Magnetic damping in binary 3-d transition metal alloys and multilayers

Dissertation

zur Erlangung des Doktorgrades
der Naturwissenschaften (Dr. rer. nat.)
der Fakultät für Physik
der Universität Regensburg

vorgelegt von

Martin Schön

aus Regensburg

März 2017

Promotionsgesuch eingereicht am: 31.01.2017 Die Arbeit wurde angeleitet von: Prof. Dr. Christian H. Back

Prüfungsausschuss: Vorsitzender: Prof. Dr. K. Rincke
1. Gutachter: Prof. Dr. C. Back
2. Gutachter: Prof. Dr. D. Weiss
weiterer Prüfer: Prof. Dr. J. Fabian

Contents

1

Introduction

Most modern computing devices are based on complementary metal oxide semiconductor (CMOS) technology. Over the last three decades an immense increase in computer processing power was achieved, which can directly be attributed to the still ongoing downscaling of the CMOS device size [1]. However, it has been predicted that this downscaling will reach its limits by the end of this decade, due to physical limitations as well as economical considerations [2]. The example of the one-electron transistor [3, 4] serves to illustrate the physical limitations of devices based on pure electronics. As the size of devices decreases (commercial release of 10 nm planned for 2017 [5]) parasitic effects, such as leakage currents and Joule heating become more prominent, increasing device power consumption exponentially [6, 7]. Based on these considerations a lower boundary on device size of approximately 5 nm is predicted [8], but whether this limit will actually be reached depends on economical and technological factors. Thus, alternatives for CMOS technology have to be found.

The field of spintronics [9–12] is by now well established and seeks to exploit both the electronic, as well as the spin degree of freedom of conduction electrons, in the search for new information storage [13], memory (RAM) [14, 15], and spin logic devices [11, 16]. Pure spin currents do not dissipate heat, which is one of their key advantages over classical electronics [17]. But even devices combining charge and spin currents benefit from a higher operation efficiency [18, 19]. In order to control the spins in a systems, the material parameters have to be well defined and tuned according to application. One critical material parameter is the damping coefficient in magnetic systems, which governs the magnetization dynamics of an excited magnetic system equilibrating towards its equilibrium state. Thus, damping affects the operational parameters of spintronics devices, such as the critical current, or switching speed for spin-transfer-torque driven magnetic switching [20,21]. Another example for the importance of the damping parameter can be found in magnonics, a sub-field of spintronics, dealing with information transport and processing utilizing magnons by studying spin wave generation, manipulation, and detection [22, 23]. Damping is a critical material parameter for magnonics applications as it is correlated to the spin wave diffusions length,

which in turn determines size and efficiency of magnonics devices [22].
The phenomenology of damping was already recognized and described in the 1930s [24, 25], however, theory has struggled to quantitatively predict the damping, even in common ferromagnetic materials [26–30]. This struggle presents a challenge for a broad range of applications in spintronics and spin-orbitronics that depend on materials and structures with well defined damping.

Of special interest are systems with ultra-low damping, as they enable many experiments that further our theoretical understanding of numerous magnetic phenomena such as damping and spin-transport [31] mediated by chirality [32] and the Rashba effect. Low damping is usually achieved in ferrimagnetic insulators such as yttrium-iron-garnet (YIG), where even for thin film damping as low as $0.9 \cdot 10^{-4}$ has been measured [33], and spin wave diffusion lengths at room temperature of tens of micrometers can be achieved [34] for a 200 nm thick YIG film. Another promising group of materials for low damping are half metallic Heusler alloys, such as $MnCo_2Ge$, Co_2FeAl or NiMnSb, for which damping constants approaching 10^{-4} have been predicted [35] and measured [36, 37].Both of those material groups require involved deposition processes like long annealing or substrate preparation and therefore immense research effort is being put into the fabrication process of those materials [38–41].

On the other hand ferromagnetic 3d transition metals Fe, Co and Ni and their alloys offer a wide range of materials properties [42] and require less involved fabrication processes. But it was believed that achieving ultra-low damping in metallic ferromagnets is limited due to the scattering of magnons by the conduction electrons. Recently, Mankovsky *et al.* [43] predicted a damping of $5 \cdot 10^{-4}$ for a $Co_{10}Fe_{90}$ alloy, which is one order of magnitude lower than the damping of metallic ferromagnets considered to possess low damping, such as the $Ni_{80}Fe_{20}$ alloy (Permalloy). This prediction motivated this work, in which the damping, as well as other magnetic properties, such as effective magnetization, and spectroscopic g-factor of Fe, Co, Ni and their binary alloys are measured via ferromagnetic resonance (FMR) and compared to theoretical predictions.
The experimentally determined damping will in most cases consist of multiple extrinsic contributions, which can be caused by a variety of mechanisms, such as eddy currents, spin pumping, inductive losses, or two magnon scattering [44–46], adding to the intrinsic damping. As the theoretical calculations of the damping do not take any of those extrinsic damping mechanisms into account, they need to be identified and quantified, in order to enable a correct comparison of experimental data to theoretical prediction. This dissertation is structured as follows.

- Chapter 1 motivates and presents the structure of this work.
- In Chapter 2 the basic properties of magnetization dynamics, the experimental method for their measurement, as well as data processing are covered.
- Chapter 3 introduces relevant damping mechanisms occurring in 3d ferromagnets. First several models for intrinsic damping processes and first principles calculations based on these models are discussed and compared to each other. Then, the extrinsic damping mechanisms radiative damping, eddy current damping, and spin pumping are elaborated on. For the radiative damping an analytic model based on FMR measurements of perpendicular standing spin waves in $Ni_{80}Fe_{20}$ is proposed.
- The experimental determination of material properties of CoNi, NiFe and CoFe alloys is described in Chapter 4. After a discussion of the sample fabrication and sample characterization via X-ray defraction, the measured magnetic properties are examined in two separate sections. Sec. 4.3 examines the magnetostatic properties of the alloys, where measurements of the alloy saturation magnetization, effective magnetization, perpendicular magnetic anisotropy, the spectroscopic g-factor and the calculated orbital magnetization are presented. The dynamic magnetic properties, inhomogeneous linewidth broadening, damping and spin pumping into adjacent normal metal layers are covered in Sec. 4.4. The focus of this section lies in the determination of all relevant extrinsic contributions to the measured damping and the calculation of the intrinsic damping, which is compared to theoretical first principle calculations.
- In Chapter 5 the intrinsic damping of the $Co_{25}Fe_{75}$ system is discussed and compared to density of states calculations.
- In Chapter 6 new sample and measurement geometries are introduced to directly measure the intrinsic damping of the $Co_{25}Fe_{75}$ alloy. Sample deposition by molecular-beam-epitaxy allows the characterization of both single crystalline and poly-crystalline $Co_{25}Fe_{75}$.
- Another method to tune damping, by varying the repetition rate of Ni-Fe double layers in a multilayer stack of fixed total thickness is demonstrated in Chapter 7.
- Finally, the experimental findings are summarized in Chapter 8.

2

Magnetization dynamics

The dynamics of magnetic relaxation processes in ferromagnets are phenomenologically well described in the Landau-Lifshitz-Gilbert equation (LLG) [24, 25]

$$\partial_t \boldsymbol{m} = -\gamma\mu_0 \boldsymbol{m} \times \boldsymbol{H}_{\text{eff}} + \frac{\alpha}{M_\text{s}} \left(\boldsymbol{m} \times \partial_t \boldsymbol{m}\right) \tag{2.1}$$

The first term describes the precession of the magnetization $\boldsymbol{m}$ around the equilibrium position, which is given by the direction of the effective magnetic field $\boldsymbol{H}_{\text{eff}}$. M_s is the saturation magnetization and $|\boldsymbol{m}| = M_\text{s}$. The second term describes the damping of this precession, i.e. a relaxation towards the equilibrium position. The damping of the precessional motion is quantified by the dimensionless Gilbert damping parameter α. γ and μ_0 are the gyromagnetic ratio and the vacuum permeability, respectively. A representation of the precession of the magnetization described by the LLG is shown in the lower panel of Fig. 2.1.

2.1 Ferromagnetic resonance

A well established experimental method to probe magnetization dynamics is ferromagnetic resonance (FMR) [47–49]. Simplified speaking, in a FMR experiment the magnetic moments of a sample, placed in a static external magnetic field are resonantly excited and driven into a collective precessional motion by an applied microwave magnetic field. The resonance condition of the magnetic system depends on the strength of the external magnetic field and the microwave frequency. Thus, by measuring the microwave absorption by the sample for different frequencies, the resonance condition can be found, giving insight into material parameters of the sample.
The resonance condition is met for a distinct pair of external field strength and microwave frequency, therefore there are two options to measure FMR: either by sweeping the external field for a fixed microwave frequency, or by sweeping the

frequency for a fixed external field, which are called field-swept or frequency-swept measurements, respectively. However, the transmission through any microwave circuit can be frequency dependent. Therefore, in order to avoid 'non-magnetic' background signals, the measurements in this work were strictly performed field-swept, and the description of FMR measurements in this chapter will be restricted to this method.
The measurement geometry is sketched in Fig. 2.1, with the external magnetic field H_0 either applied in the sample plane, along the $\boldsymbol{y}$ direction, or out of the sample plane, in $\boldsymbol{z}$ direction. These configurations are called in-plane (IP) and out-of-plane(OOP) geometry, respectively. The excitation microwave field h_x is applied in the sample plane, by means of a co-planar waveguide (CPW). For optimal excitation of magnetization precession, H_0 and h_x are perpendicular, i.e. h_x is applied along the $\boldsymbol{x}$ direction.
The transmission of single frequency microwaves is then determined for different values of the external field and the transmitted microwave power is measured, which is proportional to the microwave susceptibility χ of the sample [50], as elaborated on in a later chapter, compare Eqs. (3.26)-(3.30). At distinct values of field and frequency the susceptibility exhibits maxima, i.e. the resonance condition of the magnetic system is met and collective precession of the magnetic moments in the sample is induced.
The resonance conditions for the OOP and IP geometry are different, because χ is a tensor. Thus for OOP and IP configurations the χ_{zz} and χ_{yx} components of the susceptibility tensor are measured respectively. Both susceptibility components exhibit Lorenzian line shape [51]. Fitting and material parameter extraction will be discussed at the end of this chapter.

2.1.1 Out-of-plane geometry

The OOP component of the microwave susceptibility can be written as [52]

$$\chi_{zz} = \frac{M_\mathrm{s}\left(H_0 - M_\mathrm{eff}\right)}{\left(H_0 - M_\mathrm{eff}\right)^2 - H_\mathrm{eff}^2 - i\Delta H\left(H_0 - M_\mathrm{eff}\right)}, \tag{2.2}$$

where $H_\mathrm{eff} = 2\pi f/\gamma\mu_0$. $M_\mathrm{eff} = M_\mathrm{s} - H_k$ is the effective magnetization and H_k is the effective perpendicular magnetic anisotropy field. ΔH is the full-width-half-maximum of the susceptibility. The resonance condition is easily calculated by finding a H_0 maximizing χ_{zz}, thus finding a value for H_0 that gives a zero denominator. For small linewidths compared to M_s the OOP resonance condition can therefore be written as

$$H_\mathrm{res} = -M_\mathrm{eff} + H_\mathrm{eff} = -M_\mathrm{eff} + \frac{h}{g\mu_\mathrm{B}\mu_0} f, \tag{2.3}$$

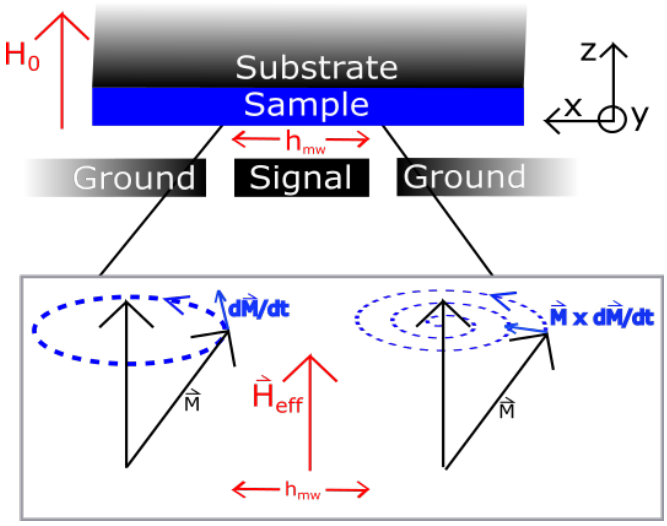

Figure 2.1: Schematic of the FMR measurement geometry. The sample is placed on the signal line of the CPW through which a current with microwave frequency is driven, inducing the microwave excitation field $h^x(I; x, z)$. The lower panel shows a sketch of the precession of the magnetization described by the LLG, Eq. (2.1), without the damping term (LHS) and with the damping term (RHS).

where h is the Planck constant, μ_B the Bohr magneton, g the spectroscopic g-factor and f the microwave frequency. The resonance field for different microwave frequencies is determined from susceptibility fits to the FMR spectra and via linear fitting of Eq. (2.3) to the resonance field data M_{eff} and g are obtained. The linewidth ΔH also displays a linear frequency dependence, given by [53]

$$\Delta H = \Delta H_0 + \alpha_{\text{tot}} \frac{4\pi f}{\gamma \mu_0}. \tag{2.4}$$

ΔH_0 is the inhomogeneous linewidth broadening, caused by magnetic inhomogeneities. In thin films it has been shown that surface or interface roughness have a strong influence on ΔH_0 [54, 55]. α_{tot} is the total measured Gilbert damping parameter, consisting of several sample and geometry dependent contributions, which will be elaborated on in a later chapter.

2.1.2 In-plane geometry

For the discussion of the IP configuration a material system with cubic crystal structure exhibiting an uniaxial and a four-fold magnetic anisotropy [51, 56] is assumed. Uniaxial anisotropy and four-fold anisotropy are aligned and the hard axis is along $\phi_m = 0$, where ϕ_m is the IP angle of the magnetization. The

other angle necessary to write down the susceptibility is ϕ_H, the IP angle of the applied external magnetic field. Then the IP susceptibility $\chi_{xy}(H_0)$ can be written as [57]

$$\chi_{xy} = \frac{M_\mathrm{s}\left(b_\mathrm{eff} - i\alpha\omega/\gamma\right)}{\left(b_\mathrm{eff} - i\alpha\omega/\gamma\right)\left(h_\mathrm{eff} - i\alpha\omega/\gamma\right) - \left(\omega/\gamma\right)^2}, \tag{2.5}$$

where

$$b_\mathrm{eff} = H_0\cos(\phi_m - \phi_H) + M_\mathrm{eff} + \frac{K_1^\parallel}{2M_\mathrm{s}}\left[3 + \cos(4\phi_m)\right] + \frac{K_\mathrm{u}^\parallel}{M_\mathrm{s}}\left[1 + \cos(2\phi_m)\right] \tag{2.6}$$

$$h_\mathrm{eff} = \cos(\phi_m - \phi_H) + \frac{2K_1^\parallel}{M_\mathrm{s}}\cos(4\phi_m) + \frac{K_\mathrm{u}^\parallel}{M_\mathrm{s}}\cos(2\phi_m). \tag{2.7}$$

$K_\mathrm{u}^\parallel$ and $K_1^\parallel$ are the uniaxial and four-fold anisotropy energy densities, respectively. For arbitrary angles ϕ_H, ϕ_m needs to be determined by minimizing the free energy of the magnetic system [56]. However, for the external field along hard and easy axis of the system $\phi_H = \phi_m$, and the resonance conditions are respectively

$$H_\mathrm{res}^\mathrm{HA} = -\left(2\frac{K_1^\parallel}{M_\mathrm{s}} + 2\frac{K_\mathrm{u}^\parallel}{M_\mathrm{s}} + M_\mathrm{eff}/2\right) + \tag{2.8}$$

$$\sqrt{\left(4\tfrac{K_1^\parallel}{M_\mathrm{s}} + 4\tfrac{K_\mathrm{u}^\parallel}{M_\mathrm{s}} + M_\mathrm{eff}\right)^2 - 4\left[2M_\mathrm{eff}\left(\tfrac{K_1^\parallel}{M_\mathrm{s}} + \tfrac{K_\mathrm{u}^\parallel}{M_\mathrm{s}}\right) + 8\tfrac{K_1^\parallel}{M_\mathrm{s}}\tfrac{K_\mathrm{u}^\parallel}{M_\mathrm{s}} + 4(\tfrac{K_1^\parallel}{M_\mathrm{s}})^2 + 4(\tfrac{K_\mathrm{u}^\parallel}{M_\mathrm{s}})^2 - (\omega/\gamma)^2\right]}$$

and

$$H_\mathrm{res}^\mathrm{EA} = -1/2\left(\frac{K_\mathrm{u}^\parallel}{M_\mathrm{s}} + M_\mathrm{eff} - \frac{K_1^\parallel}{M_\mathrm{s}}\right) + \tag{2.9}$$

$$\sqrt{\left(\tfrac{K_\mathrm{u}^\parallel}{M_\mathrm{s}} + M_\mathrm{eff} - \tfrac{K_1^\parallel}{M_\mathrm{s}}\right)^2 - 4\left[2M_\mathrm{eff}\tfrac{K_1^\parallel}{M_\mathrm{s}} + 2(\tfrac{K_1^\parallel}{M_\mathrm{s}})^2 - (\omega/\gamma)^2\right]}.$$

The linewidth dependence on frequency is the same as for the OOP configuration and is described in Eq. (2.4).

2.2 Measurement setups, fitting functions and error calculation

Two different FMR measurement setups were utilized for the experiments in this thesis, as illustrated in Fig. 2.2. Panel (a) sketches a Vector-Network-Analyzer (VNA) FMR setup. The VNA is connected to both ends of the CPW and acts as both the microwave source and detector, thus measuring all the scattering parameters S_{ab} $(a, b = 1, 2)$ of the microwave circuit. As shown by Ding *et al.* [58] the measured S_{21} transmission parameter, measured from channel 1 to channel 2 of the VNA, carries both information about the magnetic and the non-magnetic characteristics of the microwave circuit, but in a constant-frequency-field-swept measurement the non-magnetic contribution to S_{21} can be assumed to be a complex offset. Furthermore, thermal drifts or similar effects are accounted for by subtracting a complex linear background. Therefore, this discussion is limited to the 'magnetic' ΔS_{21} transmission parameter $\Delta S_{21} = S_{21}$ - offset - linear background.

The VNA measures the ΔS_{21} parameter phase sensitive, in other words both the in phase components and the out-of-phase components of the signal, which for the magnetic signal correspond to the real and imaginary part of the complex susceptibility [52]. The VNA-FMR spectrum in the OOP geometry is therefore fitted with the following function:

$$\Delta S_{21}(H_0) = A\chi_{zz}(H_0)e^{i\phi}, \tag{2.10}$$

where A is a dimensionless amplitude and ϕ is the phase. Splitting up the fitting function into real and imaginary parts enables simultaneous fitting of both in-phase and out-of-phase components of ΔS_{21}.

$$\Delta S_{21}(H_0) = \mathrm{Re}\left(\Delta S_{21}\right) + i\mathrm{Im}\left(\Delta S_{21}\right) \tag{2.11}$$

$$\mathrm{Re}\left(\Delta S_{21}\right) =$$

$$AM_\mathrm{s}\left(H_0 - M_\mathrm{eff}\right)\left[\frac{\left(\left(H_0 - M_\mathrm{eff}\right)^2 - H_\mathrm{eff}^2\right)\cos\left(\phi\right) - \left(2\alpha H_\mathrm{eff}\left(H_0 - M_\mathrm{eff}\right)\right)\sin\left(\phi\right)}{\left(\left(H_0 - M_\mathrm{eff}\right)^2 - H_\mathrm{eff}^2\right) + \left(2\alpha H_\mathrm{eff}\left(H_0 - M_\mathrm{eff}\right)\right)^2}\right] \tag{2.12}$$

$$\mathrm{Im}\left(\Delta S_{21}\right) =$$

$$AM_\mathrm{s}\left(H_0 - M_\mathrm{eff}\right)\left[\frac{\left(\left(H_0 - M_\mathrm{eff}\right)^2 - H_\mathrm{eff}^2\right)\sin\left(\phi\right) + \left(2\alpha H_\mathrm{eff}\left(H_0 - M_\mathrm{eff}\right)\right)\cos\left(\phi\right)}{\left(\left(H_0 - M_\mathrm{eff}\right)^2 - H_\mathrm{eff}^2\right) + \left(2\alpha H_\mathrm{eff}\left(H_0 - M_\mathrm{eff}\right)\right)^2}\right] \tag{2.13}$$

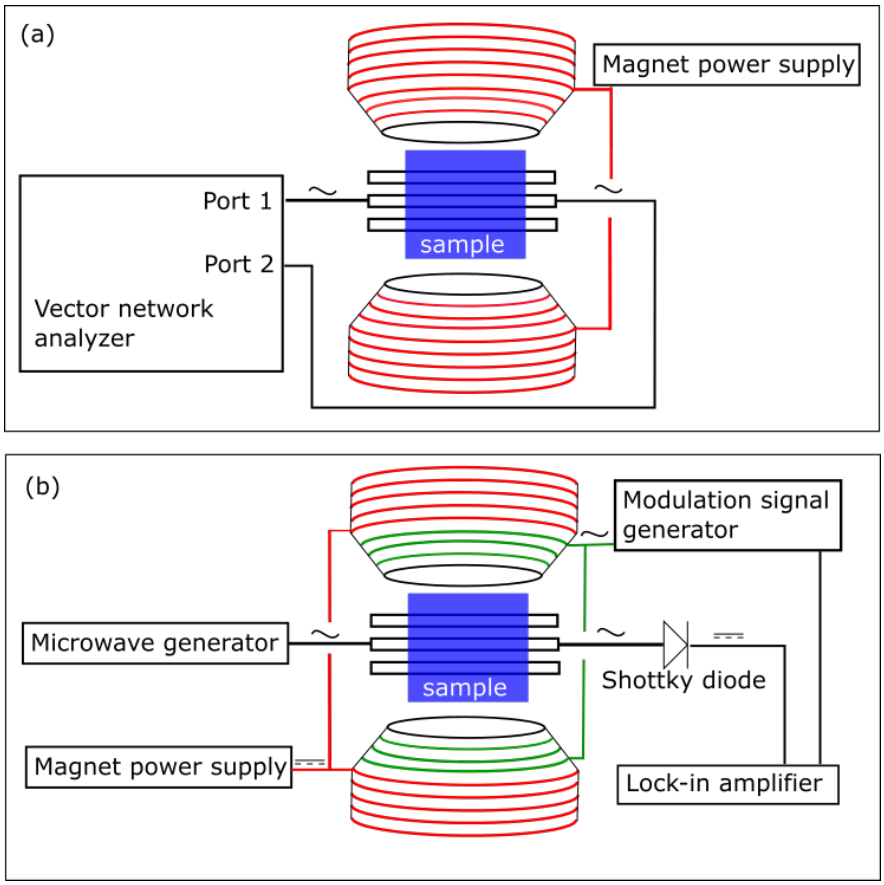

Figure 2.2: Schematic of the FMR measurement setup. (a) depicts the VNA-FMR setup, where the sample and waveguide are placed in an external magnetic field and both ends of the waveguide are connected to the VNA. Then the ΔS_{21} transmission parameter between port 1 and 2 of the VNA is measured. The second measurement setup utilized in this thesis is schematically shown in (b). The microwave signal is generated by a microwave signal generator, transmitted through the waveguide and then converted into a DC signal via a Schottky diode, which is then detected by a lock-in amplifier. Modulation of the FMR signal is achieved by modulation of the external magnetic field via a set of modulation coils.

The second measurement setup, illustrated in Fig. 2.2 (b), utilizes a microwave generator connected to the waveguide as a microwave source. The other end of the waveguide is connected to a Schottky diode, which rectifies the microwave current. The diode signal is then measured via a lock-in amplifier for better signal to noise ratio. Low frequency modulation (≈86 Hz) of the signal is achieved by field modulation. Smaller modulation coils are attached to the pole shoes of the DC field magnet and a low frequency ac current is applied inducing a modulation field on the order of 100 Oe in direction of the field H_0. The measured microwave signal is then proportional to derivative of the imaginary part of the microwave susceptibility [56] with respect to the external field. In an arbitrary measurement geometry the full microwave susceptibility can be rather complicated, but always exhibits Lorentzian lineshape [51, 59]. Therefore, the FMR spectra measured by lock-in technique are simply fitted by a combination of symmetric and anti-symmetric Lorentzians differentiated with respect to the external magnetic field [57, 59], taking the form,

$$S\frac{2\left(H_0-H_{\mathrm{res}}\right)\Delta H^2}{\left(\Delta H^2+\left(H_0-H_{\mathrm{res}}\right)^2\right)^2}+I\frac{8\Delta H\left(H_0-H_{\mathrm{res}}\right)^2-4\Delta H^3}{\left(\Delta H^2+\left(H_0-H_{\mathrm{res}}\right)^2\right)^2}. \tag{2.14}$$

S and I are the amplitudes of symmetric and antisymmetric Lorentzian respectively. H_{res} here carries all information on the magnetic anisotropy, as anisotropy is not explicitly included in the fitting function. All anisotropies then can be determined by measuring H_{res} angle dependent [56].
Errors for all fitting parameters are determined by 1σ (95 %) confidence intervals of the fits. These errors are then used as weights for fitting Eqs. (2.3) and (2.4) to the resonance field and linewidth data. The spectroscopic g-factor g and the effective magnetization M_{eff} are the fitting parameters in Eq. (2.3), and the inhomogeneous linewidth broadening ΔH_0 and the damping α are fitting parameters in Eq. (2.4). The fitting errors to these parameters are again determined by 95 % confidence intervals of the fits, thus assigning reasonable errors to the extracted determined material parameters.

3

Gilbert-like Damping

The focus of this thesis lies on the measurement of Gilbert-like damping mechanisms, i.e. damping mechanisms leading to a linear dependence of linewidth on frequency. In the previous chapter damping was only introduced as a phenomenological parameter to describe the relaxation of an excited magnetization vector towards the equilibrium position and to quantify the linewidth of FMR spectra. In this chapter the physical origins of multiple damping mechanisms will be discussed. The contributions to the experimentally determined damping are commonly divided into two categories: intrinsic damping and extrinsic contributions to the damping [50]. As this distinction is often misleading, only the damping directly correlated to intrinsic material properties, will be called intrinsic damping. In other words, only the damping that cannot be influenced or determined by sample or measurement geometry will be called intrinsic damping. Damping mechanisms that can be influenced by sample or measurement geometry will be called extrinsic damping.

3.1 Intrinsic damping

Even in a perfectly crystalline ferromagnet the magnetic precession will not be free of damping. Many theoretical approaches state that this is due to spin-orbit-coupling (SOC), a purely quantum mechanical effect that couples spin and orbital moments [51]. The SOC enables transfer of energy from the spin system to the electronic system, thus opening a channel for energy dissipation from the spin precession. In combination with other equilibration processes of the electronic system, this leads to a damping of the precession.

One of the goals of the theoretical description of the damping is to correctly model the experimentally found temperature dependence of the damping in metallic ferromagnets [60, 62]. An example of this behavior is shown in Fig. 3.1, depicting both an increase of the damping towards low and towards high temperatures. This behavior closely correlates to the behavior of the conductivity at low temperatures and the behavior of the resistivity at high temperatures and is therefore

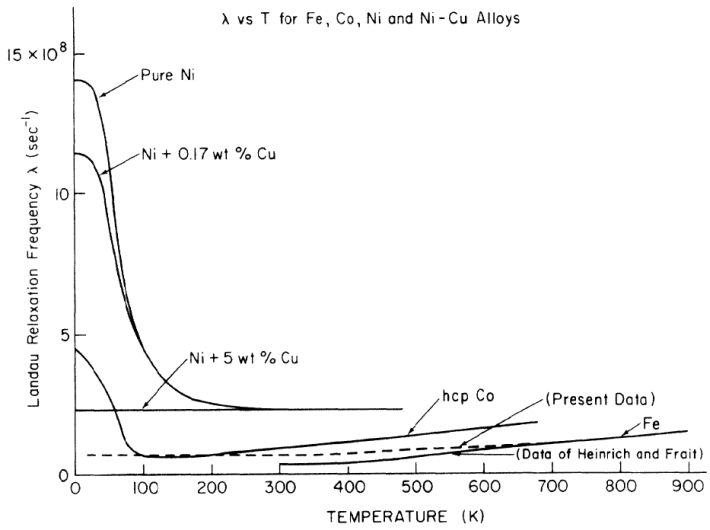

Figure 3.1: From Ref. [60] and references therein. Collected data for the temperature variation of the Landau relaxation frequency λ ($\lambda \propto \alpha$, compare Ref. [61]) for Fe, Co, Ni, and NiCu alloys.

also called conductivity-like and resistivity-like, respectively.
More recently numerical calculations of values for the damping and both temperature dependence and alloy composition dependence have been published [43, 63, 64]. In the following sections a short overview of the most prominent approaches and their numerical results will be given.

3.1.1 Breathing and bubbling Fermi surface models

One of the early successful theories describing the conductivity-like low temperature behavior of the damping was that of Kamberský, who introduced the so-called breathing Fermi surface model (BFS) [65, 66]. In the BFS model the damping term (in Landau-Lifshitz notation λ, compare Ref. [61]) is written as

$$\lambda = \frac{g^2 \mu_B^2}{\hbar} \sum_n \int \frac{dk^3}{(2\pi)^3} \eta\left(\epsilon_{n,k}\right) \left(\frac{\partial \epsilon_{n,k}}{\partial \theta}\right)^2 \frac{\tau_1}{\hbar}. \tag{3.1}$$

The name breathing Fermi surface stems from the picture that the precessing magnetization, due to spin-orbit coupling, distorts the Fermi surface, as modeled in Eq. (3.1) by variations of the single particle states $\partial \epsilon_{n,k}$ with the spin direction θ. n and k are labeling band index and wave vector, respectively. $\eta\left(\epsilon_{n,k}\right)$ is the negative derivative of the Fermi function only allowing states near the Fermi energy to contribute to the damping. The distortion of the Fermi surface

causes some populated states to rise above the Fermi energy and pushes some unpopulated states below, creating electron-hole pairs near the Fermi surface. Recombination of the electron-hole pairs is delayed by the lifetime τ, which in this way governs the equilibration of the system. A short scattering time (high temperature) will cause a quick equilibration of the distorted Fermi surface and therefore lower damping. However, for long life times a stronger distortion of the Fermi surface is induced and a stronger damping is expected. Therefore, the damping scales with τ_l.
When comparing the predictions of the BFS model to experimental findings, good qualitative agreement for the low temperature (large τ_l) behavior of the damping is found, compare Fig. 3.1. However, the BFS fails in describing the resistivity-like increase of the damping at higher temperatures.

Therefore a different mechanism has to be responsible for this behavior. Heinrich, *et al.* [67] described this mechanism in the so called bubbling Fermi surface model or s-d exchange model. This model is based on the interaction of localized d-states with itinerant s-p states. Strictly speaking, there is no clear distinction between s-p and d states in 3d transition metals, due to s-p hybridization and d-band delocalization [68,69] of differing degrees, but the distinction here serves to describe electrons of localized and itinerant character. The interaction between s and d electrons enables a scattering between magnons and itinerant electrons, resulting in the creation and annihilation of electron-hole pairs. The magnon gets annihilated in the scattering process, which therefore entails a spin-flip, due to angular momentum conservation. s-d scattering alone does not dissipate angular momentum from the magnetic system, as it only changes the occupation of the bands. Only in combination with additional scattering processes, which recombine the electron-hole pairs, angular moment dissipation in the magnetic system can occur. The damping in the s-d model can be written as [50, 57]

$$\alpha = \frac{\mu_\mathrm{B}^2 N(E_\mathrm{F})}{M_\mathrm{s}\gamma}\frac{1}{\tau_\mathrm{l}}, \tag{3.2}$$

where $N(E_\mathrm{F})$ is the density of states at the Fermi energy and τ_l is the interband electron-hole lifetime time. From this equation it is obvious that the damping caused by s-d interaction increases with increasing temperature (small τ_l), thus describing the high temperature behavior of the damping.
A note of caution is necessary at the end of this section, since the lifetimes τ_l for the BFS and the s-d models are not automatically the same. The strength of different scattering mechanisms, such as electron-electron or electron-phonon scattering, limiting the lifetimes of electron-hole pairs, depend on the exact band structure and can therefore differ for the electron-hole pairs produced in the two different scattering processes. Nevertheless, the lifetimes always are proportional to the momentum scattering time τ, and can be approximated by it.

3.1.2 Torque correlation model

In order to describe the damping over the whole temperature range Kamberský [29] introduces his so-called torque-correlation model. In the torque correlation model the damping can be written as [27]

$$\lambda = \frac{g^2 \mu_B^2}{\hbar} \sum_{n,m} \int \frac{dk^3}{(2\pi)^3} \left| \Gamma_{n,m}^- \right|^2 W_{nm}(k), \tag{3.3}$$

where $\Gamma_{n,m}^- = \langle n, k \,|[\sigma^-, H_{SO}]|\, m, k \rangle$ are the matrix elements for the SOC mediated transition between state m and n and $W_{nm}(k) = (1/\tau) \int d\omega \eta(\omega) A_{n,k}(\omega) A_{m,k}(\omega)$ describes the spectral overlap of the electron spectral functions $A_{m/n,k}$ at the Fermi Energy. $A_{m/n,k}$ are modeled as Lorenzian functions with width $\propto \hbar/\tau$ around the center of the band.
Qualitatively Eq. (3.3) describes the decay of magnons into electron-hole pairs, mediated by SOC. The electron-hole pairs can either occupy the same band or two different spin split bands, i.e the spin-flip scattering can occur intra- or inter-band. The intra-band spin flip scattering only is non-zero due to a mixing of both spin states in one band, caused by the SOC.

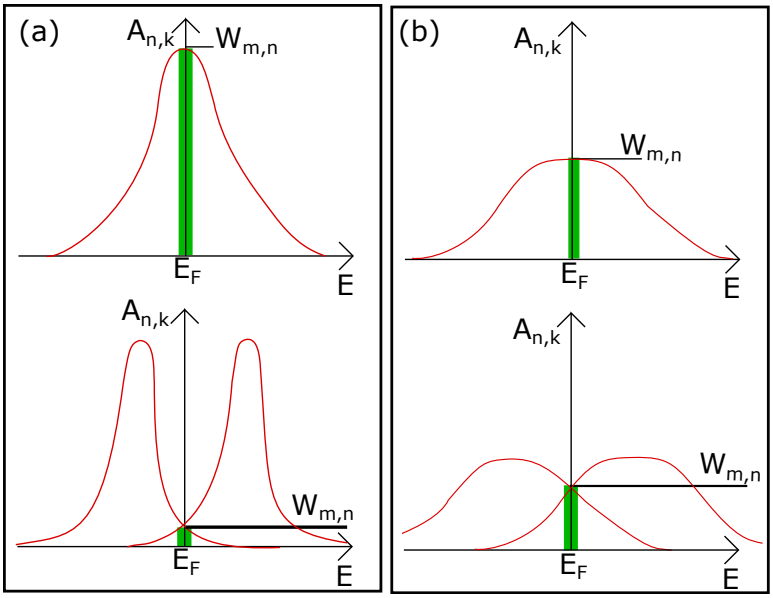

Figure 3.2: Illustration of the spectral overlap function W_{nm}. (a) and (b) show spectral functions $A_{m/n,k}$ for intra and inter band scattering with small (large τ) and large (small τ) width, respectively. The width of the spectral functions is shown by the blue lines and W_{nm} is signified by the green areas. Adapted from Ref. [61].

The spectral overlap function at the Fermi energy W_{nm} exhibits different behavior for intra- and inter-band transitions. In the case of intra-band transitions, W_{nm}

is approximately the amplitude of the Lorenzian spectral function at the Fermi energy. Thus, W_{nm} scales inversely with the width of the spectral function and therefore scales directly with the scattering time τ. For an inter-band scattering event W_{nm} describes the overlap between two energetically shifted electron spectral functions at the Fermi energy. W_{nm} now scales with the width of the spectral functions ($\propto 1/\tau$). An illustration of W_{nm} for the two different cases is shown in Fig. 3.2. Thus, it can be concluded that Eq. (3.3) qualitatively describes both resistivity and conductivity like behavior of the damping. As shown in Ref. [27] the intra-band terms of Eq. (3.3) describe the same physics as the BFS model in the long scattering time limit.

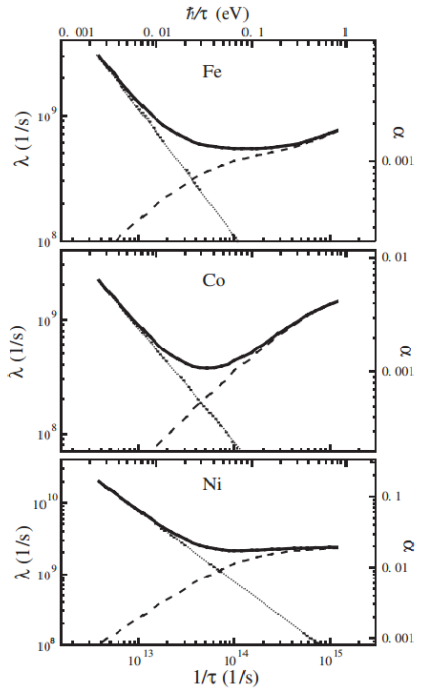

Figure 3.3: From Ref. [27]. The dependence of the damping parameter on the inverse scattering time $1/\tau$ is shown for Ni, Fe and Co (solid lines). The dotted lines represent the inter-band contributions and the dashed lines the intra-band contributions. For all elements the damping displays a distinct minimum for different scattering times.

Due to the taxing computational requirements for quantitative predictions by this model only limited quantitative analysis was published [65] until more recently Gilmore, *et al.* [27], as well as Thonig, *et al.* [70] computed values of the damping based on the torque-correlation model for the 3d transition metals Ni, Co and Fe, as shown in Fig. 3.3.

The calculated damping depends on the momentum scattering time τ. For longer τ the damping increases, because the intra-band scattering contribution to the damping dominates, causing a damping enhancement. Similarly, for shorter τ the inter-band contribution dominates, enhancing the damping. Therefore the damping exhibits a minimum in 3d transition metals at a element specific τ, when both intra- and inter-band contributions are of roughly similar magnitude. These calculations model the temperature dependence of the damping reasonably well, but quantitative comparison to measurements is complicated due to difficulties in the exact determination of the momentum scattering time. This reliance on τ is a large obstacle for a quantitative analysis. Nevertheless, the torque correlation model delivers a good qualitative description of the temperature dependent behavior of the damping and can be a rather intuitive tool for materials engineering of the damping.

3.1.3 Scattering matrix approach

Another approach for the calculation of α_{int} via scattering theory was successfully implemented by Brataas, *et al.* [30], which is a generalization on non-local interfacial damping enhancement, i.e. spin pumping (discussed in Sec. 3.2.3). However, intrinsic spin relaxation can also be included in the scattering matrix formalism. The calculations are based on the model of a ferromagnet in contact to a thermal bath via normal metal leads. The precession of the magnetization heats up the ferromagnetic system and this excess heat leaks via the normal metal contacts, thus dissipating energy from the magnetic system. The energy pumping into the normal metal leads can be described in a scattering matrix (S_{ij}) formalism, accounting for reflexion and transmission at the interfaces. Comparison of this energy flux to the energy dissipation term in the LLG results in an expression for the damping tensor $\tilde{G}_{ij}$, which depends on the scattering matrix:

$$\tilde{G}_{ij} = \frac{\gamma^2 \hbar}{4\pi} \mathrm{Re}\left(\mathrm{Tr}\left[\frac{\partial S}{\partial \tilde{m}_i} \frac{\partial S^\dagger}{\partial \tilde{m}_j} \right] \right), \tag{3.4}$$

where $\tilde{m}_i$ and $\tilde{m}_j$ are the components of the normalized magnetization vector $\tilde{\boldsymbol{m}} = \boldsymbol{m}/M_{\mathrm{s}}$. The expression for the intrinsic damping in the scattering matrix approach is qualitatively similar to the one derived in the torque-correlation model [30]. But the scattering matrix approach allows simultaneous and separable determination of bulk-damping and spin pumping contribution, by including spin-flip scattering in the scattering matrix. Assuming isotropic damping $\tilde{G}_{ij}) = \tilde{G}$), and the total damping for a sample with thickness t can be written as $\tilde{G}(L) = \tilde{G}_{\mathrm{interface}} + \tilde{G}_{\mathrm{bulk}}(t)$, where $\tilde{G}_{\mathrm{interface}}$ is the interfacial damping term, which is constant in this approach and $\tilde{G}_{\mathrm{bulk}}(t)$ is the thickness dependent bulk damping,which can be expressed as $\tilde{G}_{\mathrm{bulk}}(t) = \alpha\gamma M_{\mathrm{s}}(t)$. The Gilbert damping parameter is then extracted from the slope of $\tilde{G}_{\mathrm{bulk}}(t)$ vs. t, as demonstrated in Ref. [63].

3.1.4 Numerical calculations of the damping

Over the last two decades the development of powerful computational and theoretical methods (density functional theory, DFT) allowed detailed calculations of the electronic band structure. Based on these band structure calculations various approaches to quantitatively model the damping in 3d transition metals and their alloys have been published. The following paragraph is intended as an overview

of the calculations that experimental results are compared to in this thesis, with no claim for completeness.
A numerical estimate of the damping of Fe and Ni in the linear response model was performed by Kamberský himself [71]. Similarly Gilmore, *et al.* [27], as well as Thonig, *et al.* [70] calculated the damping for Ni, Fe and Co in a torque correlation model. Both of these approaches specify the SOC as the main mechanism for the damping, but do not describe mechanisms for the spin flip scattering, necessary to dissipate angular momentum from the system. Both models rely on artificially introduced parameters to model the electron life time. Therefore, these calculations yield the damping only as a function of the momentum scattering time. This problem was first addressed by Brataas, *et al.* [30], who described the damping via scattering theory, allowing Starikov, *et al.* [63] a first principles calculation of the damping of NiFe alloys, which was expanded by Liu, *et al.* [72] to include the influence of electron-phonon interaction on the damping. Furthermore, this formalism was applied for the calculation of the damping in non-collinear ferromagnetic systems, i.e. domain walls [73]. Another first principles approach was achieved by a numerical realization of Kamberský's linear response model [65] performed by Ebert, *et al.* [26] for NiFe. Later Mankovsky, *et al.* [43] expanded the calculations for NiCo, NiFe, FeV and CoFe alloys. The latter work includes calculations of the dependence of the damping on temperature for Ni, Fe, and Co, making it a comprehensive theoretical study of binary alloy properties and will be the main study to compare experimental values to in this thesis. More recently Turek, *et al.* [64] calculated the damping for NiFe and CoFe alloys in the torque-correlation model, utilizing non-local torque correlators, thus archiving an *ab initio* description of the damping in those systems.

3.2 Extrinsic Contributions to the total measured damping

The methods for the calculation of the damping described in the previous sections only account for the intrinsic damping of the ferromagnet. Experimentally determined damping will often consist of multiple extrinsic contributions additional to the intrinsic damping [74]. Hence, the extrinsic contributions to the damping need to be identified and quantified in any experiment in order to facilitate a comparison of experimentally determined damping to calculated values. This chapter introduces several mechanisms for extrinsic contributions to the damping and how to experimentally determine them.

3.2.1 Radiative damping

The model and experimental results presented in this section have been published in Ref. [46].
According to Faraday's Law, the time-varying flux of a precessing magnetic moment generates an ac voltage in any conducting material that passes through the flux. As shown in Fig. 3.4, spin wave precession in a conducting ferromagnet on top of a coplanar waveguide (CPW) induces ac currents both in the ferromagnet and the CPW. The dissipation of these eddy currents in the sample, and the flow of energy away in the CPW give rise to two contributions to magnetic damping. Historically, the damping caused by eddy currents in the ferromagnet α^{eddy} is called eddy current damping, while the damping caused by the eddy currents in the waveguide is called radiative damping α_n^{rad}. This section will describe an analytical model for radiative damping. The validity of this model is supported by damping measurements of perpendicular standing spin waves (PSSWs) in Permalloy films.

3.2.1.1 Radiative damping model

In a experimental geometry as sketched in Fig. 3.4 (a), a ferromagnetic sample with thickness δ and length l is placed on top of the center conductor of a coplanar waveguide (CPW) with width W. The sample dimension along $\boldsymbol{x}$ is much larger than W. The sample and CPW are separated by a gap of height d. An external DC magnetic field $\boldsymbol{H}_0$ is applied perpendicular to the sample plane, and the spin wave resonances (SWR) are driven by microwaves in the CPW at resonance frequency f. A fraction of the ac magnetic induction $\boldsymbol{B}$ due to the

dynamic component of the magnetization $m_n^x(H_0, I; z)$ wraps around the center conductor.

To derive a quantitative expression for α_n^{rad}, we start by calculating $h^x(I; x, z)$, the $\boldsymbol{x}$ component of the driving field $\boldsymbol{h}_{\mathrm{mw}}$ that is generated by an excitation current I in the center conductor. We assume $h^x(I; x, z)$ is uniform along $\boldsymbol{y}$, but we allow for variation along $\boldsymbol{x}$ and $\boldsymbol{z}$. To estimate $h^x(I; x, z)$ we use the Karlqvist equation [75]

$$h^x(I; x, z) = \frac{I}{2\pi W}\left[\arctan\left(\frac{x + W/2}{z}\right) - \arctan\left(\frac{x - W/2}{z}\right)\right]. \tag{3.5}$$

This microwave field can excite PSSWs in the sample. Schematic mode profiles for the fundamental mode ($n = 0$) and the first three PSSW modes are shown in Fig. 3.4(b), where arbitrarily unpinned boundary conditions at the top surface and pinned boundary conditions at the bottom surface were chosen.

The mode profiles describe a z-dependence of the dynamic magnetization components m^x and m^y. In the perpendicular geometry used here, $|m^x| = |m^y|$ everywhere, i.e. the precession is circular. In what follows, only m^x, the dynamics of which are inductively detected in the measurement, will be discussed. Furthermore, the analysis is restricted to the case of ideal perpendicular standing spin wave modes in a fully saturated film that only vary through the film thickness without any lateral variation. This eliminates the need to explicitly consider the full Polder susceptibility tensor in the calculation of the sample response to the excitation field. The sample dimensions are l along the waveguide direction, δ in thickness, but infinite in the lateral direction.
Introducing the concepts of a spin wave mode susceptibility χ_n, and the dimensionless, normalized spin wave amplitude $q_n(z)$ for the nth spin wave mode, the magnetic excitation of amplitude in x-direction $\tilde{m}_n^x(H_0, I; z)$ that results from the application of a microwave magnetic field of amplitude $h^x(I; x, z)$, driven by an ac current $I = V_{\mathrm{in}}/Z_0$ in an applied field H_0 can be written as

$$\tilde{m}_n^x(H_0, I; z) := \tilde{m}_n^x(z) = q_n(z)\,\chi_n(H_0)\,\langle q_n(z)\,h^x(I; x, z)\rangle \tag{3.6}$$

where the quantity in brackets is simply the overlap integral of the excitation field and the normalized spatial profile of the nth spin wave mode $q_n(z)$. The magnetic excitation of amplitude in y-direction $\tilde{m}_n^y(z)$ can be written in a similar way. In the trivial case of a uniform excitation field and uniform spin wave mode, we recover the usual relation between the excitation field and the magnetization dynamics via the Polder susceptibility tensor component, χ^{xx}. However, if the product of the mode profile and excitation field has odd spatial symmetry, dynamics are not excited, as we expect. The overlap integral is nothing more than

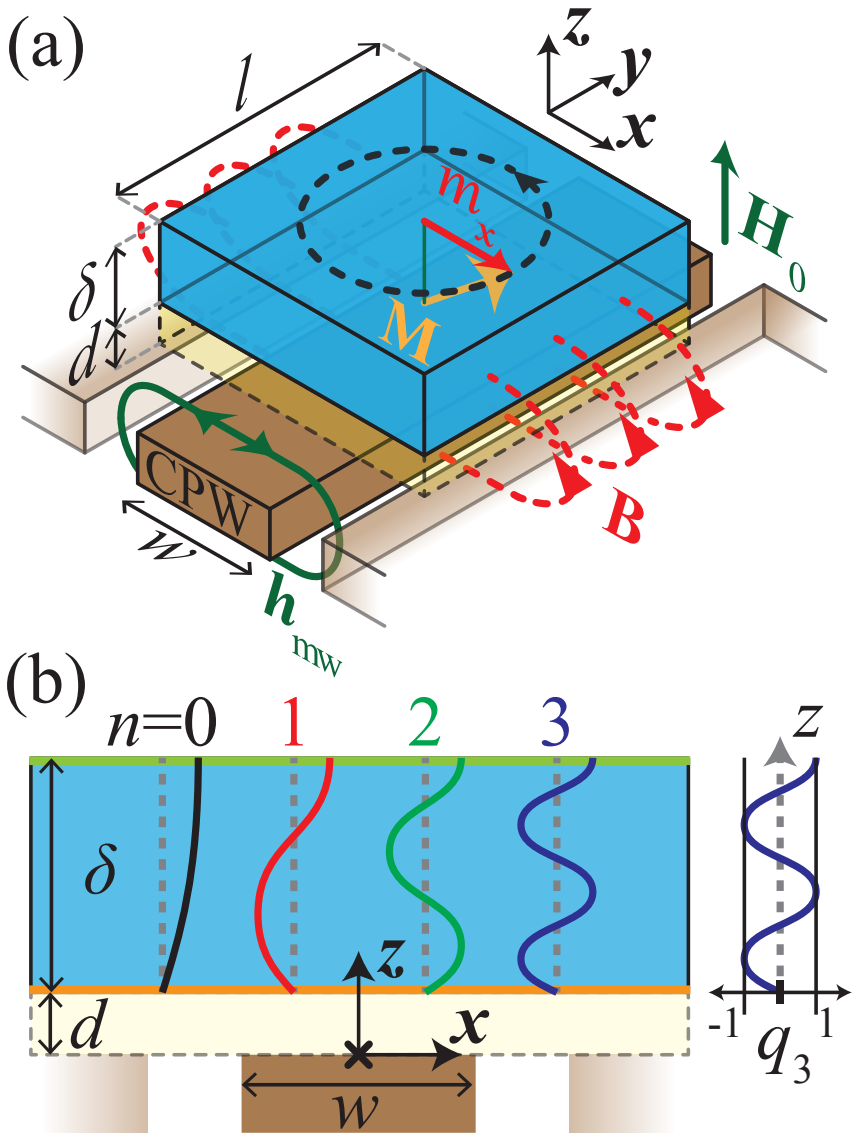

Figure 3.4: Schematic of the radiative damping process. (a) $\boldsymbol{M}$ is the dynamic magnetization, $\boldsymbol{H}_0$ the applied external field and $\boldsymbol{B}$ is the magnetic inductance due to the x-component m_x of the dynamic magnetization. W is the width of the center conductor, l the length of the sample on the waveguide, δ the thickness of the sample and d the spacing between sample and wave guide. (b) Simplified depiction of the PSSW eigenfunctions q_n for mode numbers n= 0, 1, 2, 3. We exemplary used boundary conditions that are completely pinned on one side and completely un-pinned on the other side. The origin of the coordinate system is indicated.

the spatial average of the mode/excitation product:

$$\langle q_n(z)h^x(I;x,z)\rangle = \frac{1}{W\delta}\int_{-\infty}^{\infty} dx \int_d^{\delta+d} dz q_n(z)h^x(I;x,z). \tag{3.7}$$

The power transferred to the waveguide via inductive coupling with the spin wave dynamics is given by

$$P_n = \frac{\left|\partial_t \Phi_n\left(H_0, I\right)\right|^2}{2Z_0}, \tag{3.8}$$

where

$$\partial_t \Phi_n\left(H_0, I\right) = \mu_0 \ell \int_{-\infty}^{\infty} dx \int_d^{\delta+d} dz \left(\partial_t m_n^x\left(z\right)\right) \tilde{h}^x\left(x,z\right), \tag{3.9}$$

with $\tilde{h}^x\left(x,z\right) = h^x(I;x,z)/I$.
It is important to recognize at this point that the power dissipation is not constant with time, given that P_n is proportional only to $\partial_t m_n^x$. As such, the damping associated with the re-radiation of the microwave energy back into the waveguide is best characterized with an anisotropic damping tensor, to be elaborated upon in more detail later in this section. To calculate the energy of the spin wave mode a spatially averaged spin wave excitation density [76] is defined,

$$\left\langle \mu_n^2\left(H_0, I\right)\right\rangle = \frac{\int_{-\infty}^{\infty} dx \int_d^{\delta+d} dz \left[\left(\partial_t m_n^x\left(z\right)\right)\left(m_n^y\left(z\right)\right)^* - \left(\partial_t m_n^y\left(z\right)\right)\left(m_n^x\left(z\right)\right)^*\right]}{4\omega\delta W}. \tag{3.10}$$

Then, the magnon density N_n associated with the nth spin wave excitation is

$$N_n = \frac{\left\langle \mu_n^2\left(H_0, I\right)\right\rangle}{2g\mu_B M_s} \tag{3.11}$$

And the total energy associated with the spin wave mode is given by

$$E_n = \frac{\omega\left\langle \mu_n^2\left(H_0, I\right)\right\rangle}{\gamma M_s}\delta\ell W \tag{3.12}$$

The energy dissipation rate $\left(1/T_1\right)_n$ for the nth mode is therefore

$$\left(\frac{1}{T_1}\right)_n = \frac{P_n}{E_n} = \frac{2\mu_0 \ell \omega_M}{Z_0} \frac{\left| \int_{-\infty}^{\infty} dx \int_{d}^{\delta+d} dz \left(\partial_t m_n^x(z)\right) \tilde{h}^x(x,z) \right|^2}{\int_{-\infty}^{\infty} dx \int_{d}^{\delta+d} dz \left[\left(\partial_t m_n^x(z)\right) \left(m_n^y(z)\right)^* - \left(\partial_t m_n^y(z)\right) \left(m_n^x(z)\right)^* \right]}, \tag{3.13}$$

where $\omega_M = \gamma \mu_0 M_s$. Applying the Fourier transform to move into the frequency domain, where $\partial_t m_n^x(H_0, I; z) \leftrightarrow i\omega \tilde{m}_n^x(H_0, I; z)$, such that the energy relaxation rate $(1/T_1)_n^x$ for magnetization oscillations along the x-axis is written as

$$\left(\frac{1}{T_1}\right)_n^x = \frac{\omega \mu_0 \ell \omega_M}{Z_0} K_n, \tag{3.14}$$

where

$$K_n := \frac{\left| \int_{-\infty}^{\infty} dx \int_{d}^{\delta+d} dz \left(\tilde{m}_n^x(z)\right) \tilde{h}^x(x,z) \right|^2}{\int_{-\infty}^{\infty} dx \int_{d}^{\delta+d} dz \mathrm{Im}\left[\tilde{m}_n^x(z) \left(\tilde{m}_n^x(z)\right)^*\right]} \tag{3.15}$$

is a dimensionless inductive coupling parameter. In the limiting case of the $n = 0$ (i.e., uniform) mode with a uniform excitation field due to current flowing only through the waveguide center conductor, and an infinitesimal spacing between the waveguide and the sample, we have $K_0 = \delta/4w$. Substituting Eq. (3.6) into Eq. (3.15), the general result

$$K_n = \frac{\left| \int_{-\infty}^{\infty} dx \int_{d}^{\delta+d} dz q_n(z) \tilde{h}^x(x,z) \right|^2}{\epsilon \int_{d}^{\delta+d} dz |q_n(z)|^2}, \tag{3.16}$$

is obtained, with $\epsilon = |\tilde{m}_n^z| \,/\, |\tilde{m}_n^x|$.
Since the energy dissipation rate for the case of radiative damping is anisotropic, it must be generally treated in the damping tensor formalism, where the Gilbert damping torque $\boldsymbol{T}$ is given by

$$T_k = \varepsilon_{ijk} \alpha_{ij} \hat{m}_i (\partial_t \hat{m})_j. \tag{3.17}$$

The equation of motion is given in form of a LLG

$$\partial_t \hat{m} = -\gamma\mu_0 \hat{m} \times \boldsymbol{H} + \boldsymbol{T} \tag{3.18}$$

and $\hat{m} = \boldsymbol{M}/M_s$ is the normalized magnetization. For the coordinates in Fig 3.4, the only nonzero radiative damping tensor components are α_{zx} and α_{yx}. For the perpendicular FMR geometry, the relationship between the energy relaxation rate and the Gilbert damping components is

$$\left(\frac{1}{T_1}\right)^x = \alpha_{zx}\omega_x, \tag{3.19}$$

and

$$\left(\frac{1}{T_1}\right)^y = \alpha_{zy}\omega_y, \tag{3.20}$$

where ω_x and ω_y are the respective stiffness frequencies, defined as

$$\omega_i := \frac{\gamma}{M_s}\frac{\partial^2 U_m}{\partial \hat{m}_i} \tag{3.21}$$

and U_m is the magnetic free energy function. The frequency-swept linewidth $\Delta\omega = \gamma\mu_0\Delta H$, where ΔH is the field-swept linewidth in Eq. (3.40), is given by

$$\Delta\omega = \frac{\left(\frac{1}{T_1}\right)^x + \left(\frac{1}{T_1}\right)^y}{2} \tag{3.22}$$

$$= \alpha_{zx}\omega_x + \alpha_{zy}\omega_y \tag{3.23}$$

For perpendicular FMR, $\omega_x = \omega_y = \omega$, and the specific case of anisotropic radiative damping, $\alpha_{zx} = \alpha_n^{\mathrm{rad}}$, $\alpha_{zy} = 0$,

$$\alpha_n^{\mathrm{rad}} = \frac{1}{2\omega}\left(\frac{1}{T_1}\right)_n^x = \frac{\mu_0 l \omega_M}{2Z_0} K_n \tag{3.24}$$

and $\Delta\omega_n^{\mathrm{rad}} = \alpha_n^{\mathrm{rad}}\omega$. This is in contrast to the case of isotropic damping processes, such as eddy currents and intrinsic damping, where $\Delta\omega_n^{\mathrm{iso}} = 2\alpha_n^{\mathrm{iso}}\omega$ instead. Thus, the net damping due to the sum of anisotropic radiative damping, and any other isotropic processes, is given by

$$\alpha_n = \alpha^{\mathrm{isotropic}} + \frac{\alpha_n^{\mathrm{rad}}}{2} \tag{3.25}$$

where α_n is the total measured damping parameter for the field-swept linewidth.

We use a vector network analyzer (VNA) to measure the two-port S-parameter matrix element for the nth spin wave mode, ΔS_n^{21}. The matrix element is defined as the ratio of the voltage induced in the waveguide by the nth spin wave mode $V_n(H_0)$ in an applied magnetic field H_0, and the excitation voltage V_{in},

$$\Delta S_n^{21} := \frac{V_n(H_0)}{V_{in}}. \tag{3.26}$$

If we model the reactance of the nth spin wave mode as nothing more than a purely inductive element of inductance L_n in series with an impedance matched transmission line, and if we assume the sample inductance is much smaller than the transmission line impedance, we can approximate ΔS_n^{21} as

$$\Delta S_n^{21}(H_0) \cong -\frac{i\omega L_n(H_0)}{Z_0}, \tag{3.27}$$

where $L_n(H_0) = \Phi_n\left(H_0, I\right)/I$.

We define a normalized, field-independent mode-inductance $\widetilde{L}_n$ as

$$\widetilde{L}_n := \frac{L_n(H_0)}{\chi_n(H_0)}, \tag{3.28}$$

and a dimensionless, field-independent mode-amplitude A_n,

$$A_n := \frac{i\omega\widetilde{L}_n}{Z_0}. \tag{3.29}$$

such that

$$\Delta S_n^{21}(H_0) = -A_n\chi_n(H_0). \tag{3.30}$$

Thus, A_n is the dimensionless amplitude parameter that we obtain when fitting data for $\Delta S_n^{21}(H_0)$. By use of Eqs. 3.9, 3.29, and 3.28, we can rewrite the mode-amplitude as

$$A_n := i\frac{\omega\mu_0 l}{W\delta Z_0}\left(\int_{-\infty}^{\infty} dx \int_d^{\delta+d} dz q_n(z)\tilde{h^x}(x,z)\right)^2. \tag{3.31}$$

Remembering that the normalized mode inductance has a factor identical to the numerator of Eq. (3.16), we can rewrite the radiative damping in terms of the normalized mode inductance,

$$\frac{\alpha_n^{\mathrm{rad}}}{\widetilde{L}_n} = \frac{\omega_M \eta_n}{Z_0}, \tag{3.32}$$

where

$$\eta_n := \frac{\delta}{4\int_d^{\delta+d} dz\,|q_n(z)|^2} \tag{3.33}$$

We emphasize that Eq. (3.32) is a very general result, regardless of the details of the excitation field profile. Thus, even if the field profile is highly non-uniform due to the combination of eddy current and capacitive coupling effects [77, 78], there should still be a fixed scaling between the radiative damping and the normalized inductance.
In the case of the uniform mode, $\eta = 1/4$ and Eq. (3.32) reduces to

$$\frac{\alpha_n^{\mathrm{rad}}}{\widetilde{L}_n} = \frac{\omega_M}{4Z_0}. \tag{3.34}$$

However, for a sinusoidal mode of the form

$$q_n(z) = \cos\left(\frac{(2n+1)\,\pi z}{2\delta}\right) \tag{3.35}$$

that is expected in the case of a pinned boundary condition at one interface and an open boundary condition at the other interface, as shown in Fig. 3.4 (b), we obtain $\eta = 1/2$ and

$$\frac{\alpha_n^{\mathrm{rad}}}{\widetilde{L}_n} = \frac{\omega_M}{2Z_0}, \tag{3.36}$$

For the case of the wavenumber values extracted from the data shown in Fig. 3.6 (c) for a 200 nm Py film, we can determine the value for η_n and the degree to which it can vary with mode number. We use the following form for the spin wave profile:

$$q_n(z) = \cos\left(k_n z\right) \tag{3.37}$$

consistent with our assumption, when extracting k_n from our PSSW data, that an unpinned boundary condition applies to only one of the interfaces, i.e. at $z = 0$. Using these extracted values for the wavenumber, we obtain values for η_n shown in Fig. 3.5. We see in Fig. 3.5 that the variation in η_n with varying

mode number is less than 10 %. Thus, to within first order, we can treat η_n as a constant for the purposes of fitting our data, i.e. $\eta_n \cong \eta$.

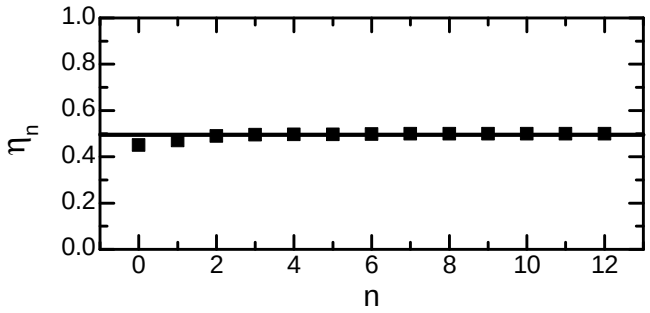

Figure 3.5: Dependence of calculated values for η_n on mode number for the case of the spectral data presented in Fig. 3.6 (c) and 3.9 (a). Wavenumbers are extracted from those data via the procedure outlined in the main text of the paper, based upon a model with a single surface with interfacial anisotropy, and an unpinned boundary condition at the other interface. Within the context of that particular model, and the expected quadratic dependence of spin wave resonance frequency with wavenumber that it produces, we see that η_n has a weak dependence on mode number, justifying our presumption that η_n can be treated as a constant for the purposes of fitting the damping data.

3.2.1.2 Sample fabrication

We deposited Ta(3)/Py(δ)/Si3N4(3), Ta(3)/Py(δ)/Ta(5), Ta(3)/Py(δ), and Py(δ) layers on 100 μm thick glass substrates by DC magnetron sputtering at a Ar pressure of 0.7 Pa ($\approx 5 \times 10^{-3}$ Torr) in a chamber with a base pressure of less than 5×10^{-6} Pa ($\approx 4\times10^{-8}$ Torr); where $\delta = 75$ nm, 120 nm and, 200 nm is the permalloy thickness. The Py thickness was calibrated by x-ray reflectivity. We estimate that the damping enhancement due to spin pumping (compare Sec. 3.2.3) into the Ta layer is two orders of magnitude smaller than the intrinsic damping of the permalloy layer for permalloy samples of these thicknesses. We utilized a wide variety of capping and seed layer combinations as a test of the robustness of the radiative damping analysis to sample structure details. Prior to deposition, the substrates are cleaned by Ar plasma sputtering. The samples are coated with approximately 150 nm of PMMA in order to avoid electrical shorting when samples are placed directly on the CPW.

3.2.1.3 Sample characterization

The FMR spectra of the samples were measured utilizing the vector-network-analyzer setup described in Sec. 2.1. An example of the obtained spectra including susceptibility fits is shown in Fig. 3.6 (a) and (b) for the Ta(3)/Py(200)/Si_3N_4(3) sample.

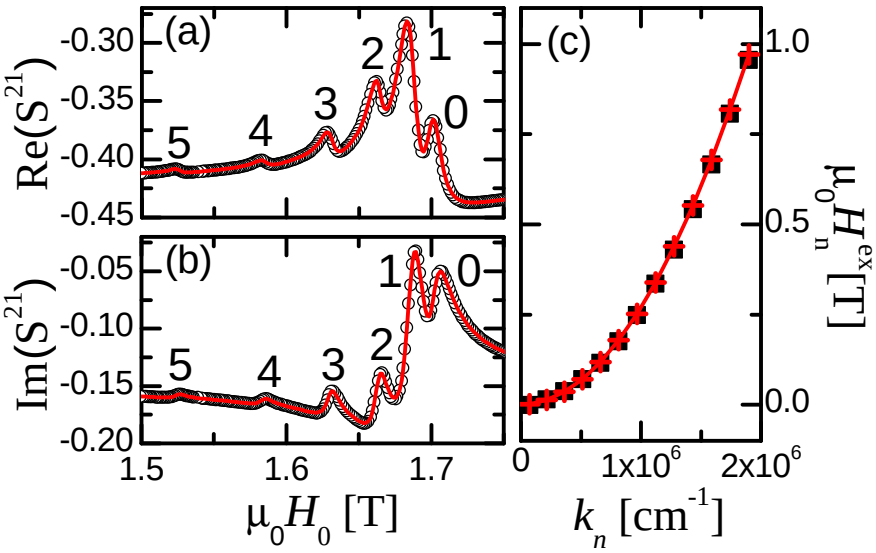

Figure 3.6: Measured S_{21} transmission parameter (black circles) at 20 GHz and the multi-peak -susceptibility fit (red line) for the (a) real part and (b) imaginary part obtained with the Ta(3)-Py(200)-Si_3N_4(3) sample. The first 6 modes are shown. (c) The exchange field H_n^{ex} (black squares) and exchange field fit, from Eqs. (3.38) and (3.39) (red crosses) for all 13 detected modes plotted as a function of the fitted wave numbers k_n.

Both even and odd PSSW modes are detected. Assuming a uniform excitation field and Dirichlet boundary conditions (completely pinned), only odd modes would be detected. Alternatively assuming Neumann boundary conditions (completely unpinned), only the fundamental mode would be detected.

Two effects can contribute to the ability to detect all the PSSW modes. First, the excitation field profile might not be uniform due to eddy current shielding [78,79]. Second, the interfacial boundary conditions might be asymmetrical, as alluded to above. According to the criterion in Ref. [78], the threshold sheet resistance for the onset of eddy current shielding at 20 GHz is 0.065 Ω/□. Estimating that the sheet resistance for our 200 nm is in excess of 0.345 Ω/□, it can be concluded that the eddy current shielding is relatively weak for all samples.

On the other hand, all modes are in principle detectable if we assume asymmetric interfacial anisotropy. For the sake of simplicity of the analysis, interfacial anisotropy for a single interface is assumed and then an optimization approach to determine the wavenumber of the modes that is consistent with such a hypothesis is applied. However, this approach does not provide a unique fit for the measured distribution of resonance fields for the PSSW spectrum, but simply allows to determine the wavenumber values required to be consistent with the measured spectrum. As such, the fitted value for K_s is to be interpreted as no more than a self-consistent value associated with only one of many possible scenarios.

Assuming negligible magnetocrystalline perpendicular anisotropy H_k, H_res is related to the exchange field via

$$\begin{aligned} H_\mathrm{res} &= H_n^\mathrm{ex} + M_\mathrm{s}, \\ \text{with } H_n^\mathrm{ex} &= \frac{2A_\mathrm{ex}}{\mu_0 M_\mathrm{s}} k_n^2. \end{aligned} \tag{3.38}$$

Here, k_n is the spinwave wavevector, and A_ex is the exchange energy that is related to the spinwave stiffness D via $D = \frac{2A_\mathrm{ex} g \mu_\mathrm{B}}{M_\mathrm{s}}$. On the other hand, in order to include interfacial anisotropy for a single interface in the analysis, the transcendental equation [80]

$$\left(-\frac{1}{2} k_n a + \frac{K_\mathrm{s}}{2A_\mathrm{ex} k_n} + 1\right) \tan(k_n \delta) = \frac{K_\mathrm{s}}{2A_\mathrm{ex} k_n} \,, \tag{3.39}$$

can be solved numerically, where K_s is the interfacial anisotropy, and $a = 0.3547\,\mathrm{nm}$ is the lattice constant [81]. The residue of the fit of Eq. (3.38) to H_res with the fitting parameters M_s, A_ex, and K_s from Eq. (3.39) is minimized by use of a Levenberg-Marquardt optimization algorithm. This yields the pairs (k_n,H_n^ex) shown in Fig.3.6 (c) for all modes. From the fit, a saturation magnetization of $\mu_0 M_\mathrm{s} = 1.02 \pm 0.01\,\mathrm{T}$ is obtained, in agreement with that determined by magnetometry. The exchange stiffness constant of $D = 3.22 \pm 0.04\,\mathrm{meVnm^2}$ is close to a value of $D \approx 3.1\,\mathrm{meVnm^2}$ reported by Maeda, *et al.* [82]. The exchange fit also yields a single surface anisotropy K_s that depends on the cap and seed layer configurations. For the Ta(3)-Py(δ)-Si_3N_4(3) sample series, $K_\mathrm{s} = (5.1 \pm 0.8) \times 10^{-4}\,\mathrm{J/m^2}$, while all the other samples have a higher K_s of $(7 \pm 1) \times 10^{-4}\mathrm{J/m^2}$. All values for K_s are in the range of other reported interface anisotropies for Permalloy layers of these thicknesses [83].

3.2.1.4 Application of the radiative damping model to experimental data

We now turn to the linewidth ΔH_n and the amplitude A_n for the individual modes. The Gilbert damping parameter α_n is extracted from the slope of the

linewidth vs. frequency f plot [84] shown in Fig. 3.7(a) via

$$\Delta H_n = \frac{4\pi\alpha_n f}{|\gamma|\mu_0} + \Delta H_n^0, \tag{3.40}$$

where ΔH_n^0 is the inhomogeneous broadening that gives rise to a nonzero linewidth in the limit of zero frequency excitation. The normalized inductance of the modes $\widetilde{L}_n$ is extracted in a similar fashion from the dependence of the mode amplitude A_n on the frequency f, see Fig. 3.7(b) and Eq. (3.29)

$$A_n = 2\pi f \frac{\widetilde{L}_n}{Z_0} + A_n^0, \tag{3.41}$$

where A_n^0 is an offset for each mode. A_n^0 is a phenomenological fitting parameter, which is not yet fully understood.

We plot α_n and $\widetilde{L}_n$ as a function of mode number n in Fig. 3.7 (c). The damping and the normalized mode inductance are found to be proportional.

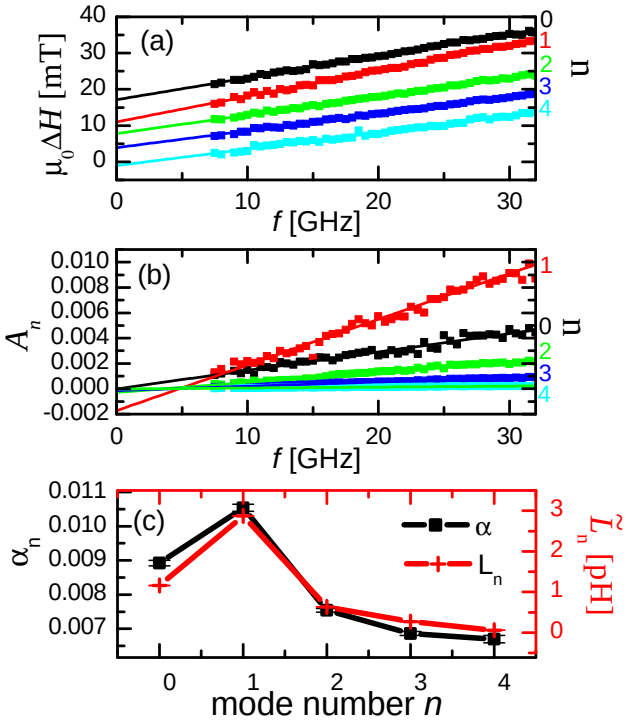

Figure 3.7: Parameter extraction for the first 5 PSSWs of the Ta(3)-Py(200)-Si_3N_4(3) sample. (a) Extraction of α from the linewidth $\mu_0\Delta H$ (data points) via linear fits (lines); staggered for display. (b) Extraction of the normalized mode inductance $\widetilde{L}_n$ (data points) from the resonance amplitude $A_n(f)$ via linear fits (lines). (c) α_n (black squares) and $\widetilde{L}_n$ (red crosses) for each PSSW.

In order to explore this correlation, we plot α_n vs. $\widetilde{L}_n$ in Fig. 3.8(a). Here, the data for α_n vs. $\widetilde{L}_n$ are linearly correlated for all modes except for $n = 0$, as seen by the linear fit (line) to the data for $n \geq 1$. This is as expected for the radiative damping model, as summarized in Eq. (3.32). The additional damping of the fundamental mode is interpreted as the result of eddy current damping, as quantified in Eq. (3.53).

In Fig. 3.8 (b), we plot the residual $\Delta\alpha_n$ of the linear fit shown in Fig. 3.8(a) for all modes. $\Delta\alpha_n$ is negligible for all modes except for $n = 0$. We extract $\Delta\alpha_{n=0}$ for all the samples and plot $\Delta\alpha_{n=0}$ vs. δ^2 in Fig. 3.8(c). It appears that $\Delta\alpha_{n=0}$ for all the samples scales linearly with δ^2, as expected from Eq. (3.53) for eddy current damping, compare Sec. 3.2.2. Simultaneous weighted fits of all the data to Eq. (3.53) yields $C = 0.4 \pm 0.1$. This value suggests a localization of eddy currents, since C corrects for the eddy current distribution in the sample.

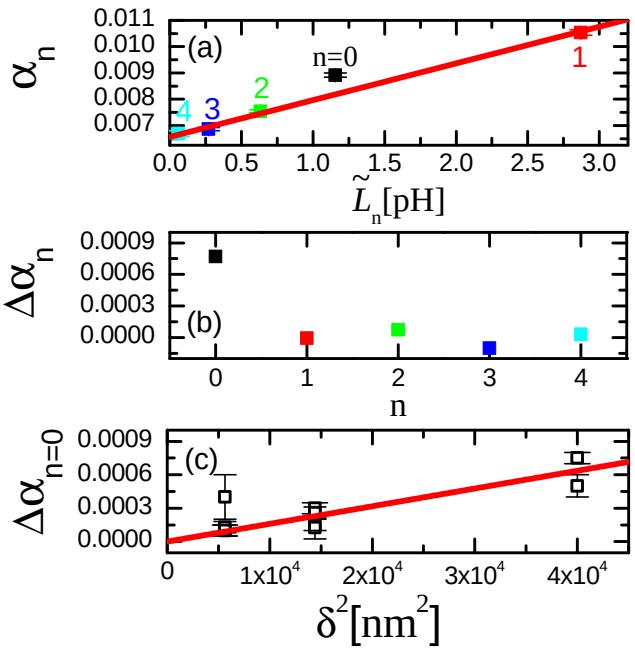

Figure 3.8: Damping α_n and inductance $\widetilde{L}_n$ for the Ta(3)-Py(200)-Si_3N_4(3) sample. (a) Linear fit of α to Eq. (3.32) where the fit is constrained to the n= 1, 2, 3, 4 modes. (b) The residual of the linear fit, showing enhanced damping for the 0-th order mode (black). We attribute the enhanced damping to an eddy current contribution. (c) Enhanced 0-th order mode damping for all samples. The red line is a fit of the data points to the eddy current damping model from Eq. (3.53).

For the $n \geq 1$ modes, it can be shown [85] that $\alpha_n^{\text{eddy}} \propto 1/k_n^2$. The calculated wavevectors from Eq. (3.39) for the $n = 1$ mode of all the samples is at least a factor three larger than that of the $n = 0$ mode and, therefore, the eddy current damping of the $n = 1$ mode is predicted to be approximately one order of magnitude smaller than the eddy current damping of the $n = 0$ mode. Thus, the eddy current damping of the $n \geq 1$ modes is negligible to within the error bars, i.e., $\alpha_n^{\text{eddy}} \approx 0$ for $n \geq 1$. This supports the analysis of the data in Ref. [86], which also neglects the eddy current damping in higher order modes.

By use of Eq. (3.53) and our fitted value of $C = 0.4$, we subtract the eddy current contribution to the damping of all the $n = 0$ modes to obtain a corrected damping value $\alpha'_{n=0}$, where $\alpha'_{n=0} = \alpha_{n=0} - \alpha^{\mathrm{eddy}}(C = 0.4)$. The corrected data for all the modes are plotted in Fig. 3.9.

Figures 3.9 (a) to (c) group all data obtained for a set of samples with identical Py thickness δ. The lines are linear fits to Eq. (3.32). For each thickness δ, we observe a significant correlation of α_n and $\widetilde{L}_n$ for all seed and cap layer configurations, as expected for a radiative damping mechanism.

Furthermore, by use of Eq. (3.36) for the $n = 0$ mode of the 75 nm thick sample, using a value of $\eta \approx 0.46$ as determined in the Appendix, we estimate $\alpha_0^{\mathrm{rad}} \approx 0.00023$

The experimentally determined value is $\alpha_0^{\mathrm{rad}} \approx 0.00035 \pm 0.0001$. The deviance from the calculated value is possibly due to non-uniformities of both the excitation field and magnetization profile in Eq. (3.36), that requires the solution of the integral in Eq. (3.16). Nevertheless the estimated value for α_0^{rad} is of the correct order of magnitude.

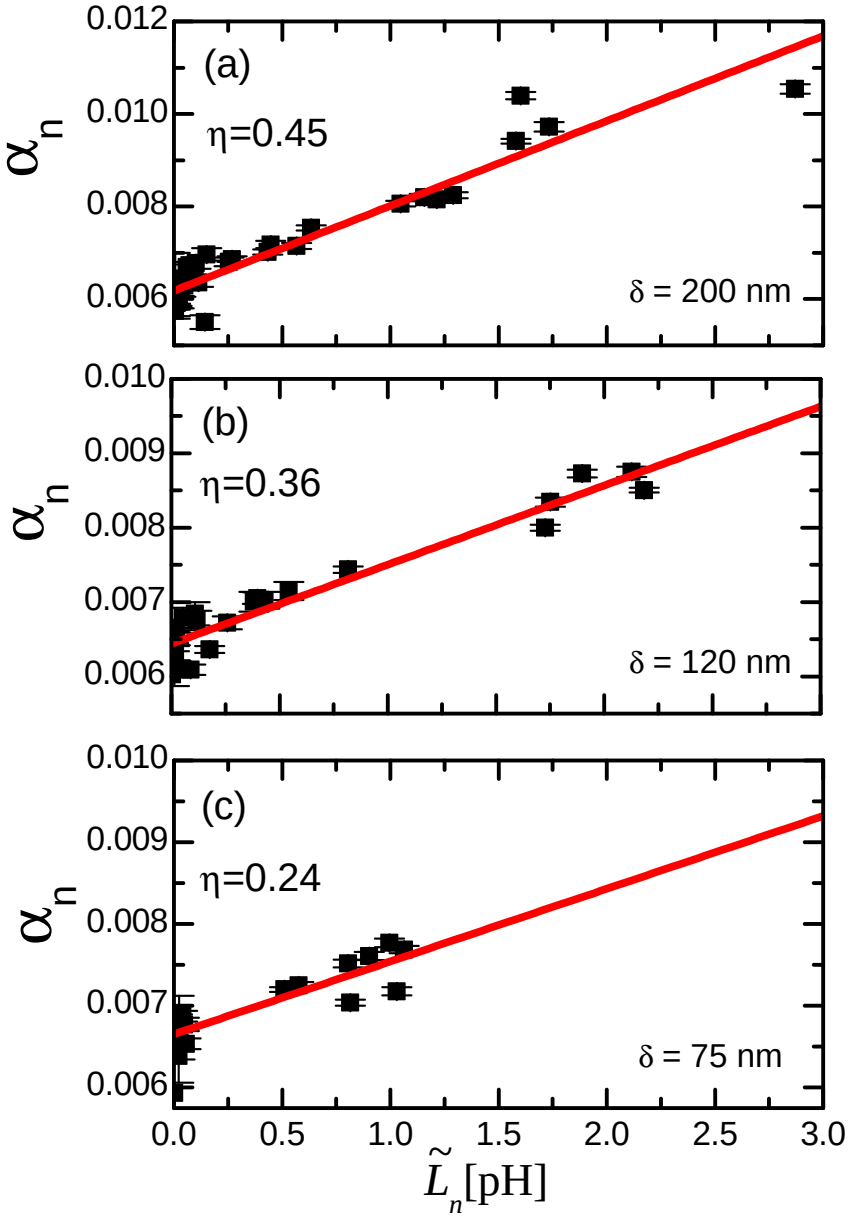

Figure 3.9: Dependence of damping α on the normalized mode inductance $\widetilde{L}_n$ after correction for the eddy current damping $\Delta\alpha_0$ of the fundamental mode, plotted for all sample configurations and different thicknesses: (a) $\delta = 200\,\mathrm{nm}$, (b) $\delta = 120\,\mathrm{nm}$ and (c) $\delta = 75\,\mathrm{nm}$. The red lines are weighted linear fits to the data by use of Eq. (3.32), that describes the radiative component of the damping.

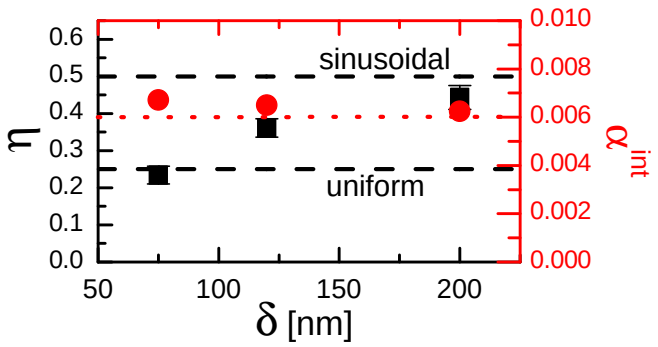

Figure 3.10: Mode profile parameter η (black squares, left axis) and intrinsic damping α_{int} (red circles, right axis) as a function of Py thickness δ. The mode profile parameter η lies between the value of 1/2 for sinusoidal PSSWs with anti-symmetric boundary conditions (dashed black line) and the value of 1/4 for the uniform mode (both dashed black lines). The intrinsic damping is close to $\alpha_{\text{int}} = 0.006$ (dotted red line).

We determine the intrinsic damping α^{int} from the $\widetilde{L}_n = 0$ intercept of the linear fits in Fig. 3.9. We plot α^{int} for the three values of δ in Fig. 3.10 (right scale). We find that α^{int} is approximately constant to within $\pm 5\%$ for all samples. In addition the average value over all the film thicknesses is in reasonable agreement to the previously reported value of α^{int}= 0.006 (dotted red line) [87].

The other fitting parameter η, extracted from the slope of α_n vs. $\widetilde{L}_n$, as an average of all cap and seed layer configurations for one thickness, is also plotted in Fig. 3.10 (left scale). The fitted out η displays robustness towards variation of the interface conditions. For anti-symmetric boundary conditions, $\eta = 1/2$ is expected, whereas for the uniform mode, $\eta = 1/4$.

We see that the fitted values lie exclusively within these extremes, within error bars. The dependence of η on δ still requires further investigation, but is beyond the scope of this work.

3.2.1.5 Application to fundamental mode FMR

In another experiment, we further validate the presence of radiative damping and demonstrate an alternative method to determine α_n^{rad} by varying the distance d in Eq. (3.5) between the sample and waveguide. To this end, we insert a $d = 200\,\mu\text{m}$ glass spacer between the sample and waveguide.

By comparing $h(0, 0)$ to $h(0, 200\,\mu\text{m})$ via Eq. (3.5), we estimate that the insertion of the spacer decreases the microwave magnetic field by about a factor of 6.25.

Referring to Eq. (3.31), the normalized mode inductance $\widetilde{L}_n$ decreases by a factor of $\cong 40$.

To determine the effect of the reduced inductive coupling on the radiative damping, we used VNA-FMR to measure the first 4 modes for the Ta(3)-Py(120) sample with and without the spacer. The effect of the spacer can be seen in the raw data, reducing the linewidth of the first two modes measured at 10 GHz in the 120 nm samples by approximately 6 Oe, well outside error bars. The fitted values of $\widetilde{L}_n$ are shown in Fig. 3.11 (a). Indeed, $\widetilde{L}_n$ decreases on average for all modes by a factor of $\cong$ 50 after inserting the spacer, in good agreement with the predictions of Eq. (3.5) and (3.31). Thus, we will assume that α_n^{rad} is negligible when the spacer is used. The data for the damping α_n of the first four modes, both with and without the spacer, are plotted in Fig. 3.11 (b). Indeed, the damping determined from the measurement with the spacer layer (circles) is consistently lower than that found without the spacer layer (squares). The line in Fig. 3.11 (b) is the previously determined intrinsic damping. Under the assumption that the radiative damping contribution is given by $\alpha_n^{\mathrm{rad}} = \alpha_n(d = 0) - \alpha_n(d = 200\,\mu\mathrm{m})$, we plot α_n^{rad} vs $\widetilde{L}_n(d = 0)$ in Fig. 3.11 (c). The line is the calculated α_n^{rad}, where we used Eq. (3.32) with $\eta = 0.35$ and $\delta = 120\,\mathrm{nm}$, as determined from the fits in Fig. 3.9. Good agreement between the calculated and measured values for α_n^{rad} are obtained, which demonstrates the self-consistency of our analysis. Of great importance is that the spacer-layer approach can also be used to determine the radiative contribution to the damping

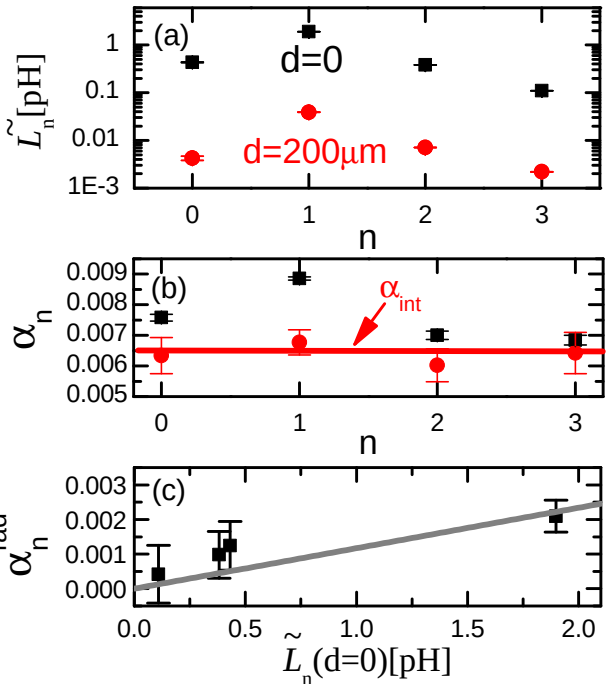

Figure 3.11: Measurement of the first four PSSWs of the Ta(3)-Py(120) sample with and without a spacer inserted between sample and CPW. (a) Inductance $\widetilde{L}_n$ determined for the sample directly on the CPW (black squares) and for a 200 µm spacer between sample and CPW (red circles). (b) The resulting damping constants for both measurements (same symbols and colors). The red line is the previously extracted intrinsic damping α^{int}. (c) The difference between the damping with and without the spacer (black squares) is in good agreement with the radiative damping from Fig. 3.9(b) (gray line).

in the absence of PSSWs (single resonance). By measuring α for varying distance d between sample and waveguide and extrapolating α to $d \to \infty$, both the intrinsic value for the damping and the radiative contribution can be determined, under conditions where eddy current damping is negligible.

3.2.2 Eddy current damping

As already stated in a previous section, the precessing magnetization induces eddy currents in a conducting sample, as described by Faraday's law. The induction of eddy currents leads to energy dissipation from the magnetic system, i.e. it causes another damping term α^{eddy}. For the derivation of the eddy current damping α_{eddy} uniform magnetization dynamics are assumed. The notation stays the same as for the radiative damping.

Then the total flux passing through the magnetic film is

$$\partial_t \Phi = \mu_0 \ell \delta (\partial_t \boldsymbol{m})_x, \tag{3.42}$$

where $(\partial_t \boldsymbol{m})_x = \hat{x} \cdot \partial_t \boldsymbol{m}$. The electrical power dissipated by the eddy-currents is

$$P_{\text{ind}} = \frac{1}{2} \frac{|\partial_t \Phi|^2}{\left(\frac{2\rho\ell}{\delta_{\text{eff}} W}\right)} \tag{3.43}$$

$$= \frac{C}{8} \frac{\mu_0^2 \delta^3 \ell W}{\rho} |(\partial_t \boldsymbol{m})_x|^2, \tag{3.44}$$

with $\delta_{\text{eff}} := C\delta/2$, where $0 \leq C \leq 1$ is a phenomenological parameter that accounts for details of the non-uniform eddy-current distribution in the ferromagnet. Analogous to the derivation of the radiative damping, we now need the energy of the magnetic excitations. The number of magnons in the system is given by

$$N_{\text{mag}} = \frac{M_s}{g\mu_B \omega^2} |\partial_t \boldsymbol{m}|^2. \tag{3.45}$$

Thus, the total magnon energy is

$$E_{\text{mag}} = \hbar\omega N_{\text{mag}} W \ell \delta \tag{3.46}$$

$$= \frac{M_s}{\gamma\omega} |\partial_t \boldsymbol{m}|^2 W \ell \delta. \tag{3.47}$$

The rate of energy dissipation is then given by

$$\frac{1}{T_1} = \frac{P_{\text{ind}}}{E_{\text{mag}}} = \frac{C}{8}\frac{\gamma\omega\mu_0^2 M_s \delta^2}{\rho}\frac{\left|\left(\partial_t \boldsymbol{m}\right)_x\right|^2}{\left|\partial_t \boldsymbol{m}\right|^2}. \tag{3.48}$$

The maximum energy decay rate occurs when $\left(\partial_t \hat{m}\right)_x = \left|\partial_t \hat{m}\right|$, in which case

$$\left(\frac{1}{T_1}\right)^x = \frac{C}{8}\frac{\gamma\omega\mu_0^2 M_s \delta^2}{\rho}, \tag{3.49}$$

where the superscript indicates that this is the maximum decay rate for magnetization oscillations along the x-axis. For the case of a perpendicular applied field sufficient to saturate the static magnetization out of the film plane, the damping process is isotropic, i.e.,

$$\left(\frac{1}{T_1}\right)^y = \frac{C}{8}\frac{\gamma\omega\mu_0^2 M_s \delta^2}{\rho}. \tag{3.50}$$

Therefore, analogous to Eq. (3.21), the frequency-swept linewidth $\Delta\omega$ is simply

$$\Delta\omega = \frac{\left(\frac{1}{T_1}\right)^x + \left(\frac{1}{T_1}\right)^y}{2} \tag{3.51}$$

$$= 2\alpha^{\text{eddy}}\omega, \tag{3.52}$$

then

$$\alpha^{\text{eddy}} = \frac{C}{16}\frac{\gamma\mu_0^2 M_s \delta^2}{\rho}. \tag{3.53}$$

3.2.3 Spin pumping

The emission of a pure spin current from a magnetic layer (FM) in FMR into a non-magnetic adjacent layer (NM) is usually referred as spin pumping. The spin current, injected into the NM, takes the form [50]

$$\boldsymbol{j_s} = \frac{\hbar}{4\pi} Re(g^{\uparrow\downarrow}) \boldsymbol{m} \times \partial_t m + Im(g^{\uparrow\downarrow}) \partial_t m, \tag{3.54}$$

where $g^{\uparrow\downarrow}$ is spin mixing conductance, defined as [88]

$$g^{\uparrow\downarrow} = S^{-1} \sum_{nm} \left(\delta_{mn} - r^{\uparrow}_{mn} r^{\downarrow *}_{mn} - t'^{\uparrow}_{mn} t''^{\downarrow *}_{mn} \right). \tag{3.55}$$

Here, m and n are states at the Fermi energy in the NM and $r^{\uparrow\downarrow}_{mn}$ and $t'^{\uparrow\downarrow}_{mn}$ are the the reflection and transmission amplitudes of an incoming electron in state m, being reflected (transmitted) into state n. The area of the FM/NM interface is S. The real part of $g^{\uparrow\downarrow}$ is always positive and the imaginary part of $g^{\uparrow\downarrow}$ is small [88] and will be neglected in the following. Emission of a spin current entails a loss of angular momentum in the magnetic system, thus opening up a channel for energy dissipation, resulting in an additional contribution to the measured damping. This becomes obvious when comparing Eq. 3.54 to the damping term in Eq. 2.1. Since its discovery and first successful theoretical description [45] spin pumping [72,88–90] and related effects such as the spin Hall effect (SHE) [91,92] have been the focus of significant research effort. In this paragraph however, spin pumping will only be treated phenomenologically as an additional contribution to the damping, as an in-depth discussion of the origin and theoretical description is beyond the scope of this thesis. Details about the theoretical description of spin pumping can for example be found in Ref. [93] For a ferromagnet in contact with a non-magnetic conductor, the damping due to spin pumping α_{sp} can be written as [50]

$$\alpha_{\mathrm{sp}} = \frac{g^{\uparrow\downarrow}_{\mathrm{eff}} \mu_{\mathrm{B}} g}{4\pi M_{\mathrm{s}} t}. \tag{3.56}$$

$g^{\uparrow\downarrow}_{\mathrm{eff}}$ is the effective spin mixing conductance, a parameter quantifying the effectiveness of spin pumping. Simplified speaking, $g^{\uparrow\downarrow}_{\mathrm{eff}}$ depends on the band overlap at the interface, but also includes spin back-flow in the case of a non-perfect spin sink.

Experimentally, α_{sp} can be determined by measuring the damping of samples with varying thickness t of the ferromagnetic layer. After accounting for other thickness dependent contributions to the damping, like eddy current damping and radiative damping, α_{sp} is then straightforwardly determined for any thickness, by fitting Eq. (3.56) to the thickness dependent damping with $g_{eff}^{\uparrow\downarrow}$ fitting parameter, as exemplary shown in Fig. 3.12 for a thickness series of $Co_{25}Fe_{75}$ samples. In a $1/t$ plot the damping also exhibits a non zero offset, which is interpreted as the bulk value of the damping. The measurement of α_{sp} in such a way is only possible for sample with a thickness large enough that the electronic band structure is not significantly influenced by the interfaces. Interfacial modification of the band structure will have a hard to predict influence on the damping and therefore cause behavior diverging from the spin pumping model. An example for this is included in Fig. 3.12, where the damping of the 1 nm $Co_{25}Fe_{75}$ sample diverges from the linear $1/t$ behavior of all other samples.

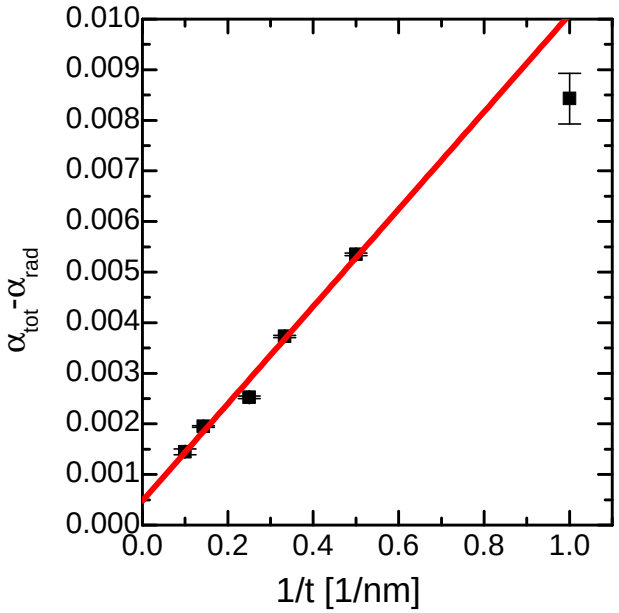

Figure 3.12: The measured damping α_{tot} of a thickness series of $Co_{25}Fe_{75}$ samples cleared of the radiative contribution α_n^{rad} is plotted against $1/t$. The red line is a linear fit to the data, excluding the 1 nm data point, which clearly deviates from the linear dependence on $1/t$ of the other data points.

3.2.4 The total measured damping

The measured damping α_{tot} consists to varying degrees of all in the previous sections discussed extrinsic damping mechanisms. However, they exhibit different dependence on sample geometry, in particular on sample thickness, as expressed in Eqs. (3.56), (3.53), and (3.32). The goal of this section is to illustrate the thickness dependence of α_{sp}, α_{eddy}, and α_{rad} and to give estimates of their magnitude for Ni, Fe, Co $Ni_{80}Fe_{20}$, and YIG, which are typically investigated materials. Fig. 3.13 depicts a calculation of the thickness dependence of the different contributions to the damping of a uniform FMR spin wave mode. For the calculations values of M_s and g are taken from Sec. 4.3 and bulk values for the resistivity are

i

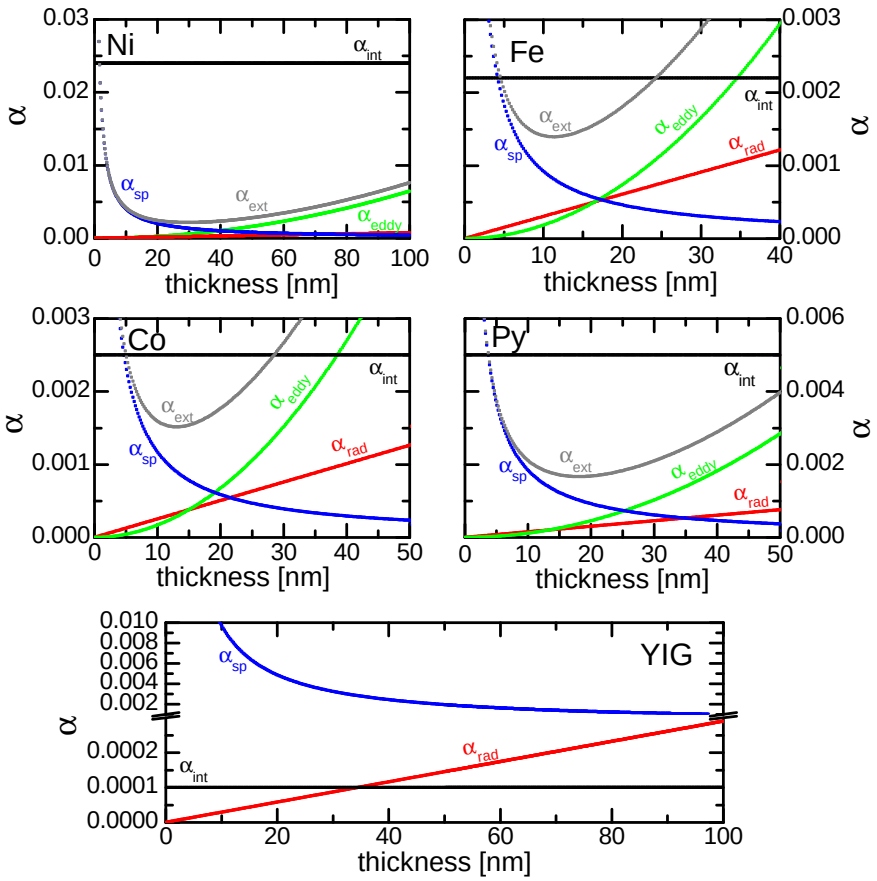

Figure 3.13: Calculated values for the extrinsic mechanisms α_{rad} (red lines), α_{sp} (blue lines), α_{eddy} (green lines), and the sum of the extrinsic contributions α_{ext} (grey lines) in Fe, Ni, Co, $Ni_{80}Fe_{20}$, and YIG are plotted against sample thickness. α_{int} (black lines) for each material system is plotted for comparison.

assumed. The estimate for α_{sp} is based on a effective spin mixing conductance of $1 \cdot 10^{19} m^{-2}$, a value well within the scatter or reported data [94]. Values of α_{rad} are based on a measurement geometry where the waveguide width is 100 µm and the sample length on the waveguide is 10 mm. α_{sp} becomes the dominating effect for thin samples ($\alpha_{\mathrm{sp}} \propto 1/t$), α_{eddy} dominates for thick samples ($\alpha_{\mathrm{eddy}} \propto t^2$), and α_{rad} increases linearly with thickness.

For comparison α_{int} and the sum of the discussed extrinsic contributions α_{ext} for the different materials are also plotted in Fig. 3.13. α_{ext} displays a minimum at a characteristic thickness, which is determined by material parameters. The larger M_{s} or g, the lower the thickness for which the minimum in α_{ext} occurs. It is no-

table that for materials with low intrinsic damping (Fe, Co, $Ni_{80}Fe_{20}$, and YIG) α_{rad} and α_{eddy} are already of the same order of magnitude as α_{int} for thicknesses of $\approx 20\,\mathrm{nm}$, showing the importance of accounting for these contributions to the total damping for many sample geometries.

In a more realistic calculation α_{eddy} would regress stronger for lower thicknesses, since the resistance typically increases for thinner samples. [95, 96] Furthermore, for larger thicknesses α_{eddy} will not follow a strict t^2 dependence, as the spin waves becomes less uniform and more localized due to eddy current shielding. [78, 79] A similar argument can be made for α_{rad}, since its value depends on the spin wave mode profile, as shown in Sec. 3.2.1.1. However, for the thicknesses shown in Fig. 3.13 the assumptions made result in reasonable values for the different extrinsic contributions.

4

Magnetic properties of binary 3d transition metal alloys

The results presented in this section have been published in Refs. [97] and [98]. For the development of new magnetic devices such as spin-transfer-torque random access memory (STT-RAM) [99, 100] or spin torque oscillators (STOs), the magnetic properties of each layer must be tuned according to the specifics of the application. 3d transition metal alloys, such as the binary alloys of NiCo, NiFe and CoFe, exhibit a wide range of magnetic properties that were thoroughly investigated with bulk samples in the 1960s and 1970s [101–103]. However, many emerging technologies require use of films of these materials as thin as a few monolayers. Such thin films can exhibit substantially modified magnetic properties from the bulk, including interfacial anisotropy [104, 105], strain induced anisotropy [106–108], reduction of Tc [109, 110], or modification of the magnetic moment [111]. While there have been a number of investigations of materials as thin films [112–117], there is not yet in the literature a comprehensive and systematic study of 3-d transition metal alloy films that spans the full alloy composition range from pure Fe to pure Ni, which also makes use of contemporary high-precision characterization methods such as broad-band ferromagnetic resonance (FMR) or high-resolution X-ray diffraction (XRD). A precise measurement of the magnetic properties for this relatively simple alloy system will facilitate their use in devices, as well as the development of new alloy systems. We therefore investigated the alloys NiCo, NiFe and CoFe over the full range of compositions. To this end, we determined the in-plane lattice constant and crystalline structure via XRD, the saturation magnetization density Ms via SQUID, as well as the perpendicular anisotropy and the interfacial orbital magnetic moment via FMR. The data presented here are not only a glossary of high-precision measurements of the thin-film magnetic properties in Ni_xCo_{1-x}, Ni_xFe_{1-x} and Co_xFe_{1-x}, but will also facilitate future testing of predictions based on theoretical calculations, e.g. density functional theory.

4.1 Samples and Method

We DC magnetron sputter deposited Ni_xCo_{1-x}, Ni_xFe_{1-x}, and Co_xFe_{1-x} alloys, spanning the full range of composition (i.e., from $x = 0$ to $x = 1$), on thermally oxidized (001) Si substrates at an Ar pressure of 0.67 Pa ($5 \cdot 10^{-3}$ Torr) in a chamber with a base-pressure of less than $5 \cdot 10^{-6}$ Pa ($4 \cdot 10^{-8}$ Torr). A Ta(3 nm)/Cu(3 nm) seed layer and Cu(3 nm)/Ta(3 nm) cap layer was used to maintain good adhesion to the substrate, promote high quality textured crystalline structure, prevent oxidation of the alloy layer, and to produce approximately symmetric interfaces and boundary conditions for the excited magnetization. A representation of the sample stack is shown in Fig. 4.1. The alloys were co-sputtered from two targets with the deposition rates determined by X-ray reflectivity (XRR). Drift in the deposition rates were periodically monitored with XRR and the repeatability of the deposition rates was found to be better than 3 % over the course of the study. For all deposited alloys the combined deposition rate was kept at approximately 2.5 Å/s to ensure similar growth conditions. In order to quantitatively account for interfacial effects we also deposited a thickness series that typically included 10 nm, 7 nm, 4 nm, 3 nm and 2 nm thicknesses of the pure elements and selected intermediate alloy concentrations $(Ni_{63})Co_{37}$, $Ni_{20})Fe_{80}$, $Ni_{50})Fe_{50}$, $Co_{85})Fe_{15}$, $Co_{50})Fe_{50}$, $Co_{25})Fe_{75}$ and $Co_{20})Fe_{80}$). Following deposition, the samples were coated with ≈ 150 nm PMMA. The FMR characterization and data analysis was performed with the field-swept Vector-Network-Analyzer (VNA)-FMR setup, as depicted in Fig. 2.2. The width of the CPW center conductor was 100 µm. In this setup, the VNA is connected to both ends of the CPW and the complex S_{21} transmission parameter for microwaves with frequencies ranging from 10 GHz to 40 GHz is measured. The signal is fitted and the effective magnetic field M_{eff} and the Landé g-factor are determined from the resonance field H_{res} vs. frequency f plot, as described in Sec. 2.1. An example of the raw data with fits is shown in Fig. 4.2.The extracted values for g and M_{eff} are then corrected for errors stemming from the limited measured frequency range via the method described by Shaw, *et al.* [118].

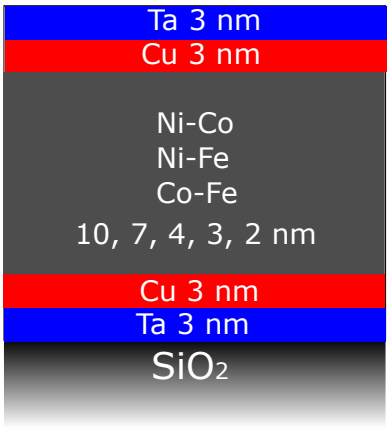

Figure 4.1: Sketch of the layer stack utilized for the binary alloy measurements.

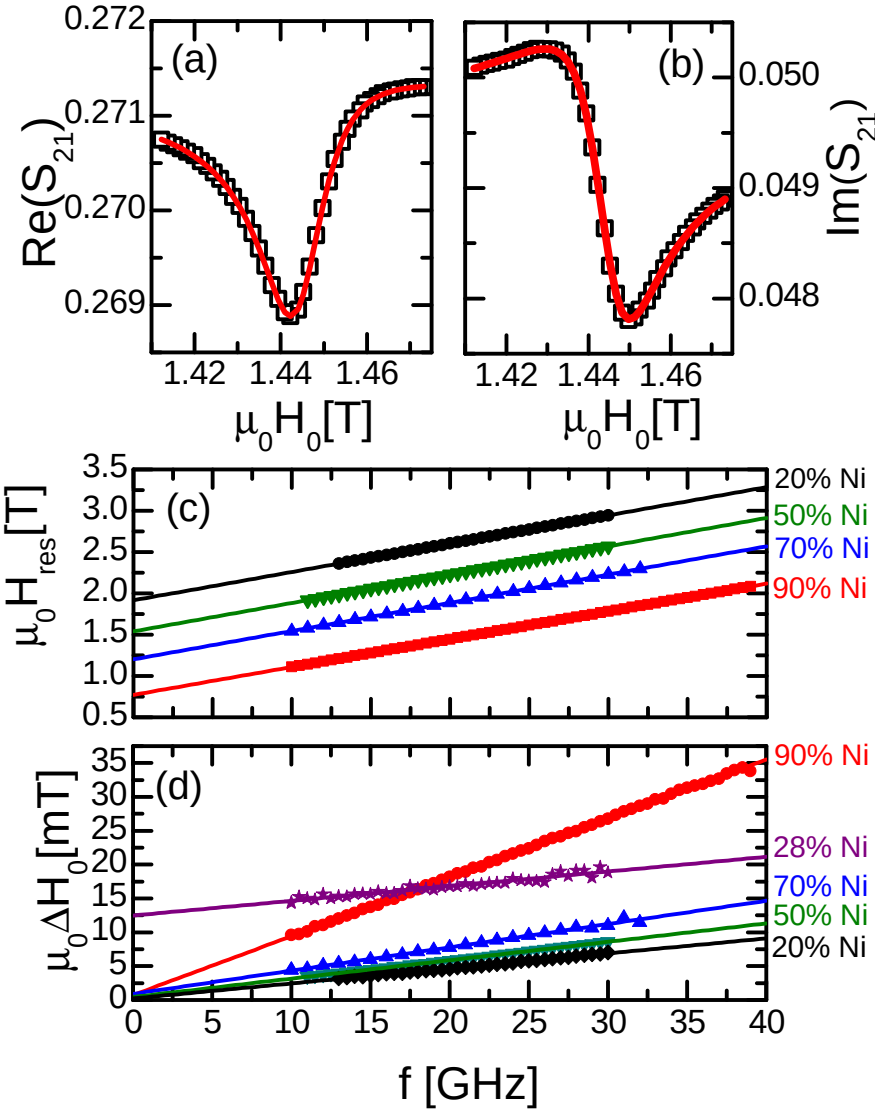

Figure 4.2: (a) and (b) show respectively the real and imaginary part of the S_{21} transmission parameter (black squares) with the complex susceptibility fit (red lines) for the $Ni_{90}Fe_{10}$ alloy with a thickness of 10 nm measured at 20 GHz. In (c) the resonance fields of four NiFe alloys are plotted against the frequency (data points) and fitted linearly (lines) with Ni concentrations denoted on the right axis. The zero-frequency intercepts of the linear fits determine the effective magnetization and their slope is inversely proportional to the g-factor. (d) shows the linewidth ΔH for the same alloys. The lines are fits of Eq. (2.4) to the data.

4.2 XRD characterization

The crystal structure was characterized by in-plane X-ray diffraction (XRD) using parallel beam optics with a Cu K_α radiation source. Fig. 4.3 shows the in-plane lattice constants, determined from the [211] bcc and [111] fcc peaks in the diffraction spectra. The Cu (220) peak is always visible in the spectra due to the Cu seed and cap layers used in all the samples. This complicates the analysis since the location of the face-centered-cubic (fcc) to body-centered-cubic (bcc) phase transition for the NiFe and CoFe alloys cannot be determined exactly. However, the change in the fcc lattice constant away from the bulk Cu value, as well as the diminishment and disappearance of the observed bcc peak, allows us to determine a concentration window in which a mixed phase occurs near the phase transition. Furthermore, we determined the texture of the bcc and fcc phases to be (110) and (111), respectively.

The NiFe alloys exhibit a bcc phase and unchanging bcc lattice constant for a Ni concentration between 0 % and 20 %. For Ni concentrations between 20 % and 30 % a mixed phase is measured as determined by the change in the fcc lattice constant to lower values than for fcc Cu, indicating the formation of an fcc phase in co-existence with a bcc phase, as seen in Fig. 4.3 (b). The location of this transition is also consistent with the concentration previously reported in the bulk NiFe system at 30 % Ni [42]. For Ni concentrations above 30 % the NiFe alloys exclusively exhibit fcc phase, with a lattice constant that approaches the value for pure bulk Ni as the Ni concentration increases. The CoFe system also exhibits a similar behavior as the NiFe samples. The alloys are purely bcc up to a Co concentration of 60 %, followed by an fcc to bcc phase transition in the vicinity of 70 % Co. This phase transition is again confirmed by XRD, but for the same reason as for the NiFe system, we could only determine that the exact location of the bcc to fcc phase transition occurs somewhere between 60 % and 80 % Co, where bcc and fcc phases co-exist, as shown in Fig. 4.3 (c). This phase transition seems to occur at a lower Co concentration than for the bulk alloy system [42], which can be attributed to the Cu seed layer, as elaborated in the next paragraph. Above 80 % Co the CoFe alloys exhibit purely fcc phase. Our pure Co films do not exhibit an hcp crystal structure, in contrast to prior reports in the literature [42]. Figure Fig. 4.3 (d) shows the XRD spectrum in the vicinity of the hcp(010) peak for the 10 nm pure Co sample, with a Ta/Cu seed and a Cu/Ta cap layer. For comparison, we include a similar Co film that was grown with only Ta only as seed and capping layers. The sample with only Ta in the seed and capping layer exhibits a clear hcp(010) peak, indicating an hcp structure. In contrast, the sample that includes Cu in the seed and capping layers shows no evidence of hcp structure. We conjecture that the strained growth of Co on Cu promotes a strained fcc (i.e. fct) phase in the Co, instead [119], which

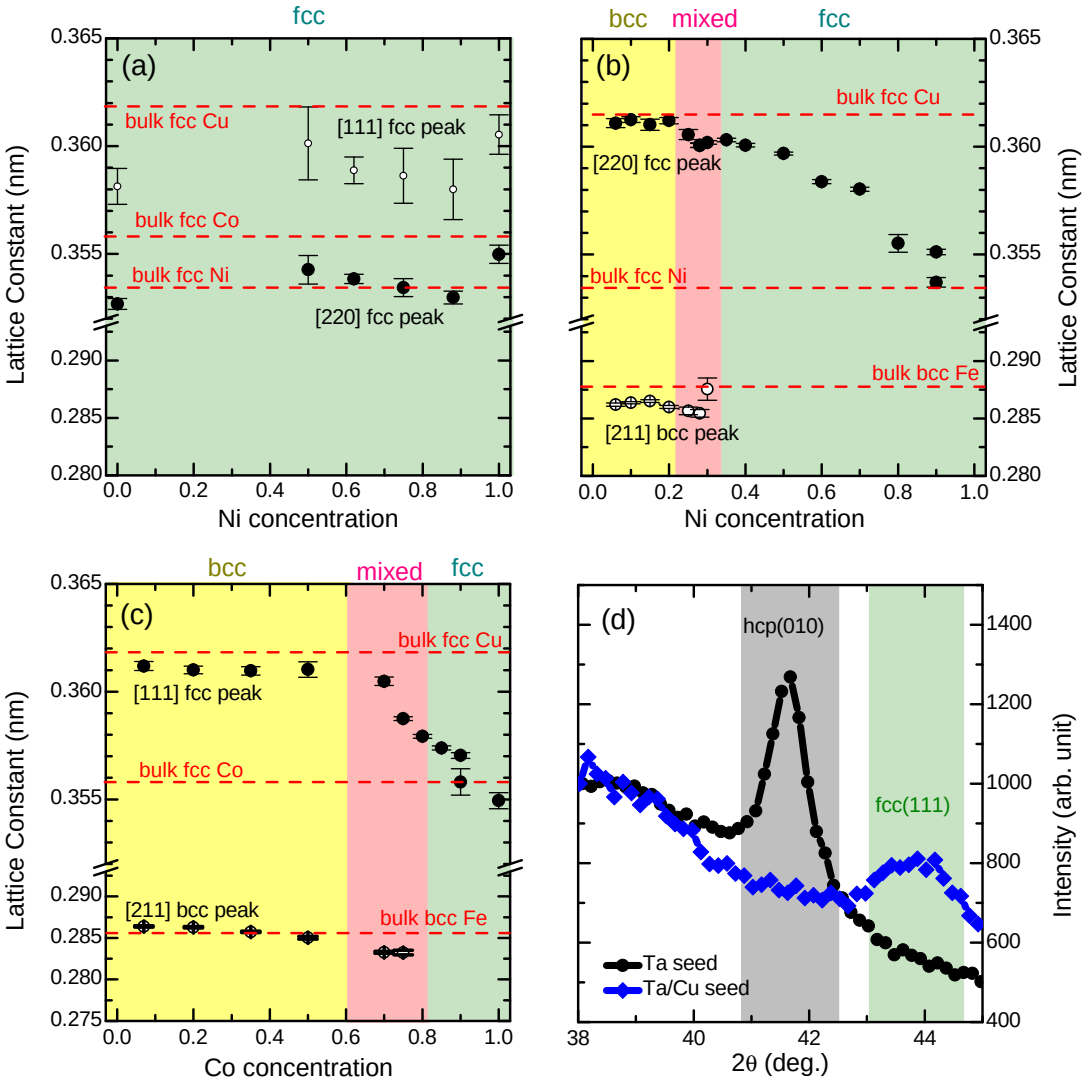

Figure 4.3: The in-plane lattice constants for (a) NiCo, (b) NiFe and (c) CoFe, determined by XRD. Note that the fcc lattice constants are always a superposition of the Cu lattice constants and the fcc part of the alloy. (d) shows XRD spectra for pure Co grown on a Ta seed layer and a Ta/Cu seed layer. The Co grown on Ta shows a clear hcp peak, while the one grown on Ta/Cu only exhibits a fcc peak.

is consistent with the structure reported for room-temperature growth of Co/Cu layers via molecular epitaxy [119–121]. The crystalline phase of the NiCo alloys is found to be exclusively fcc and exhibits distinguishable fcc(111) and fcc(220) peaks. The first peak, with its larger lattice constant, can be attributed to Cu, while we attribute the second peak to the CoNi.

4.3 Static magnetic properties

The saturation magnetization M_s of binary 3d transition metal alloys has first been successfully described by the Slater-Pauling model [122,123], which is based on a rigid band model. Simplified speaking alloying a 3d ferromagnet with another element changes the Fermi energy, shifting the occupation of the magnetic d-states around the Fermi energy. Assuming rigid bands, this occupation shift then directly translates into a change in magnetization, leading to the basic triangular shape of the Slater-Pauling curve [42,69,74]. In the NiFe and CoFe alloy systems transitions from a bcc (body-centered-cubic) to a fcc (face-centered-cubic) phase occur, causing change in the electronic band structure, leading to further features in the Slater-Pauling curve: In the CoFe and NiFe alloys, a drop or local minimum of magnetic moment is typically observed, respectively, at the phase. When it was initially discovered, the Slater-Pauling behavior was understood in terms of a rigid band model for magnetism in the 3-d metals. The rigid band model has since been discredited both theoretically and experimentally, but the empirical power of the Slater-Pauling behavior remains a corner-stone of alloy engineering with the 3-d metals. In order to refine theoretical predictions of the magnetization of alloy systems, the microscopic band structure, beyond the rigid band model has to be known, since alloying influences the band structure, for example by smearing out the bands due to disorder [74]. Furthermore, other magnetic properties like orbital magnetization or magnetic anisotropy cannot be described semi-classically and are purely quantum mechanical in origin. [124]

4.3.1 Magnetization

We determined the room temperature (RT) saturation magnetization M_s for all samples via superconducting quantum interference device (SQUID) magnetometry. The samples were first diced with a precision diamond saw such that the surface area of the sample is accurately known. The saturation magnetization M_s for all alloy samples is then determined by dividing the measured magnetic moment to the volume. The sample volumes were corrected to account for interfacial factors, like the existence of a dead layer or alloying with the Cu cap and seed

layers. Such interfacial effects on the magnetization are determined in a thickness series for select alloys, measured with FMR. The M_{eff} vs. 1/t plot plots (not shown) show a non-zero $M_{\text{eff}} = 0$ intercept of $0.7\,\text{nm}^{-1}$, indicating the existence of either a $0.7 \pm 0.3\,\text{nm}$ magnetic dead layer, or a layer of reduced magnetization corresponding to a thickness of approximately two mono-layers on each interface for all measured samples. The determined thicknesses of the dead layers display no discernible trend for alloy composition. The existence of a dead layer of this thickness has been found for Fe and $Ni_{80}Fe_{20}$ at similar interfaces [125, 126]. Accounting for the 0.7 nm dead layer, the SQUID measurements are normalized to the alloy volume and the resulting M_{s} for all alloys is plotted in Fig. 4.4 (a)-(c) (blue triangles). For the NiCo alloys M_{s} decreases almost linearly with increasing Ni concentration from $\mu_0 M_{\text{s}}(\text{Co}) = 1.77 \pm 0.04\,\text{T}$ to $\mu_0 M_{\text{s}}(\text{Ni}) = 0.51 \pm 0.03\,\text{T}$. In the NiFe alloy system M_{s} increases from $\mu_0 M_{\text{s}}(\text{Fe}) = 2.05 \pm 0.02\,\text{T}$ to a maximum of $2.12 \pm 0.06\,\text{T}$ at 10 % Ni followed by a minimum at the phase transition (25 % Ni). At Ni concentrations greater than 40 % M_{s} decreases again with increasing Ni concentration. M_{s} of the CoFe alloys shows a maximum of $2.42 \pm 0.05\,\text{T}$ at approximately 35 % Co followed by a decrease with higher Co concentration and a drop at the phase transition.

This behavior for M_{s} is consistent with the often-observed Slater-Pauling curve [122, 123, 127], which is included in Fig. 4.4 as the gray dotted lines. The only deviations occur in the vicinity of the NiFe and CoFe phase transitions. In those cases, the dip or drop in the curve occur at lower Ni or respectively Co concentration than in the bulk Slater-Pauling curve. This is consistent with our XRD measurements that indicate promotion of the fcc phase by the Cu substrate, which causes small deviations relative to the bulk phase diagram. The effective magnetization M_{eff} is determined by use of Eq. (2.3) to analyze the FMR data. Assuming purely interfacial perpendicular anisotropy, i.e. negligible bulk perpendicular anisotropy, the saturation magnetization M_{s} can also be determined by measuring M_{eff} in a thickness series (10 nm, 7 nm, 4 nm, 3 nm, 2 nm) and determining the y-intercept (corresponding to infinite thickness t) when M_{eff} is plotted versus $1/t$. This is done for a select number of alloys and the resulting values of MS determined from FMR are also included in Fig. 4.4 (red crosses). These values for M_{s} agree well with the values of M_{s} determined by SQUID, demonstrating the equivalency of both measurement methods. Furthermore, the determined M_{eff} for the 10 nm thick alloy samples for all concentrations is plotted in Fig. 4.4 (black squares). M_{eff} generally follows the Slater-Pauling curve with an offset due to the presence of interfacial perpendicular anisotropy.

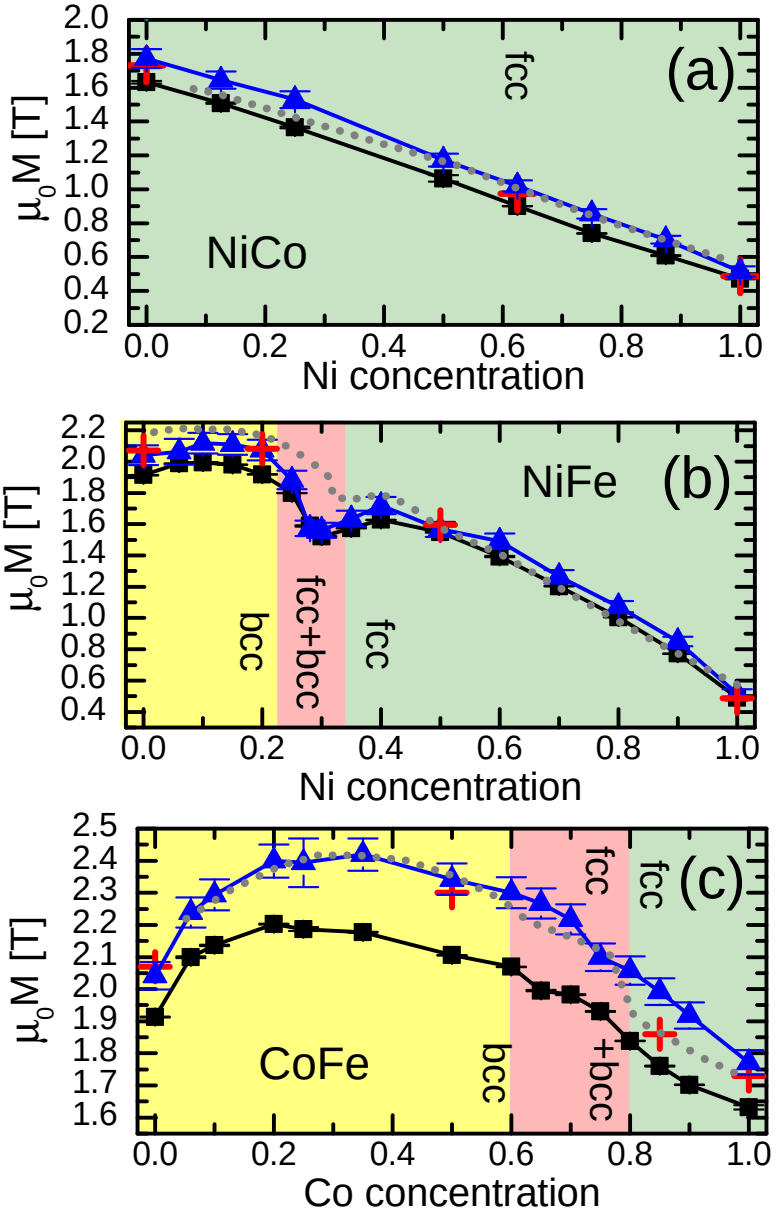

Figure 4.4: RT effective magnetization M_{eff} (black squares), measured via FMR,and the RT saturation magnetization M_{s} (blue triangles), measured via SQUID magnetometry, are plotted in (a) for NiCo, in (b) for NiFe and in (c) for CoFe. For comparison, M_{s} is also determined by linear regression of M_{eff} vs. $1/t$. The extrapolated values for M_{s} are included the plots as red crosses. They match M_{s} by SQUID at those alloy concentrations reasonably well. This shows that the SQUID and FMR measurements are consistent. The crystal structure of the alloys is denoted and signified in the same color code as in Fig. 4.3. For comparison the bulk Slater-Pauling curves for the three alloy systems are also plotted (gray dotted lines) [42].

4.3.2 Perpendicular magnetic anisotropy

As already stated, the difference between M_{eff} from FMR and M_{s} from magnetometry is the result of interfacial perpendicular anisotropy H_k, which results from the broken symmetry at the interfaces [128, 129]. Despite being purely interfacial, this interface anisotropy acts on the whole film in the thin film limit and is therefore often employed to engineer the anisotropy according to certain specifications, in particular for perpendicularly magnetized materials [130–133]. Defining the anisotropy energy as in Ref. [105], the effective total perpendicular anisotropy energy density K can be determined from M_{s} and M_{eff} via [109] $K = 1/2(M_{\text{s}} - M_{\text{eff}})M_{\text{s}}\mu_0$, and is plotted as a function of alloy concentration in Fig. 4.5. Note here that we do not separate the different contributions to K (second and fourth order anisotropy constants) [56]. For the NiCo alloy, K decreases almost linearly from pure Co to pure Ni. For the NiFe alloys K has a sharp minimum at the phase transition. We speculate that the minimum is due to the coexistence of multiple phases with compensating amounts of anisotropy. Then, with higher Ni content, K decreases almost linearly. The CoFe alloys behave in a very different manner. Thin films of pure Co and Fe exhibit similar anisotropies, but their alloys have higher values for the anisotropy, up to $2.3 \cdot 10^5\,\text{J/m}^3$, as shown in Fig. 4.5 (c). At a Co concentration of 75 % near the fcc to bcc phase transition, K exhibits some degree of distortion. If we assume that M_{s} is independent of thickness for thicknesses as small as 2 nm or greater (e.g. Cu does not alloy with the magnetic films), the bulk anisotropy K_{vol} and the average interfacial anisotropy K_{int} can be determined from the thickness dependence of the total anisotropy K by use of the phenomenological equation $K(t) = K_{\text{vol}} + 2K_{\text{int}}/t$ [134] (the factor of 2 accounts for the number of interfaces), where fits of the data based on this equation are presented in the right panels in Fig. 4.5. We plot the extracted volume and interface components of K against their respective atomic number in Fig. 4.5 (d) and (e). K_{vol} is small to negligible and shows no discernible trend with alloy composition. The interface components of the total perpendicular anisotropy for the $Co_{33}Ni_{67}$ alloy is in the range of the one reported by Shaw, *et al.* [134] of $2K_{\text{int}} = 1.56 \cdot 10^{-4}\,\text{J/m}^2$ for a $(CoFe)_{25}Ni_{75}$ alloy with the same seed and cap layers as used in this study.

K_{int} exhibits similar Slater-Pauling behavior as the magnetization data in Fig. 4.4. This behavior gives an indication that there is a certain amount of interfacial anisotropy energy per uncompensated d-band spin, i.e. the anisotropy energy is proportional to the spin density at the interface. In Fig. 4.6 we plot the interface anisotropy against areal spin density and indeed K_{int} increases with the areal spin density. A linear fit to the data yields an x intercept of $(23 \pm 7)\mu_{\text{B}}/m^2$, which translates to a magnetization of $(0.7 \pm 0.2)\ \mu_{\text{B}}$ per interface atom. Considering the symmetry at the 3d transition metal alloy/Cu interface a nonzero x intercept seems reasonable. The symmetry of the localized alloy d-bands is

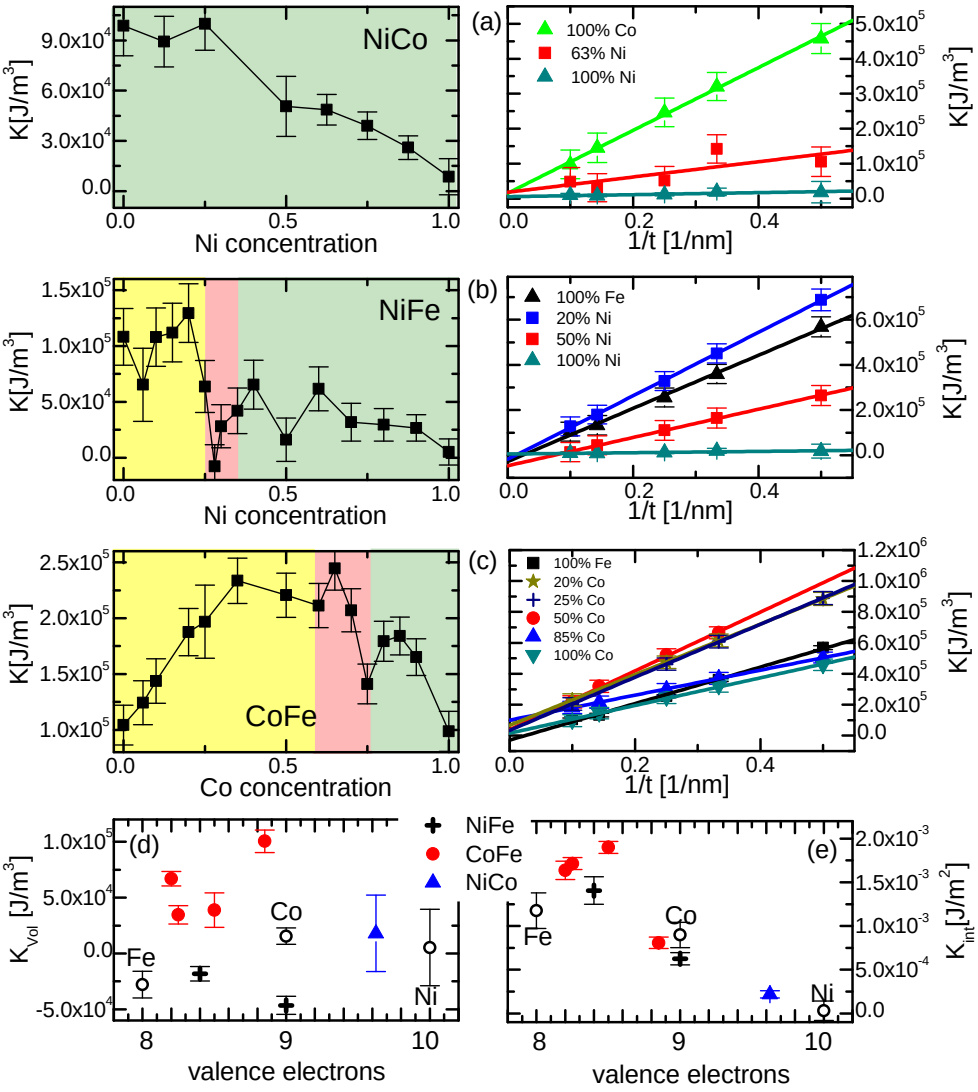

Figure 4.5: The volume averaged perpendicular anisotropy energy density K is plotted vs. alloy composition for (a) NiCo, (b) NiFe and (c) CoFe. Its thickness dependence for select alloys is plotted in the adjoining panels to the right. Again the crystal structure is signified in color code. The perpendicular anisotropy shows a local minima where fcc and bcc phases coexist for both NiFe and CoFe. In (d) and (e) we respectively plot the volume averaged bulk anisotropy energy density K_{vol} and the total interfacial anisotropy for both FM/Cu interfaces K_{int}, extracted from the intercept and slope via linear regression of K vs. reciprocal thickness 1/t.

largely broken at the interface with the mostly s-like Cu bands, while the alloy s-p band symmetry should be less affected [135, 136]. Thus only the uncompensated localized d-bands should effectively contribute to the perpendicular anisotropy. While the picture for the itinerant nature of magnetism in the 3d metals remains incomplete, there is substantial evidence that the magnetization in Ni is not solely found in localized d-bands, as one might presume on the basis of *ab initio* calculations. Tunneling spectroscopy measurements of spin-polarization of the s-p-like conduction electrons for Ni have found values around 23 % to 46 % (compare Ref. [68] and references therein), which is close to the x intercept value of the linear fit in Fig. 4.6. It is understood that the s-p bands are strongly hybridized with the d-band near the Fermi surface, giving rise to a high degree of spin polarization for the conduction bands in Ni near the Fermi surface, as revealed by angle resolved photoemission spectroscopy (ARPES) [137]. On the other hand, it is believed that the d-bands in Fe are more localized [69, 138, 139]. These considerations justify the value of the x intercept of the linear fit to the data, which is close to M_s of Ni. Furthermore, we can estimate the perpendicular interfacial anisotropy energy per d-band to be $(2 \pm 0.6) \cdot 10^{-4}\mathrm{eV}/\mu_B$. Note that the measured interface anisotropies are specifically for the Cu/alloy/Cu interfaces prepared for this study. It is very likely that these anisotropies will also vary with both the choice of non-magnetic metal and the deposition conditions. It is also important to emphasize that the crystalline texture will affect the interfacial anisotropy [140]. In the present case, all of the fcc materials possess a (111) texture, whereas the bcc materials have a (110) texture. But the general trend may indicate a starting point in the search for alloy systems with the desired interface anisotropies.

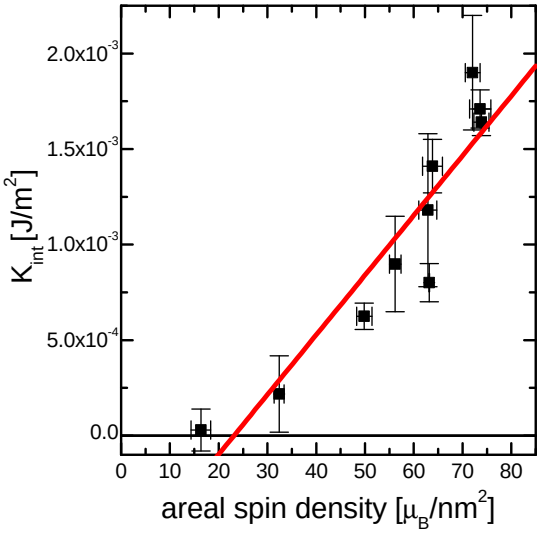

Figure 4.6: The interfacial anisotropy K_{int} is plotted against the the areal spin density. The red line is a linear fit to the data.

4.3.3 g-factor and orbital magnetization

We now turn to the measured spectroscopic g-factor that describes the relationship between the spin angular momentum and total magnetic moment per electron. For pure Fe and Ni, the g-factors are found to be $g_{\mathrm{Fe}} = 2.085 \pm 0.003$ and Ni $g_{\mathrm{Ni}} = 2.182 \pm 0.016$, respectively. For comparison, previously reported value for bulk Fe and Ni were found to be $g_{\mathrm{Fe}} = 2.08$ and $g_{\mathrm{Ni}} = 2.1853$, [82,102] in good agreement with our results for 10 nm thick films. The agreement between bulk and thin film values is not necessarily expected since there can be a substantial contribution of the orbital moment at the interface [134]. Similarly, the g-factor of Co is found to be $g_{\mathrm{Co}} = 2.139 \pm 0.005$, which is very close to the value previously reported for thin film fcc Co $g_{\mathrm{Co}} = 2.145$ [120]. This value is considerably smaller than the one for bulk hcp Co found in literature of $g_{\mathrm{Co}} = 2.183$ [102]. This is consistent with the XRD results that show no evidence of an hcp phase for the pure Co film. Furthermore, the measured g-factor of Permalloy ($Ni_{80}Fe_{20}$) is within 0.2 % the g-factor of $g_{\mathrm{Py}} = 2.109$ previously reported by Shaw, *et al.* [134]. We found that the g-factor decreases for most alloys with decreasing layer thickness, which has already been observed [118,134] and is beyond the scope of this work. Interestingly the g-factor increases with decreasing thickness for pure Co and the $Co_{50})Fe_{50}$ alloy. The g-factor for NiCo stays approximately constant for Ni concentrations between 12 % and 66% after an initial increase from pure fcc Co. At Ni concentrations above 66 %, g approaches the value of pure Ni. For comparison, the g-factor for hcp Co is also plotted in Fig. 4.7 (a) and (c). Assuming pure hcp Co a constant g-factor of 2.17 is, within a 1 % scatter, a good approximation for the g-factor of all NiCo alloys. The NiFe alloys display a different behavior with Ni-concentration. Staring from pure Fe to $Ni_{80})Fe_{20}$, g only shows an incremental increase, followed by a strong increase in g toward the value for pure Ni. The g-factor in the CoFe alloys exhibits a strong non-monotonic behavior. g increases with Co concentration from the value for pure Fe and displays a maximum at 10 % Co, followed by a minimum at approximately 20 % Co. With higher Co concentration the alloy g-factor increases towards the value for hcp Co and only drops again for pure fcc Co. We do not observe a strong variation of g-factor around the fcc-bcc phase transition of NiFe, contrary to the previous report by Bauer and Wigen [101]. Instead, our data for NiFe follow a similar trend as that reported by Meyer and Ash [102], albeit our measurements are of greater precision.

The orbital contribution to the magnetization can be calculated from the measured g-factor. Because an unquenched portion of the orbital moment also contributes to the net magnetization moment, the g-factor can differ significantly from its undressed value of 2. The ratio of orbital and spin electron moments,

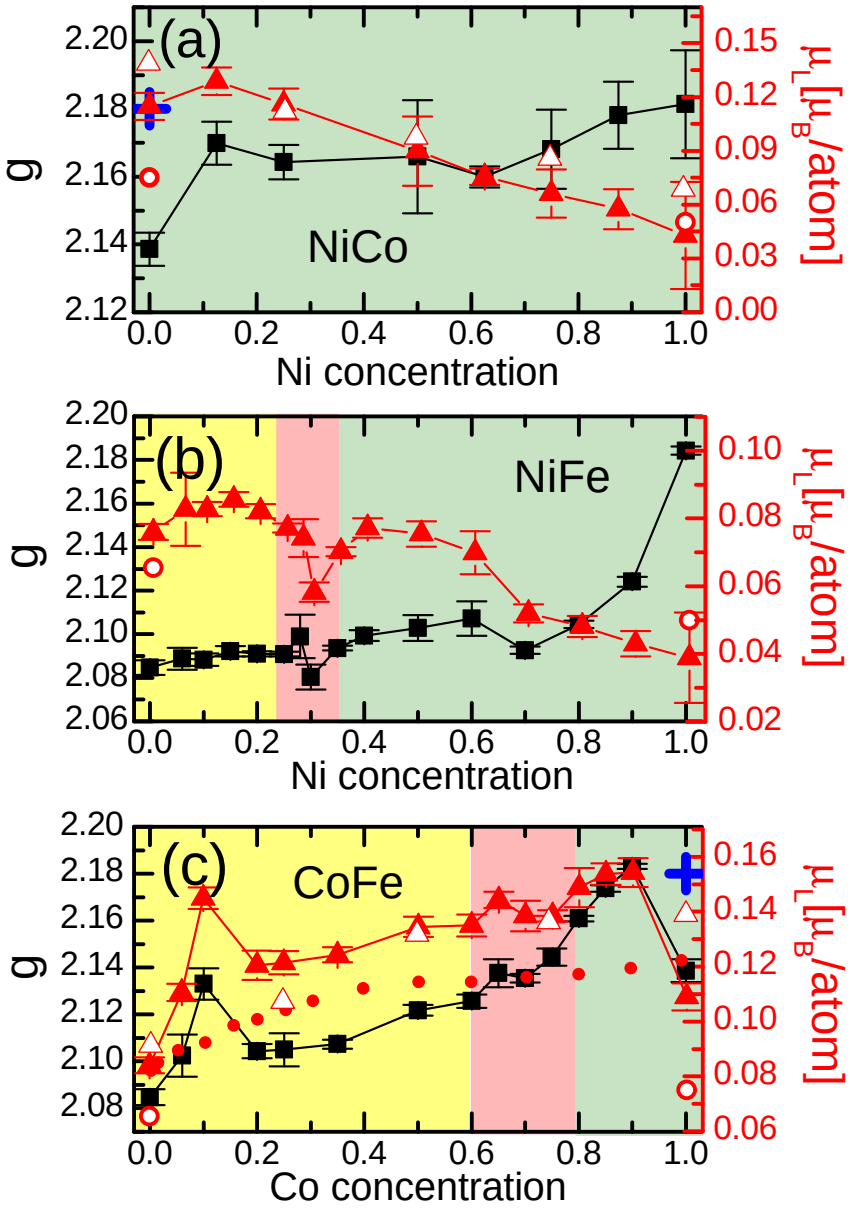

Figure 4.7: The measured out-of-plane spectroscopic g-factor (black squares, left axis) and the orbital contribution to the saturation magnetization μ_L (red triangles, right axis) are plotted for (a) NiCo, (b) NiFe and (c) CoFe against the respective alloy composition (crystal phases are again signified in color). In (a) and (c) the g-factor for pure hcp Co is added [42, 102] (blue cross). Orbital moments for the pure elements calculated by Ceresoli, *et al.* [141] are plotted as red open circles for comparison. Also orbital moments for the NiCo and CoFe systems calculated by Söderlind, *et al.* [142] (red open triangles) as well as the orbital moment calculated for CoFe by Chadov, *et al.* [143] (red dots) are included in the respective panels.

μ_L and μ_S, to the total magnetic electron moment μ is given by [144]

$$\frac{\mu_L}{\mu_S} = \frac{g-2}{2} \tag{4.1}$$

We use SQUID magnetometry to determine the total magnetic moment per atom for each alloy, where we make use of previously published data for alloy atom density [42]. We then calculate the spin and orbital moment per atom by use of Eq. (4.1). The atomic orbital moment in Bohr magnetons μ_B per atom is plotted in Fig. 4.7 (right axis, red triangles). Our values agree well with the previous report for the NiCo alloys of Reck and Fry [103]. For NiFe, their reported μ_L is slightly larger than our measured value. It was not possible to discern if the non-monotonic feature exhibited by the CoFe alloys were also observed by Reck and Fry due to an inadequate density of data in the original report. Our measurements are consistent with the well-known fact that μ_L is generally small and on the order of a few percent of the total atomic moment in crystals with cubic symmetry. Beyond that qualitative comparison, the precision of our data enable us to test theoretical ab initio models for orbital moment. Theoretical values for μ_L for pure Ni, Fe and Co reported by Ceresoli, *et al.* [141], are included in Fig. 4.7 as red open circles. For pure bcc Fe and hcp Co, the calculations underestimates the orbital moment by approximately 30 %, while for fcc Ni the theory overestimates μ_L. The results of Söderlind, *et al.* [142] for the NiCo and CoFe alloys are included as red open triangles, and the theoretical predictions of Chadov, *et al.* [143] for the CoFe system are included as red dots. The predictions of Söderlind, *et al.* for the NiCo and CoFe alloys are remarkably close to our measured values, with the possible exception of pure Co, where we measured $\mu_L = 0.11\mu_B$, and they predicted 0.14 μ_B. The calculated results of Chadov, *et al.* [143], match our measured values for pure Co and Fe quite well, but they are significantly lower than the measured values for all the alloys. The model also fails to capture the substantial jump in the orbital moment with the addition of Co at low concentrations (< 10 %), and the similarly precipitous drop as the alloy approaches pure Co.

4.4 Dynamic magnetic properties

In the previous section alloy properties correlated to the magnetization were discussed. Now we turn to properties related to the linewidth in the FMR experiment. The measured linewidth vs. frequency data is fitted to Eq. (2.4), as described in Sec. 2.1.1, select examples for which are shown in Fig. 4.2 (d). As already stated, the extracted total damping consists of multiple contributions, which are identified and quantified in this section, in order to extract the intrinsic damping.

4.4.1 Inhomogeneous linewidth broadening

The first contribution to the linewidth we discuss is the inhomogeneous linewidth broadening ΔH_0, which is presumably indicative of sample homogeneity [59,145]. We plot ΔH_0 for all the alloy systems against the respective concentrations in Fig. 4.8. For all alloys, ΔH_0 is in the range of a few mT to 10 mT.There are only a limited number of reports for ΔH_0 in the literature to compare with.

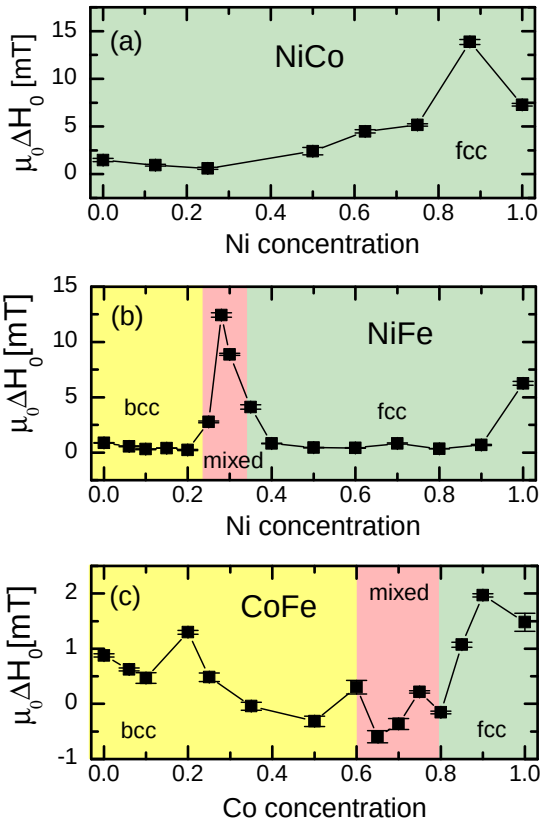

Figure 4.8: The inhomogeneous linewidth-broadening ΔH_0 is plotted vs. alloy composition for (a) NiCo, (b) NiFe and (c) CoFe. The alloy phases are denoted by color code.

For Permalloy we measure $\Delta H_0 = 0.35$ mT, which is close to other reported values [54]. For the other NiFe alloys, ΔH_0 exhibits a significant peak near the fcc-to-bcc phase transition at 30 % Ni, (see Fig. 4.8 (b)) which is easily seen in the raw data in Fig. 4.2. We speculate that this increase of inhomogeneous broadening in the NiFe is caused by the coexistence of the bcc and fcc phases at the phase transition. However, the CoFe alloys do not exhibit an increase in ΔH_0 at the equivalent phase transition at 70 % Co. This suggests that the bcc and fcc phases of NiFe tend to segregate near the phase transition, whereas the same phases for CoFe remain intermixed throughout the transition. One possible explanation for inhomogeneous broadening is magnetic anisotropy, as originally proposed in Ref. [55]. However, this explanation does not account for our measured dependence of ΔH_0 on alloy concentration, since the perpendicular magnetic anisotropy, determined in Sec. 4.3.2, essentially exhibits opposite behavior with alloy concentration. For our alloys ΔH_0 seems to roughly correlate to the inverse exchange constant [146, 147], which could be a starting point for future investigation of a quantitative theory of the inhomogeneous broadening.

4.4.2 Binary alloy damping

We plot the total measured damping α_{tot} vs. composition for NiCo, NiFe and in Fig. 4.9 (red crosses). The total damping of the NiCo system increases continuously with Ni concentration. Such continuous behavior in the damping is expected owing to the absence of a phase transition with for this alloy. In the NiFe system, α_{tot} is essentially unchanged by Ni-concentration up to the bcc to fcc phase transition at approximately 25 % Ni. Upon reaching the phase transition, α_{tot} increases sharply by approximately 30 %. On the Ni-rich side of the phase transition, α_{tot} increases monotonically with increasing Ni concentration all the way to pure Ni. The CoFe system shows a different behavior in the damping and displays a sharp minimum of $(2.3 \pm 0.1) \cdot 10^{-3}$ at 25 % Co as previously reported [74]. Then α_{tot} increases with Co concentration to a plateau value stretching from the phase transition ($\approx$ 70 % Co) to pure Co. Comparison of our data to previous reports is imprecise, owing to the variation in measurement conditions and sample characteristics for all the reported measurements. First of all, the damping strongly depends on the temperature [27, 148]. In addition, the multiple intrinsic and intrinsic contributions to the total damping are not always accounted for in the literature. As an example, reports for the intrinsic damping in Py ($Ni_{80}Fe_{20}$) vary from $\alpha = 0.0055$ to $\alpha = 0.04$ at room temperature. The large variation for these reported data is possibly the result of different uncontrolled contributions to the extrinsic damping that add to the total damping in the different experiments, e.g. spin-pumping [149–151], or roughness [150]. Therefore, the value for the intrinsic damping of Py is expected to be at the low end of this scatter. Our measured value of $\alpha = 0.0072$ lies within the range of reported values. Similarly, we find many of our measured damping values for different alloy compositions lie within the range of reported values [52, 60, 120, 152–154]. Our measured damping of the pure elements and the $Ni_{80}Fe_{20}$ and $Co_{90}Fe_{10}$ alloys is compared to room temperature values found in literature in Table 4.1, Columns 2 and 3. Column 5 contains theoretically calculated values.

This scatter in the experimental data reported in the literature and its divergence from calculated values of the damping shows the necessity to determine the intrinsic damping α_{int} by quantification of all extrinsic contributions to the measured total damping α_{tot}.

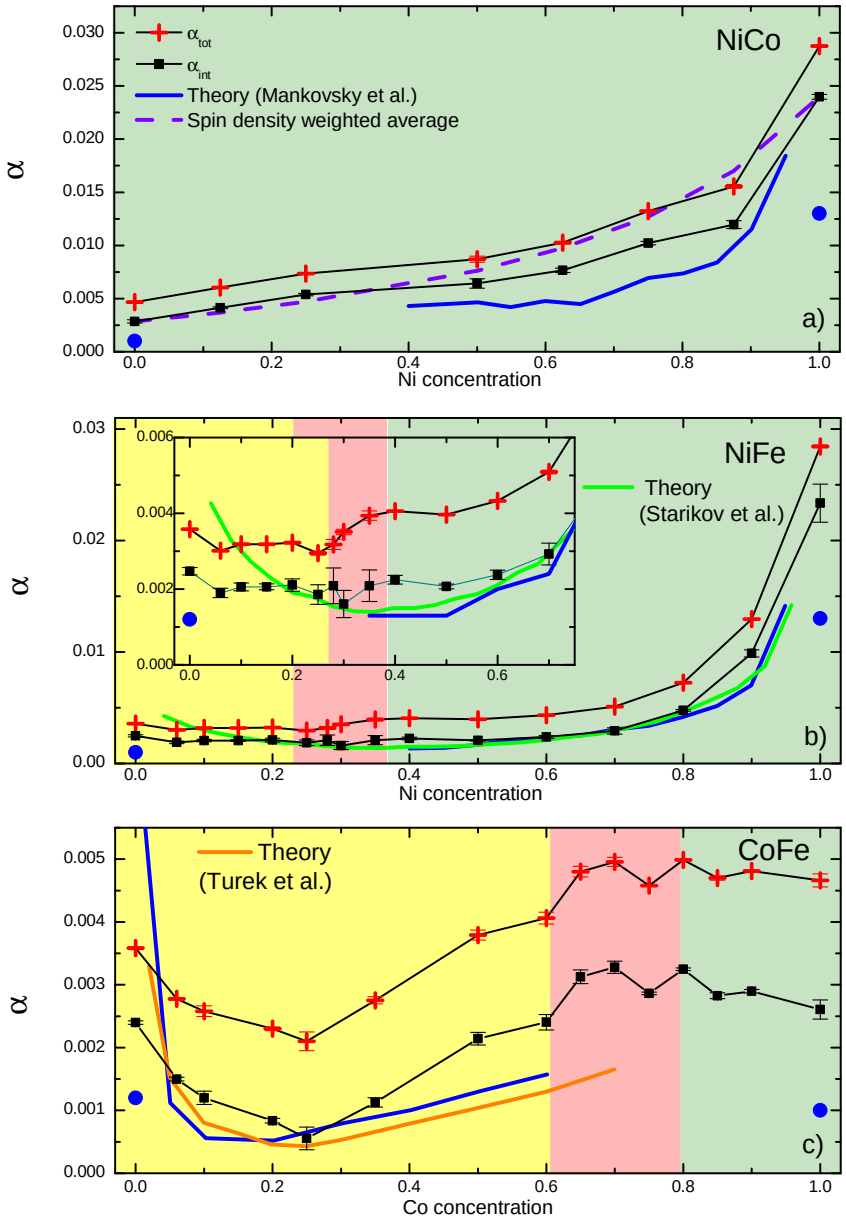

Figure 4.9: The measured damping α_{tot} of all the alloys is plotted against the alloy composition (red crosses) for (a) NiCo, (b) NiFe and (c) CoFe. The black squares are the intrinsic damping α_{int} after correction for spin pumping and radiative contributions to the measured damping. The blue line is the intrinsic damping calculated from the Ebert-Mankovsky theory, [43] where the blue circles are the values for the pure elements at 300K. The green line is the calculated damping for the NiFe alloys by Starikov, *et al.* [63] The inset in (b) depicts the damping in a smaller concentration window in order to better depict the small features in the damping around the phase transition. The damping for the CoFe alloys, calculated by Turek *et al.* [64] is plotted as the orange line in (c). For the NiCo alloys in (a) the damping calculated by the spin density of the respective alloy weighted bulk damping [132] (purple dashed line).

Material	α_{tot}	Literature values	α_{int}	Calculated values
Ni	0.029 (fcc)	0.064 [152] 0.045 [155]	0.024 (fcc)	0.017 [27] (fcc) 0K 0.022 [156] (fcc) 0K 0.013 [43] (fcc)
Fe	0.0036 (bcc)	0.0019 [152] 0.0027 [153]	0.0025 (bcc)	0.0013 [27] (bcc) 0K 0.0010 [156] (bcc) 0K 0.0012 [43] (bcc) 0K
Co	0.0047 (fcc)	0.011 [152]	0.0029 (fcc)	0.0011 [27] (hcp) 0K 0.00073 [156] (hcp) 0K 0.001 [43] (hcp)
$Ni_{80}Fe_{20}$	0.0073 (fcc)	0.008 [152] 0.008-0.04 [157] 0.0078 [154] 0.007 [158] 0.006 [87, 159] 0.0055 [160]	0.0050 (fcc)	0.0046 [63, 72] (fcc) 0K 0.0039- 0.0049 [64] (fcc) 0K
$Co_{90}Fe_{10}$	0.0048 (fcc)	0.0043 [152] 0.0048 [132]	0.0030 (fcc)	

Table 4.1: The total measured damping α_{tot} (Col. 2) and the intrinsic damping (Col. 4) for Py, $Co_{90}Fe_{10}$, and the pure elements are compared to both experimental (Col. 3) and theoretical (Col. 5) values from the literature. All values are room temperature values of the damping if not noted otherwise.

4.4.2.1 Radiative damping and spin pumping contributions

The first extrinsic contributions to the damping that we consider is the radiative damping α_{rad}, which is discussed in Sec. 3.2.1. The calculated α_{rad} for all alloys is plotted in Fig. 4.11. Though inherently small for most thin films, α_{rad} can become significant for alloys with exceptionally small intrinsic damping and/or high saturation magnetization. For example, it plays a significant role (values of $\alpha_{\mathrm{rad}} \approx 5 \cdot 10^{-4}$) for the whole composition range of the CoFe alloy system and the Fe-rich side of the NiFe system. On the other hand, for pure Ni and Py α_{rad} comprises only 3 % and 5 % of α_{tot}, respectively. The values for the radiative damping can also be confirmed by a spacer measurement, as described in Sec. 3.2.1.5. We therefore measure the damping of a 10 nm $Co_{25}Fe_{75}$ and a $Co_{20}Fe_{80}$ sample with a 100 µm spacer inserted between sample and waveguide. The spacer lowers the inductive coupling between sample and waveguide and therefore almost completely suppresses the radiative damping contribution. Thus, $\alpha_{\mathrm{rad}} = \alpha_{\mathrm{tot}}(d = 0) - \alpha_{\mathrm{tot}}(d = 100\,\mu\mathrm{m})$, where d is the distance between sample and waveguide. The experimentally determined α_{rad} are plotted in Fig. 4.11 (c) and match within errors the calculated values.

The second non-negligible contribution to the damping that we consider is the

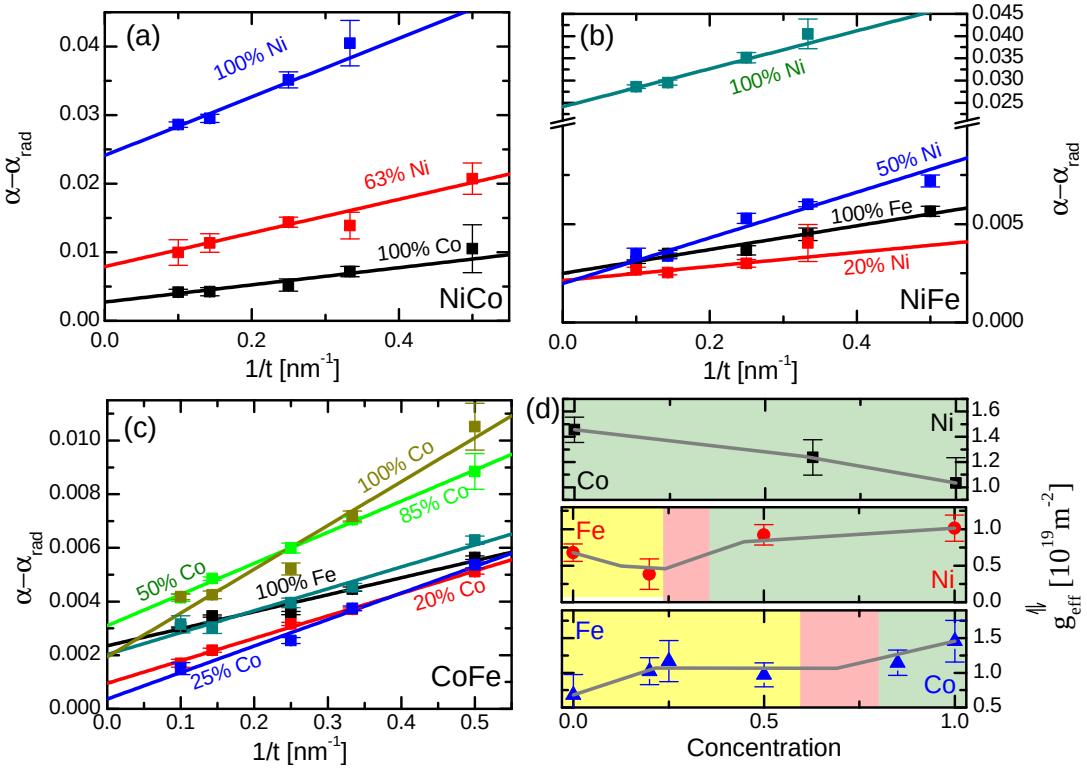

Figure 4.10: The damping for the thickness series at select alloy compositions vs. $1/t$ for (a) NiCo, (b) NiFe and (c) CoFe (data points, concentrations denoted in the plots), with linear fits to Eq. (3.56) (solid lines). (d) The extracted effective spin mixing conductance $g_{\text{eff}}^{\uparrow\downarrow}$ for the measured alloy systems, where the gray lines show the linear interpolations for intermediate alloy concentrations.

interfacial contribution to the measured damping, such as spin-pumping into the adjacent Ta/Cu bilayers. Spin pumping is proportional to the reciprocal sample thickness, as elaborated on in Sec. 3.2.3. In Fig. 4.10 (a)-(c) we plot the damping dependence on reciprocal thickness $1/t$ for select alloy concentrations, and extract the effective spin mixing conductance $g_{\text{eff}}^{\uparrow\downarrow}$ by fitting Eq. (3.56) to the data. The effective spin mixing conductance contains details of the spin transport in the adjacent non-magnetic layers, such as the interfacial spin mixing conductance, both the conductivity and spin diffusion for all the non-magnetic layers with a non-negligible spin accumulation, as well as the details of the spatial profile for the net spin accumulation [90,161]. Regardless, the values for $g_{\text{eff}}^{\uparrow\downarrow}$, plotted versus the alloy concentration in Fig. 4.10 (d), are in the range of previously reported values for samples prepared under similar growth conditions [90,91,132,161,162]. Intermediate values of $g_{\text{eff}}^{\uparrow\downarrow}$ are determined by a guide to the eye interpolation [grey lines, Fig. 4.10 (d)] and α_{sp} is calculated for all alloy concentrations utilizing those

interpolated values, as plotted in Fig. 4.11 The data for $g_{\mathrm{eff}}^{\uparrow\downarrow}$ in the NiFe alloys shows approximately a factor two increase of $g_{\mathrm{eff}}^{\uparrow\downarrow}$ between Ni concentrations of 30 % Ni and 50 % Ni, which we speculate to occur at the fcc to bcc phase transition around 30 % Ni. According to this line of speculation, the previously mentioned step increase in the measured damping at the NiFe phase transition can be fully attributed to the increase in spin pumping at the phase transition. In CoFe, the presence of a step in $g_{\mathrm{eff}}^{\uparrow\downarrow}$ at the phase transition is not confirmed, given the measurement precision, although we do observe an increase in the effective spin mixing conductance when transitioning from the bcc to fcc phase. The concentrational dependence of $g_{\mathrm{eff}}^{\uparrow\downarrow}$ requires further thorough investigation and we therefore restrict ourselves to reporting the experimental findings.

4.4.2.2 Intrinsic damping

Eddy-current damping [44, 85] is estimated by use of Eq. (3.53) for films 10 nm thick or less. Eddy currents are neglected because they are found to be less than 5 % of the total damping. Two-magnon scattering is disregarded because the mechanism is disallowed in the out-of-plane geometry [163–165]. The total measured damping is therefore well approximated as the sum

$$\alpha_{\mathrm{tot}} = \alpha_{\mathrm{int}} + \alpha_{\mathrm{rad}} + \alpha_{\mathrm{sp}}. \tag{4.2}$$

We determine the intrinsic damping of the material by subtracting α_{sp} and α_{rad} from the measured total damping, as shown in Fig. 4.9. The intrinsic damping increases monotonically with Ni concentration for the CoNi alloys. Indicative of the importance of extrinsic sources of damping, α_{int} is approximately 40 % smaller than α_{tot} for the Co-rich alloy, though the difference decreases to only 15 % for pure Ni. This behavior is expected, given that α_{rad} and α_{sp} are proportional, or inversely proportional to M_{s}, respectively. A comparison of α_{int} to the calculations by Mankovsky, *et al.* [43] shows excellent quantitative agreement to within 30 %. Furthermore, we compare α_{int} of the NiCo alloys to the spin density weighted average of the intrinsic damping of Ni and Co [purple dashed line in Fig. 4.9 (a)], which gives good agreement with our data, as observed by Shaw *et al.* [132]. α_{int} for NiFe [Fig. 4.9 (b)] also increases with Ni concentration after a small initial decrease from pure Fe to the first NiFe alloys. The step increase found in α_{tot} at the bcc to fcc phase transition is fully attributed to α_{sp}, as detailed in the previous section, and therefore does not occur in α_{int}. Similar to the NiCo system α_{int} is significantly lower than α_{tot} for Fe-rich alloys. The comparison to the calculations by Mankovsky, *et al.* [43] (blue line) and Starikov, *et al.* [63] (green line) yields within errors almost perfect agreement in the fcc phase, with marginally larger deviations in the Ni rich regime. Starikov, *et al.* [63] calculated the damping over the full range of compositions, under the assumption of continuous fcc phase. This calculation deviates further from our measured α_{int} in the

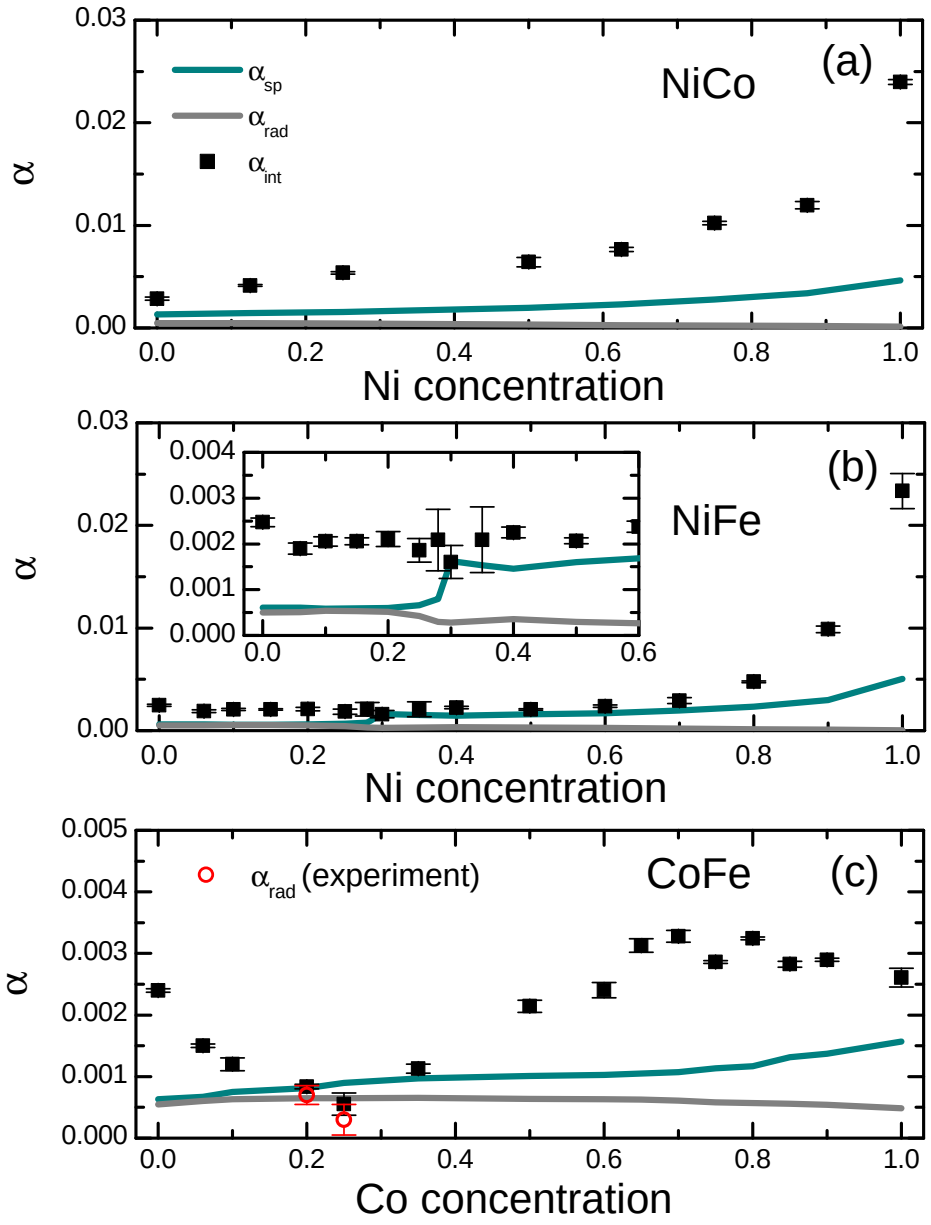

Figure 4.11: Spin pumping α_{sp} (dark green lines), radiative damping contribution α_{rad} (grey lines) and the extracted intrinsic damping α_{int} (black squares) are plotted against alloy concentration for 10 nm samples of NiCo in (a), NiFe in (b), and CoFe in (c). α_{rad} for the $Co_{25}Fe_{75}$ and $Co_{20}Fe_{80}$, determined by a spacer measurement, is plotted in (c) as red circles. The comparison of both extrinsic contributions to α_{int} shows the necessity to account for extrinsic contributions to the damping, in particular in the case of large M_{s} and low intrinsic damping.

bcc phase exhibiting qualitatively different behavior. The dependence of α_{int} on alloy composition in the CoFe alloys exhibits strongly non-monotonic behavior, differing from the two previously discussed alloys. α_{int} displays a minimum at 25 % Co concentration with a, for conducting ferromagnets unprecedented, low value of $\alpha_{\text{int}} = (5 \pm 1.8) \cdot 10^{-4}$. With increasing Co concentration, α_{int} grows up to the phase transition, at which point it decreases by 10-20 % until it reaches the value for pure Co. The special properties of the CoFe alloy system are elaborated on in greater detail in Sec. 5.

Comparing α_{int} to the calculations by Mankovsky *et al.* [43], we find good quantitative agreement with the value of the minimum. However, the concentration of the minimum is calculated to occur at approximately 10-20 % Co, a slightly lower value than 25 % Co that we find in this study. Furthermore, the strong concentration dependence around the minimum is not reflected in the calculations. More recent calculations by Turek *et al.* [64], for the bcc CoFe alloys [orange line in Fig. 4.9 (c)] find the a minimum of the damping of $4 \cdot 10^{-4}$ at 25 % Co concentration in good agreement with our experiment, but there is some deviation in concentration dependence of the damping around the minimum. Turek *et al.* [64] also reported on the damping in the NiFe alloy system, with similar qualitative and quantitative results as the other two presented quantitative theories [43, 63] and the results are therefore not plotted in Fig. 4.9 (b) for the sake of comprehensibility of the figure. For both NiFe and the CoFe alloys the calculated spin density weighted intrinsic damping of the pure elements (not plotted) deviates significantly from the determined intrinsic damping of the alloys, in contrary to the good agreement achieved for the CoNi alloys. We speculate that this difference between the alloy systems is caused by the non-monotonous dependence of the density of states at the Fermi Energy in the CoFe and NiFe systems.

Other calculated damping values for the pure elements and the $Ni_{80}Fe_{20}$ and $Co_{90}Fe_{10}$ alloys are compared to the determined intrinsic damping in Tab. 4.1. Generally, the calculations underestimate the damping significantly, but our data are in good agreement with more recent calculations for Py. None of the theories considered here include thermal fluctuations. Regardless, we find exceptional agreement with the calculations to α_{int} at intermediate alloy concentrations. We speculate that the modeling of disorder in the alloys in the calculations, by the coherent potential approximation (CPA) could be responsible for this exceptional agreement. The effect of disorder on the electronic band structure possibly dominates any effects due to nonzero temperature. Indeed, both effects cause a broadening of the bands due to enhanced momentum scattering rates. This directly correlates to a change of the damping parameter according to the theory of Gilmore and Stiles [27]. Therefore, the inclusion of the inherent disorder of solid-solution alloys in the calculations by Mankovsky, *et al.* [43] mimics the effects of temperature on damping to some extent. This argument is corroborated by the fact that the calculations by Mankovsky, *et al.* [43] diverge for diluted alloys

and pure elements (as shown in Fig. 4.9 (c) for pure Fe), where no or to little disorder is introduced to account for temperature effects. Mankovsky, *et al.* [43] performed temperature dependent calculations of the damping for pure bcc Fe, fcc Ni and hcp Co and the values for 300 K are shown in Tab. 4.1 and Fig. 4.9 (c). These calculations for α_{int} at a temperature of 300 K are approximately a factor of two less than our measured values, but the agreement is significantly better than obtained with calculations that neglect fluctuations.

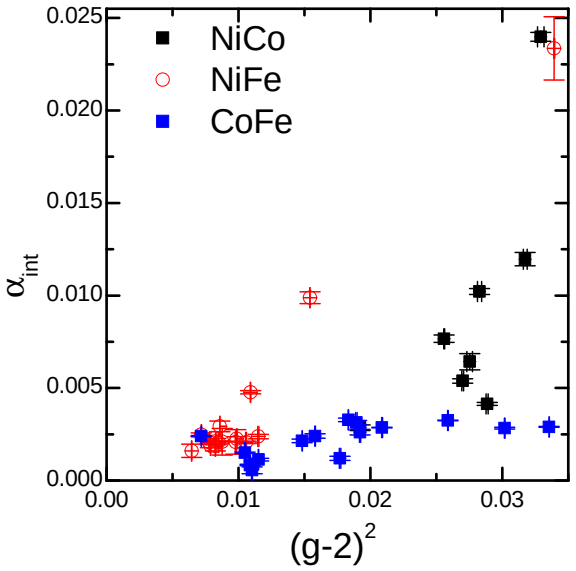

Figure 4.12: The intrinsic damping α_{int} is plotted against $(g-2)^2$ for all alloys. We do not observe a proportionality between α_{int} and $(g-2)^2$.

It has been reported [120,166] that there is a proportionality between α_{int} and $(g-2)^2$, as originally predicted by Kambersky in his microscopic BFS model [66]. We present in Fig. 4.12 a plot of α_{int} vs. $(g-2)^2$ (determined in Sec.4.3.3) for all samples measured here. While some samples with large values for $(g-2)^2$ also exhibit large α_{int}, this is not a general trend for all the measured samples. Given that the damping is not purely a function of the spin-orbit strength, but also depends on the details of the band structure, the result in Fig. 4.12 is to be expected. In other words, if there is significant band overlap, then there should be significant interband transition leading to the related damping channel. Furthermore, the density of states at the Fermi energy will affect the intraband contribution to the damping [27, 70]. Finally, the ratio of inter- to intra-band scattering that mediates damping contributions at a fixed temperature (RT for our measurements) changes for different elements [27,70] and therefore with alloy concentration. None of these factors are necessarily proportional to the spin-orbit coupling. Therefore, we conclude that this simple relation, which originally traces to an order of magnitude estimate for the case of spin relaxation in semiconductors [167], does not hold for all magnetic systems in general.

5

Damping of Co_xFe_{1-x} alloys

The results presented in this section have been published in Ref. [74].

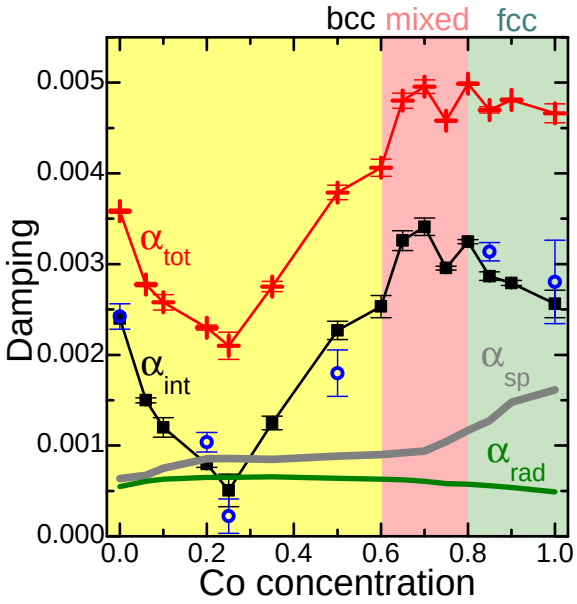

Figure 5.1: Total measured damping with radiative and interfacial contributions. Total damping α_{tot} (red circles with lines), spin-pumping α_{sp} (grey line) and radiative α_{rad} (green line) contributions to the damping, the calculated intrinsic damping α_{int} (black squares with lines), as well as the extrapolated bulk value of the damping (blue open circles) are plotted as a function of Co-concentration. The crystal structure of the alloys, obtained from XRD, is signified by the color regions in the plot.

Taking a closer look at the determined intrinsic damping of the $Co_{25}Fe_{75}$ alloy underlines the importance of accounting for the contributions of α_{sp} and α_{rad}, as they are of similar magnitude as α_{int}, which is shown in Fig. 5.1. For the samples for which there is full thickness-dependent data, the intrinsic damping can also be determined from the y-intercepts found in the data of Fig. 4.5. We also include these intercepts in Fig. 5.1 (blue circles), which show that both approaches to remove the effects of spin pumping are consistent. For 25% Co, α_{int} now exhibits a sharp minimum in damping of $(5 \pm 1.8) \cdot 10^{-4}$, which is astonishing for a conductor. Indeed, values of $\alpha_{\mathrm{int}} \leq 0.001$ have been measured only in ferrimagnetic insulators [168]. These results raise the question why α_{int} can be so low in the presence of conduction electrons. To gain a deeper understanding, we performed electronic structure calcu-

lations for Co_xFe_{1-x} within a full-relativistic, multiple-scattering approach (Korringa-Kohn-Rostoker method [169], KKR) using the coherent potential approximation (CPA) [170, 171] over the entire range of compositions. Several representative examples are given in Fig. 5.2 (a). The d-states (peak in the DOS below E_F) for pure Fe are not fully occupied. Consistent with the rigid band model [172], the d-states shift to lower energies when the concentration of Co increases, and become fully occupied at 25% Co, coinciding with the minimum in $n(E_F)$ shown in Fig. 5.2 (a), which originates from the hybridization between majority Fe e_g and minority Co t_{2g} states.

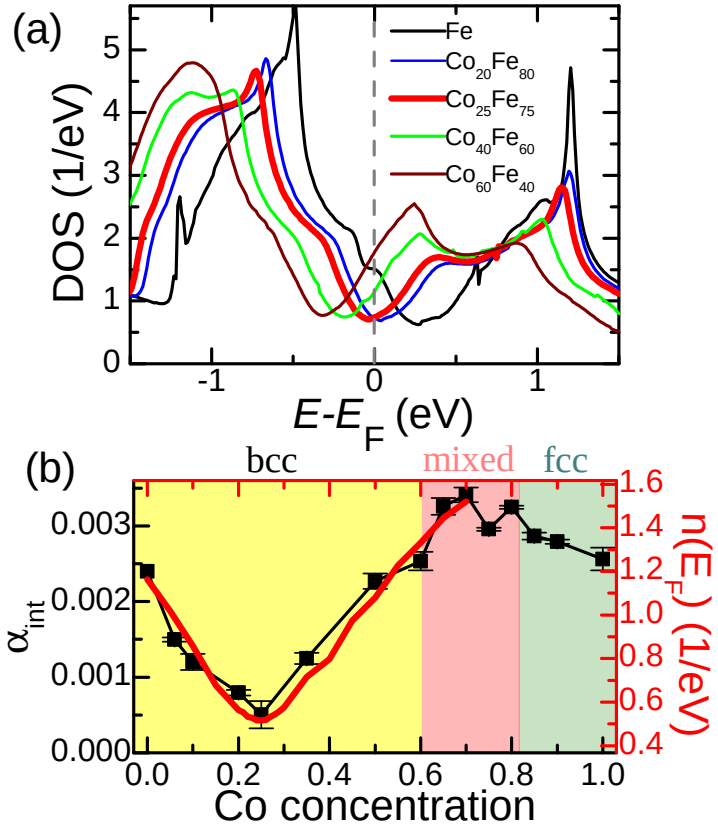

Figure 5.2: Calculated electron density of states (DOS) and its comparison to the intrinsic damping. (a) Electronic structure of bulk Co_xFe_{1-x}. The DOS is shown for several Co-concentrations, as indicated. Note that all alloy compositions are aligned to a common Fermi energy, E_F, at zero energy to facilitate comparison. b, The intrinsic damping (black squares, left axis) is compared to the calculated DOS at the Fermi energy $n(E_F)$ (red line, right axis). The y-offset of $n(E_F)$ is chosen deliberately to demonstrate that the concentration-dependent features of the damping directly correlate to features of $n(E_F)$. Concentration-independent contributions to the damping cannot be excluded, which are accounted for by the $0.4\,eV^{-1}$ y-offset.

Ebert *et al.* [173] and Lounis *et al.* [174] suggested that α_{int} is proportional to $n(E_{\text{F}})$ in the breathing Fermi-surface model (that is, intraband transitions) in the cases of a minimally varying spin-orbit coupling (SOC) (as is the case for the $\text{Co}_x\text{Fe}_{1-x}$ system) and small electron-phonon coupling [27, 66]. Alternatively, interband transitions become significant only if bands have a finite overlap due to band broadening, caused for example by coupling to the phonons. As a result, interband transitions are suppressed at low temperature and energy dissipation becomes dominated by intraband transitions. Our RT measurements of $\text{Co}_x\text{Fe}_{1-x}$ system satisfy this 'low-temperature' condition because the electron-phonon coupling is $<$20 meV for pure bcc Fe, and $<$30 meV for pure hcp Co. Band broadening due to disorder is about 15 meV for the e_g states that dominate at E_{F} (50 meV for the t_{2g} states) in $\text{Co}_{25}\text{Fe}_{75}$ and varies up to 55 meV for the e_g states (150 meV for the t_{2g} states) over the whole range of composition. These calculations show that the band-broadening effect at RT is too small to provide significant interband damping, consistent with the almost perfect proportionality between $n(E_{\text{F}})$ and α_{int} for all alloy compositions in the bcc phase (0 % to 60 % Co). Such a proportionality requires an offset of $0.4\,\text{eV}^{-1}$, which originates from the fact the $n(E_{\text{F}})$ is a superposition of all states, some of which do not contribute significantly to the damping. We therefore demonstrate and conclude that α_{int} is largely determined by $n(E_{\text{F}})$ in the limit of an intraband scattering dominated intrinsic damping mechanism. Furthermore, the FeCo system studied here is unique from an electronic structure point of view, in the sense that the two elements have similar spin-orbit coupling and our calculations show that any enhanced broadening of electron states at the Fermi level due to alloying is small. The only remaining significant contributing factor to the damping is $n(E_{\text{F}})$. Because all the other factors are relatively insensitive to the alloy composition and structure, the deep minimum in $n(E_{\text{F}})$ for $\text{Co}_{25}\text{Fe}_{75}$ leads to the low intrinsic damping that we measure.

6

Approaching the intrinsic damping of $Co_{25}Fe_{75}$

In the previous sections the intrinsic damping of the investigated materials was deduced from the value of total measured damping and the contributions of significant extrinsic damping mechanisms.

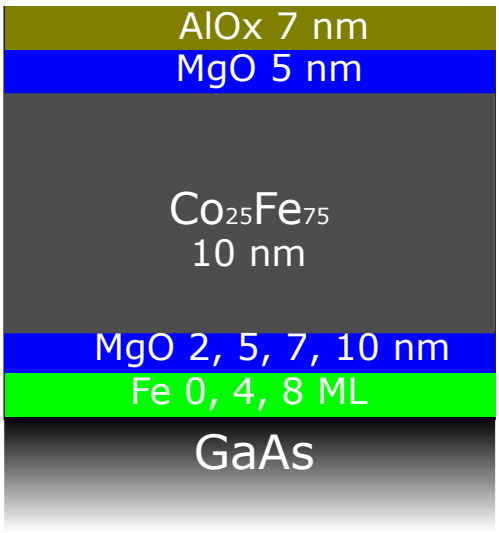

Figure 6.1: Sketch of the sample stack for epitaxial $Co_{25}Fe_{75}$ samples. A 10 nm $Co_{25}Fe_{75}$ film is deposited on a GaAs (100) substrate with Fe and MgO seed layers of variable thicknesses. A 5 nm MgO/7 nm Al_2O_3 cap is applied to all samples to prevent oxidation.

The Cu/Ta cap and seed layers of the samples investigated were used to guarantee a well controlled sample growth, but they introduced a spin pumping contribution to the damping. Similarly, the narrow 100 µm waveguide utilized in the previous measurements induced a non-negligible radiative damping. However, for application in devices the total damping of the whole system determines device properties. Therefore, in order to suppress extrinsic damping mechanisms the geometric factors, which determine their magnitude need to be optimized. As shown in Chapter 5, the $Co_{25}Fe_{75}$ alloy exhibits the lowest intrinsic damping of all investigated alloys, which in combination with its large M_s is of great interest for magnonics applications. Thus, it is desirable to find a sample and measurement geometry, where the total measured damping of $Co_{25}Fe_{75}$ approaches α_{int}. To this end, we utilize a waveguide with a 500 µm center-line in the following measurements, rendering the contribution of α_{rad} negligible. The

$Co_{25}Fe_{75}$ layer is grown on a GaAs (100) substrate with insulating MgO cap and seed layers, compare Fig. 6.1, thus eliminating any possibility of damping enhancement by spin pumping. A 7 nm AlOx capping layer is also introduced to prevent oxidation. In this geometry the measured damping approaches the intrinsic damping $\alpha_{\mathrm{tot}} \approx \alpha_{\mathrm{int}}$ and can be tuned by optimizing the sample deposition process.

6.1 Poly-crystalline $Co_{25}Fe_{75}$

Samples were prepared by molecular-beam-epitaxy (MBE). Before sample deposition the Si, Si_2O_3, GaAs, and MgO substrates were annealed at 250° C. The $Co_{25}Fe_{75}$ layers were co-deposited from Fe and Co sources on a 5 nm MgO seed layer. Samples then were characterized in an IP-FMR measurement, as described in Sec. 2.1.2. We plot the resonance field H_{res} against IP angle in Fig. 6.2. Only the sample grown on the MgO substrate exhibits a four-fold anisotropy, while samples grown on the other three substrates only exhibit a weak uniaxial anisotropy. For a crystalline sample a four-fold anisotropy is expected, therefore the IP angle dependence of H_{res} gives an indication of sample structure. We thus assume that the sample grown on MgO is to some degree crystalline and that the others are poly-crystalline.

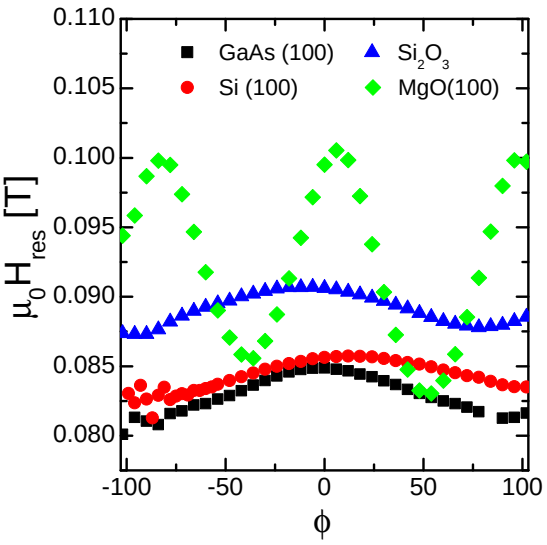

Figure 6.2: The IP angle dependence of the resonance field H_{res} is plotted for samples with different substrates.

For magnonics applications isotropic materials are advantageous, since magnetic anisotropies cause anisotropic spinwave dispersion relations, complicating any device geometries. We therefore only discuss the isotropic poly-crystalline samples in this section. All these samples display isotropic damping, however the sample grown on GaAs exhibits the lowest linewidth and damping. The RT angle dependence of the resonance field and the frequency dependent linewidth for easy and hard axis are plotted in Fig. 6.3 (a) and (b), respectively and we find a RT damping of $(1.6 \pm 0.2) \cdot 10^{-3}$. This value is significantly lower than values typically

measured in metallic ferromagnets [98] and is within a factor of three of the theoretically predicted and experimentally deduced value of $5 \cdot 10^{-4}$. Nevertheless, the question why the measured damping is larger than the theoretically predicted one remains, especially because extrinsic damping mechanisms should not be the reason for the difference. As discussed in Sec. 3 temperature has a significant influence on the damping and knowledge of the temperature dependence of the damping might give an indication for the intrinsic mechanisms responsible for the damping. We therefore measure the temperature dependence of the damping in a temperature range from 20 K to 295 K. The results are shown in Fig. 6.3 (c). The damping scatters, within errors around an average value of $(1.6 \pm 0.2) \cdot 10^{-3}$ and does not exhibit any discernible dependence on temperature.

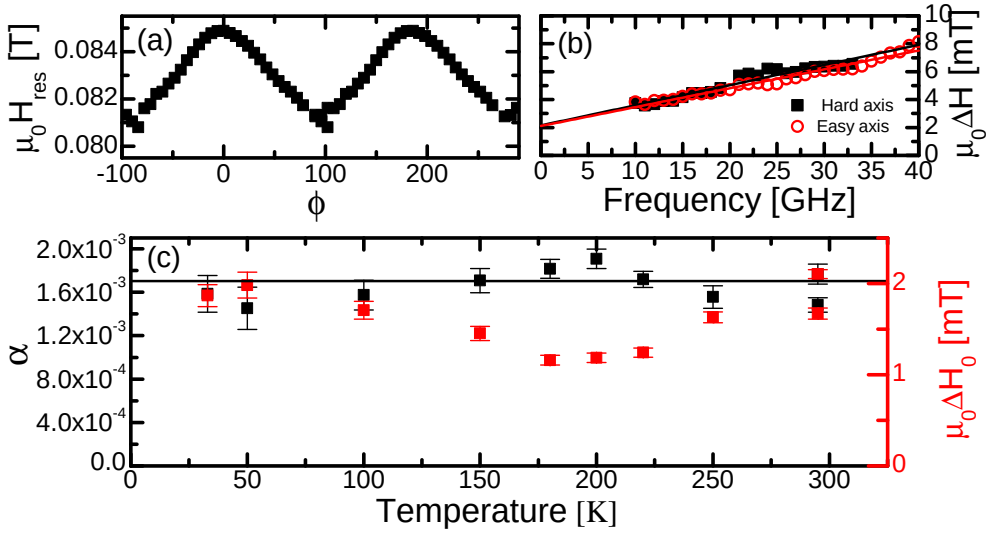

Figure 6.3: Results of an IP FMR measurement of a GaAs/MgO(5 nm)/$Co_{25}Fe_{75}$ (10 nm)/MgO(5 nm) sample. (a) shows the angular dependence of the resonance field measured at 12 GHz and (b) the linewidth vs. frequency plots for hard and easy axis. The temperature dependence of the total damping α and inhomogeneous linewidth broadening ΔH_0 are plotted in (c), where the black line represents the temperature average of the damping $\alpha_{\text{ave}} = (1.6 \pm 0.3) \cdot 10^{-3}$.

Calculations and experiments [43, 60] usually show a significant increase of the damping at temperatures below 100 K. Within the framework of the torque-correlation model (Sec. 3.1.2) this increase is caused by enhanced intra-band scattering due to a band narrowing of the thermally broadened bands. The absence or later onset of such an increase can point to increased interband mediated scattering being responsible for the damping. This, in turn indicates a strong broadening of the bands, which is in our poly-crystalline and atomically disordered $Co_{25}Fe_{75}$ samples not surprising. Band structure calculations show that

disorder, as well as crystalline defects can causes band broadening [74]. Therefore, the temperature dependent measurements give a good indication that the damping in the poly-crystalline $Co_{25}Fe_{75}$ samples is significantly influenced by interband scattering, which could also cause the deviation from the theoretically possible value of the damping.

6.2 Epitaxial $Co_{25}Fe_{75}$

For all calculations of the damping perfect crystallinity of the sample is assumed. Therefore, in order to facilitate the comparison of our measurements to theoretical values, crystalline samples were deposited. We deposited the layer stack, sketched in Fig. 6.1 on a GaAs substrate. The substrate was annealed at 250° C before additional GaAs was deposited to produce a perfectly crystalline surface. Fe seed layers of 4 and 8 mono-layers thickness were introduced on some of the samples to facilitate crystalline growth of the MgO. Crystalline growth of MgO(100) on both GaAs(100) and Fe(100) has been observed, facilitated by a relatively small lattice mismatch of 5.4 % and 3.4 %, respectively [175–178]. The MgO thickness was varied between 2 nm and 10 nm to investigate the effects of roughness on the damping. The sample growth was monitored by reflection high-energy electron diffraction (RHEED), which indicated a crystalline sample growth.

Fig. 6.4 shows the results of IP-FMR measurements of the sample series grown with 2 nm, 5 nm, 7 nm, and 10 nm MgO seed layers. The IP angle dependence of the resonance field and linewidth measured at 12 GHz [Fig. 6.4 (a) and (b)] shows a clear four-fold anisotropy and negligible uniaxial anisotropy. The four-fold anisotropy constant $K_1^{\parallel}$ shows no dependence on MgO seed layer thickness and has within error bars a value of $K_1^{\parallel} = (2.1 \pm 0.8)\,\mathrm{J/m^3}$ for all samples, which is close to $K_1^{\parallel}$ of Fe layers of similar thickness grown on MgO(100) [179]. For all samples the linewidth along the hard axis (0°) has the same low value of 3.6 mT, however the linewidth for the different samples changes significantly along the easy axis, which can be caused by a two-magnon scattering process. Two-magnon scattering is mediated by defects, such as interface roughness [50] and a difference in the easy axis linewidths is therefore not surprising for samples deposited on seed layers with presumably varying roughness. The existence of the two-magnon scattering process can be directly determined from the frequency dependent linewidth, which is exemplary plotted in Fig. 6.4 (c) for the $Co_{25}Fe_{75}$ sample grown on a 5 nm MgO seed layer. While the linewidth in the hard axis [110] direction is completely linear with frequency, the linewidth along the easy [100] axis displays a sharp non-linear drop for frequencies below 20 GHz. This drop at low frequencies is consistent with the two magnon scattering mechanism described in Ref. [50]. Following the argument in Ref. [57], the enhancement of

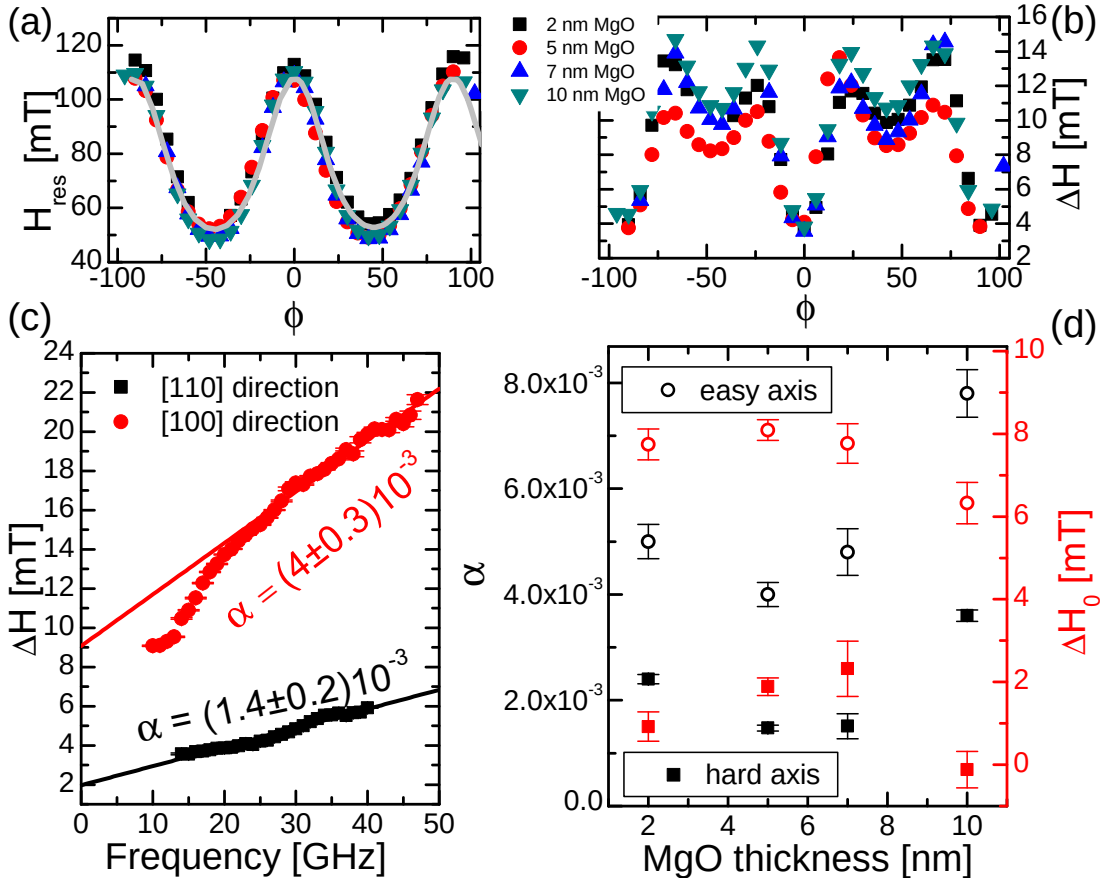

Figure 6.4: Results of IP-FMR measurements of 10 nm $Co_{25}Fe_{75}$ samples grown on a GaAs substrate with MgO buffer layers of different thicknesses. (a) and (b) depict the IP angle dependence of the resonance field and linewidth measured at 12 GHz, respectively. The frequency dependence of the linewidth along [110] (hard axis) and [100] (easy axis) of a sample with a 5 nm MgO spacer is shown in (c). Finally, the extracted damping and inhomogeneous linewidth broadening, measured along hard axis (closed squares) and easy axis (open circles), are plotted for different MgO spacer thicknesses.

ΔH_0 in the easy axis measurement can be completely ascribed to two-magnon scattering; the obvious enhancement of the easy axis damping is not accounted for in this model, though. Indeed, all samples of the series display an anisotropic damping, compare Fig. 6.4 (d), with the easy axis damping being approximately a factor of three larger than the hard axis damping. Theoretically, an anisotropic intrinsic damping in Fe has been predicted [180, 181], but has to our knowledge experimentally not been verified. The two-magnon scattering contribution to the easy axis linewidth in our measurements complicates the analysis, therefore the question of anisotropic damping requires more thorough investigation, which is beyond the scope of this section.

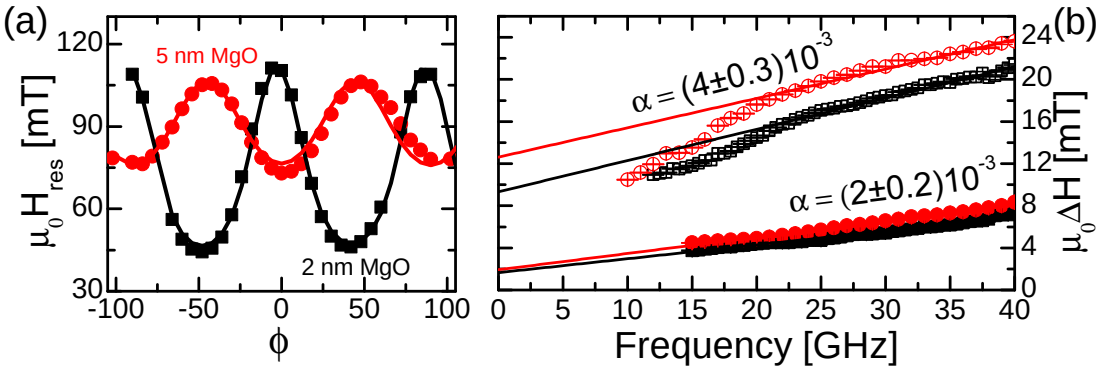

Figure 6.5: (a) shows IP angle dependence of the resonance field for $Co_{25}Fe_{75}$ samples grown on 4ML Fe/2 nm (black squares) and 4ML Fe/5 nm (red circles) seed layers measures at 12 GHz. Linewidths along hard axis (closed symbols) and easy axis(open symbols) are plotted against frequency in (b) for the two samples. The lines are linear fits of the data to Eq. (2.4).

As the hard axis damping does not display signs of a two-magnon contribution, we assume, that the measured hard axis damping approaches the intrinsic damping of the samples. We determine a hard axis damping of $(1.3 \pm 0.3) \cdot 10^{-3}$ for the sample grown on a 5 nm MgO seed layer. This value is lower than the RT damping of the poly-crystalline sample (compare Sec. 6.1), and approaches the goal value of achieving a damping value below $1 \cdot 10^{-3}$. We observe a dependence of the hard axis damping on MgO seed layer thickness, which we attribute to the influence of film roughness. It is notable that there seems to be no obvious correlation between damping and the magnitude of the four-fold anisotropy. Fig. 6.5 (a) shows the IP angle dependence of the H_{res} of two 5 nm $Co_{25}Fe_{75}$ samples, one grown on 4ML Fe/2 nm MgO and the other on 4ML Fe/5 nm MgO seed layers. Both samples display negligible uniaxial anisotropy and a clear four-fold anisotropy, with anisotropy constants of $K_1^{\parallel} = (2.4 \pm 0.5)\,\mathrm{J/m^3}$ and $K_1^{\parallel} = (1.2 \pm 0.7)\,\mathrm{J/m^3}$, respectively. However, the anisotropy axis for the sample grown on 4ML Fe/5 nm MgO

the anisotropy axis is shifted by 45° in relation to the other sample. We speculate that this rotation of the anisotropy axis is cause by thickness dependent strain in the MgO grown on Fe, that favors alignment of (100) MgO and (100) $Co_{25}Fe_{75}$ axis for a MgO thickness of 5 nm. In Fig. 6.5 (b) we plot the dependence of the linewidth on frequency for easy and hard axis and extract the hard and easy axis damping, yielding values of $(2 \pm 0.2) \cdot 10^{-3}$ and $(4 \pm 0.3) \cdot 10^{-3}$, respectively for both samples. This clearly shows that there is no correlation between the magnitude of $K_1^{\parallel}$ and the damping in the $Co_{25}Fe_{75}$ system.

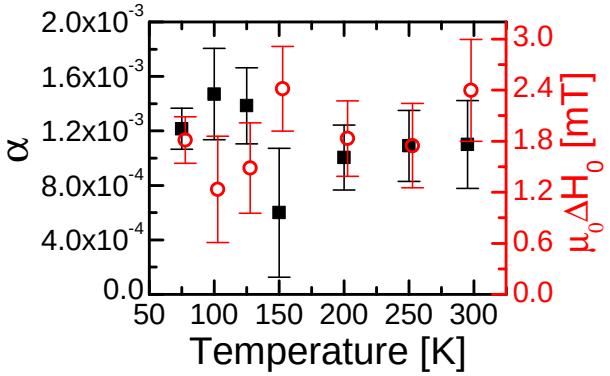

Figure 6.6: Temperature dependent measurement of the hard axis damping (left axis, black closed symbols) and inhomogeneous linewidth broadening (right axis, red open symbols) of a 10 nm $Co_{25}Fe_{75}$ sample deposited on 8 ML Fe/5 nmMgO seed layers.

The other samples grown with additional Fe seed layers of 4ML and 8ML thickness display a similar but altogether less predictable behavior of the damping with MgO seed layer thickness variation. The lowest hard axis damping in the sample series is achieved by the sample grown on a 8 ML Fe/5 nmMgO seed layers with a RT value of $(1.2 \pm 0.4) \cdot 10^{-3}$. Furthermore, we measured the temperature dependence of this sample, which is plotted in Fig. 6.6. Within errors, the hard axis damping does not display a dependence of temperature and scatters around the RT value, which as discussed in the previous section points to a non-negligible inter-band scattering contribution to the damping at RT.

7

Tuning of effective magnetization and damping in NiFe multilayers

Multilayer structures of Co and Ni or CoFe and Ni have been thoroughly investigated, as they can exhibit perpendicular magnetic anisotropy for select layer thicknesses and compositions [132, 182]. Furthermore, Shaw *et al.* [132] found that the damping of the CoFe multilayers can be tuned with layer structure, between the values found for the pure element damping. In the following we investigate this tunability of both damping and M_{eff} in NiFe multilayer structures. To this end we keep the total thickness of the multilayer stack constant at 10 nm and change both the number of layers and the relative Ni and Fe concentrations in the stack. The stack sequence is sketched in Fig. 7.1.

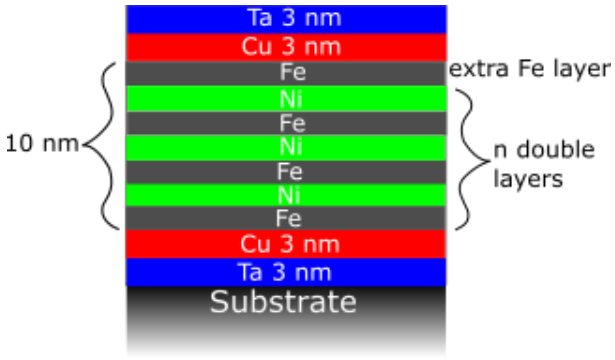

Figure 7.1: Schematic of the NiFe multilayer stack sequence.

Samples were deposited in the same way described in Sec. 4.1 with Ta/Cu seed and Cu/Ta capping layers. In order to keep the spin pumping contribution to the measured damping constant over the range of samples and to prevent interdiffusion between Ni and the Cu cap and seed layers, an additional Fe layer on top of the stack was introduced. The measured M_{eff} and α for the multilayers are plotted in Fig. 7.2 (a) and (b), respectively. For comparison M_{eff} and the damping of 10 nm thick alloys with the same concentration, as well as the the calculated spin density wighted M_{eff} and damping are also plotted.

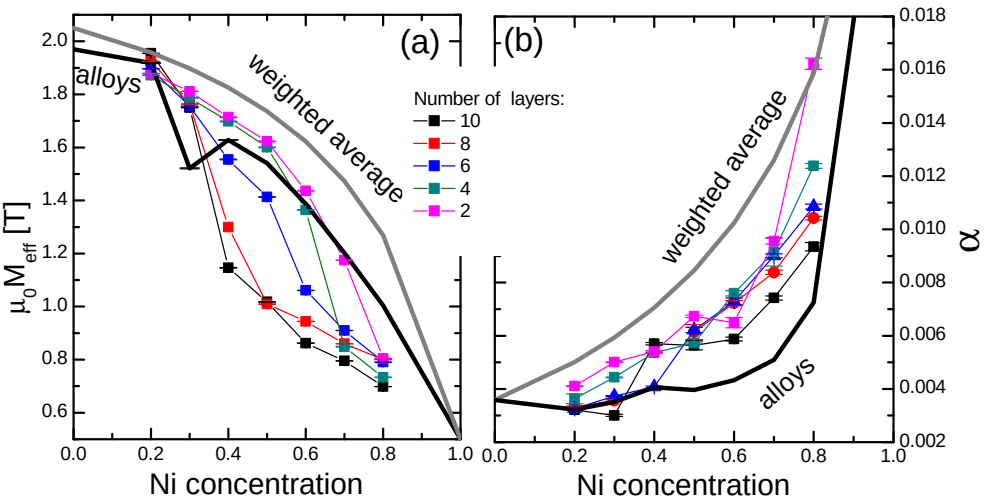

Figure 7.2: The effective magnetization M_{eff} and the damping α for NiFe multilayer structures measured via FMR are plotted in (a) and (b), respectively. The number of layers refers to the number of Ni-Fe double layers in a stack of 10 nm thickness. For comparison the alloy values of M_{eff} and α are added to both plots (black lines), as well as the bulk averaged damping (gray line). The measured multilayer damping lies, within errors, exclusively between these two boundaries.

Not surprisingly, M_{eff} for the multilayer structures deviates significantly from the M_{eff} of the alloys and follows for a low number of layers a weighted average behavior with anisotropy offset. M_{eff} is significantly lowered though, for larger double layer repetition rates and close to equiatomic concentration. This behavior can be understood when considering the perpendicular anisotropy induced at the Ni-Fe interfaces [183]. Each interface induces an additional perpendicular anisotropy contribution, thus lowering M_{eff} with rising number of layers. However, the influence of additional interfaces becomes smaller towards the concentration extrema. On the iron rich side the behavior of M_{eff} with layer number even switches and additional layers cause a rise of M_{eff}. This behavior could be caused for many reasons, such as different interface roughness, interfacial intermixing, or a dependence of the anisotropy on layer thickness [131]. A reasonable estimate of the expected M_{eff} for the multilayer structures would require precise knowledge of interface properties, going well beyond the scope of this section, therefore, this discussion is limited to the experimental findings.
The measured multilayer damping can be found almost exclusively between the limits given by the alloy damping and the bulk averaged damping. Generally, a decrease of α_{tot} with a increasing number of layers can be observed. This behavior is an indication that as the thickness of the individual layers decreases, the damping of the multilayer stack behaves more alloy like, which can be quite intuitively explained: For thick exchange coupled layers interface effects will be

negligible and thus the intrinsic damping in each layer will be largely unaffected. The total damping of the stack will behave close to a spin density weighted average of the individual layer damping. For thinner layers ($\leq 1\,\mathrm{nm}$) however, the damping will be dominated by the interfaces and - especially considering intermixing at the interface - it is conceivable that the damping at the interfaces is closer to that of a disordered alloy. Therefore, the damping in multilayer structures, consisting of many thin layers will behave more like an alloy of the same constituents. Of course this argument is only valid for thick enough multilayers of similar elements, where the symmetry breaking at the interface does not have a significant influence on the band structure.
From the data it is obvious that the NiFe multilayers give access to a wide range of material parameters, which cannot be achieved by alloying. Most notable is the possibility to simultaneously lower M_{eff} and α_{tot} for equiatomic concentrations, especially since many metallic alloys with low damping seem to simultaneously exhibit large M_{eff} [74,153,184]. Multilayers of Ni and Fe allow for a material with M_{eff} of $\approx$1.2 T, which is close to M_{eff} of the commonly used Permalloy, but with a damping close to the one of pure Fe.

8

Summary and outlook

The objective of this work was the investigation of magnetic damping processes in the binary 3d transition metal alloys NiCo, NiFe, and CoFe in a FMR experiment. The focus was on the determination of the intrinsic damping and its comparison to ab initio theories. To this end we characterized the magnetic properties Ni_xCo_{1-x}, Ni_xFe_{1-x}, and Co_xFe_{1-x} sample series over the complete range of alloy compositions. The saturation magnetization and spectroscopic g-factor of all samples match the bulk values reasonably well, thus confirming well the controlled magnetic properties of the sample series. However, the sample and measurement geometry induce significant additional extrinsic contributions to the measured damping, namely radiative damping and spin pumping. We directly quantify these two extrinsic contributions and calculate the intrinsic damping of all samples enabling a detailed comparison of *ab initio* calculations to our measurements. In most cases this comparison yields exceptional qualitative and quantitative agreement. The Co_xFe_{1-x} system stands out, as it displays strong non-monotonous dependence of the damping on alloy composition with a minimum value of the damping of $(2.3 \pm 0.1) \cdot 10^{-3}$ at a Co-concentration of 25 %. After accounting for the extrinsic contributions we find an intrinsic value of the damping for the $Co_{25}Fe_{75}$ alloy of $(5.0 \pm 1.8) \cdot 10^{-4}$, in agreement with theory. We explain this exceptionally low value of the damping by an unique feature in the band structure: The density of states at the Fermi energy, which is directly correlated to both interband and intraband intrinsic damping mechanisms, exhibits a minimum at 25 % Co, thus effecting the minimum in the intrinsic damping.
As damping below $1 \cdot 10^{-3}$ is usually only observed in insulating or half metallic magnetic materials, the low value of the damping for the $Co_{25}Fe_{75}$ alloy in combination with its large saturation magnetization of 2.3 T makes it a promising material for spintronics and magnonics applications. However, for the implementation in devices, the total damping determines the operational parameters. We therefore implement a new sample and measurement geometry, which effectively suppresses extrinsic contributions to the damping. This was achieved by growing $Co_{25}Fe_{75}$ samples between insulating MgO cap and seed layers. Thus we were able to produce magnetically isotropic poly-crystalline samples with an isotropic damping of $(1.6 \pm 0.2) \cdot 10^{-3}$. The damping of this sample displays no discernible

dependence on temperature and we conclude that the inter-band transitions play a non-negligible role for the magnetic damping. In order to minimize this intrinsic damping mechanism, we deposited another set of samples on a perfectly crystalline GaAs substrate. The sample series growth was epitaxial, as confirmed by RHEED and all samples exhibit a four-fold magnetic IP anisotropy, also indicative for crystallinity. We find a value of the damping measured along the hard axis of $(1.2 \pm 0.4) \cdot 10^{-3}$ for a $Co_{25}Fe_{75}$ sample grown on 8 ML Fe/5 nm MgO seed layers and a value of $(1.3 \pm 0.3) \cdot 10^{-3}$ for a sample just grown on a 5 nm MgO seed layer. Both of those values approach the theoretically predicted and experimentally deduced value of $(5 \pm 1.8) \cdot 10^{-4}$, however, they still are approximately a factor of 2 larger. The damping throughout the whole sample series was highly anisotropic, with the easy axis damping a factor 2-3 larger than the hard axis damping. We attribute this partially to a two-magnon scattering process enhancing the damping.
Finally, we demonstrate that a wide range of material properties are accessible by growing multilayers of Ni and Fe. Variation of the layer repetition rate and respective Ni and Fe compositions in a stack of fixed thickness allows for a targeted tuning of the material properties within well defined limits.

This work presents a comprehensive study of the damping in 3d transition metal alloys and multilayers. The most noteworthy result is the discovery of an ultra-low damping value for the $Co_{25}Fe_{75}$ alloy, a material which could exhibit spin wave diffusion lengths exceeding 10 µm. However, further investigation on the suitability of the low damping isotropic $Co_{25}Fe_{75}$ for devices are necessary. First test could be FMR and spin wave measurements on structured samples, to measure material properties locally and after structuring processes. Another open question remaining is the reason for the anisotropic damping measured in the epitaxial $Co_{25}Fe_{75}$ samples. As theory does not predict this large an anisotropy of the damping, a thorough investigation of the frequency dependence of two-magnon scattering with measurements to larger frequencies is necessary.

Bibliography

[1] G. E. Moore. *Cramming more components onto integrated circuits.* IEEE Solid-State Circuits Society Newsletter **11**, 33-35 (2006).

[2] N. Z. Haron and S. Hamdioui in *Why is CMOS scaling coming to an END?*, 2008 3rd International Design and Test Workshop, 98-103, (2008).

[3] D. L. Klein, R. Roth, A. K. L. Lim, A. P. Alivisatos, and P. L. McEuen. *A single-electron transistor made from a cadmium selenide nanocrystal.* Nature **389**, 699–701 (1997).

[4] L. Guo, E. Leobandung, and S. Y. Chou. *A Silicon Single-Electron Transistor Memory Operating at Room Temperature.* Science **275**, 649–651 (1997).

[5] Samsung. https://news.samsung.com/global/samsung-starts-industrys-first-mass-production-of-system-on-chip-with-10-nanometer-finfet-technology, (Downloaded 14.1.2017).

[6] N. S. Kim, T. Austin, D. Baauw, T. Mudge, K. Flautner, J. S. Hu, M. J. Irwin, M. Kandemir, and V. Narayanan. *Leakage current: Moore's law meets static power.* Computer **36**, 68-75 (2003).

[7] K. J. Kuhn. *Considerations for Ultimate CMOS Scaling.* IEEE Transactions on Electron Devices **59**, 1813-1828 (2012).

[8] D. Mamaluy, X. Gao, and B. Tierney in *How much time does FET scaling have left?*, 2014 International Workshop on Computational Electronics (IWCE), 1-2, (2014).

[9] I. Žutić, J. Fabian, and S. Das Sarma. *Spintronics: Fundamentals and applications.* Rev. Mod. Phys. **76**, 323–410 (2004).

[10] S. Bader and S. Parkin. *Spintronics.* Annual Review of Condensed Matter Physics **1**, 71-88 (2010).

[11] A. Hoffmann and S. D. Bader. *Opportunities at the Frontiers of Spintronics.* Phys. Rev. Applied **4**, 047001 (2015).

[12] H. Ohno, M. D. Stiles, and B. Dieny. *Spintronics.* Proceedings of the IEEE. Institute of Electrical and Electronics Engineers **104**, 1782–1786 (2016).

[13] C. Chappert, A. Fert, and F. N. Van Dau. *The emergence of spin electronics in data storage.* Nat Mater **6**, 813–823 (2007).

[14] J. Z. Sun, M. C. Gaidis, E. J. O'Sullivan, E. A. Joseph, G. Hu, D. W. Abraham, J. J. Nowak, P. L. Trouilloud, Y. Lu, S. L. Brown, D. C. Worledge, and W. J. Gallagher. *A three-terminal spin-torque-driven magnetic switch.* Applied Physics Letters **95**, 083506 (2009).

[15] S. A. Wolf, J. Lu, M. R. Stan, E. Chen, and D. M. Treger. *The Promise of Nanomagnetics and Spintronics for Future Logic and Universal Memory.* Proceedings of the IEEE **98**, 2155-2168 (2010).

[16] Z. Pajouhi, S. Venkataramani, K. Yogendra, A. Raghunathan, and K. Roy. *Exploring Spin-Transfer-Torque Devices for Logic Applications.* IEEE Transactions on Computer-Aided Design of Integrated Circuits and Systems **34**, 1441-1454 (2015).

[17] P. A. Grünberg and K. Takanashi in *Spintronics: Towards devices with lower energy consumption*, 10th IEEE International Conference on Nanotechnology, 3, (2010).

[18] M. Sharad and K. Roy. *Spintronic Switches for Ultralow Energy On-Chip and Interchip Current-Mode Interconnects.* IEEE Electron Device Letters **34**, 1068-1070 (2013).

[19] Y. Zhang, W. Zhao, J. O. Klein, W. Kang, D. Querlioz, Y. Zhang, D. Ravelosona, and C. Chappert in *Spintronics for low-power computing*, 2014 Design, Automation Test in Europe Conference Exhibition (DATE), 1-6, (2014).

[20] S. Mangin, Y. Henry, D. Ravelosona, J. A. Katine, and E. E. Fullerton. *Reducing the critical current for spin-transfer switching of perpendicularly magnetized nanomagnets.* Applied Physics Letters **94**, 012502 (2009).

[21] L. Su, Y. Zhang, J.-O. Klein, Y. Zhang, A. Bournel, A. Fert, and W. Zhao. *Current-limiting challenges for all-spin logic devices.* Scientific Reports **5**, 14905 (2015).

[22] V. V. Kruglyak, S. O. Demokritov, and D. Grundler. *Magnonics.* Journal of Physics D: Applied Physics **43**, 264001 (2010).

[23] A. V. Chumak, V. I. Vasyuchka, A. A. Serga, and B. Hillebrands. *Magnon spintronics.* Nat Phys **11**, 453–461 (2015).

[24] L. Landau and E. Lifshitz. *Theory of the dispersion of magnetic permeability in ferromagnetic bodies.* Phys. Z. Sowietunion, 8, 153 (1935).

[25] T. L. Gilbert. *A phenomenological theory of damping in ferromagnetic materials.* IEEE Trans. Mag. 40 (6): 3443-3449 (2004).

[26] H. Ebert, S. Mankovsky, D. Ködderitzsch, and P. J. Kelly. *Ab Initio Calculation of the Gilbert Damping Parameter via the Linear Response Formalism.* Phys. Rev. Lett. **107**, 066603-066607 (2011).

[27] K. Gilmore, Y. U. Idzerda, and M. D. Stiles. *Identification of the Dominant Precession-Damping Mechanism in Fe, Co, and Ni by First-Principles Calculations.* Phys. Rev. Lett. **99**, 027204 (2007).

[28] V. Kambersky and C. E. Patton. *Spin-wave relaxation and phenomenological damping in ferromagnetic resonance.* Phys. Rev. B **11**, 2668–2672 (1975).

[29] V. Kamberský. *On ferromagnetic resonance damping in metals.* Czechoslovak Journal of Physics B **26**, 1366-1383 (1976).

[30] A. Brataas, Y. Tserkovnyak, and G. E. W. Bauer. *Scattering Theory of Gilbert Damping.* Phys. Rev. Lett. **101**, 037207 (2008).

[31] S. Emori, U. Bauer, S.-M. Ahn, E. Martinez, and G. S. D. Beach. *Current-driven dynamics of chiral ferromagnetic domain walls.* Nat Mater **12**, 611–616 (2013).

[32] E. Jue, C. K. Safeer, M. Drouard, A. Lopez, P. Balint, L. Buda-Prejbeanu, O. Boulle, S. Auffret, A. Schuhl, A. Manchon, I. M. Miron, and G. Gaudin. *Chiral damping of magnetic domain walls.* Nat Mater **15**, 272–277 (2016).

[33] H. Chang, P. Li, W. Zhang, T. Liu, A. Hoffmann, L. Deng, and M. Wu. *Nanometer-Thick Yttrium Iron Garnet Films With Extremely Low Damping.* Magnetics Letters, IEEE **5**, 1-4 (2014).

[34] L. J. Cornelissen, J. Liu, R. A. Duine, J. B. Youssef, and B. J. van Wees. *Long-distance transport of magnon spin information in a magnetic insulator at room temperature.* Nat Phys **11**, 1022–1026 (2015).

[35] C. Liu, C. K. A. Mewes, M. Chshiev, T. Mewes, and W. H. Butler. *Origin of low Gilbert damping in half metals.* Applied Physics Letters **95**, 022509 (2009).

[36] S. Mizukami, D. Watanabe, M. Oogane, Y. Ando, Y. Miura, M. Shirai, and T. Miyazaki. *Low damping constant for Co_2FeAl Heusler alloy films and its correlation with density of states.* Journal of Applied Physics **105**, 07D306 (2009).

[37] P. Dürrenfeld, F. Gerhard, J. Chico, R. K. Dumas, M. Ranjbar, A. Bergman, L. Bergqvist, A. Delin, C. Gould, L. W. Molenkamp, and J. Åkerman. *Tunable damping, saturation magnetization, and exchange stiffness of half-Heusler NiMnSb thin films.* Phys. Rev. B **92**, 214424 (2015).

[38] T. Liu, H. Chang, V. Vlaminck, Y. Sun, M. Kabatek, A. Hoffmann, L. Deng, and M. Wu. *Ferromagnetic resonance of sputtered yttrium iron garnet nanometer films.* Journal of Applied Physics **115**, 17A501 (2014).

[39] A. Sombra, E. Mallmann, J. Goes, and P. Fechine. *Yttrium Iron Garnet: Properties and Applications Review.* Solid State Phenomena **202**, 65–96 (2013).

[40] P. W. Jang and J. Y. Kim. *New growth method of solid phase epitaxy in sputtered YIG films.* IEEE Transactions on Magnetics **37**, 2438-2440 (2001).

[41] U. Geiersbach, A. Bergmann, and K. Westerholt. *Structural, magnetic and magnetotransport properties of thin films of the Heusler alloys Cu_2MnAl, Co_2MnSi, Co_2MnGe and Co_2MnSn.* Journal of Magnetism and Magnetic Materials **240**, 546 - 549 (2002). 4th International Symposium on Metallic Multilayers.

[42] R. M. Bozorth. *Ferromagnetism.* IEEE Press, 2003.

[43] S. Mankovsky, D. Ködderitzsch, G. Woltersdorf, and H. Ebert. *First-principles calculation of the Gilbert damping parameter via the linear response formalism with application to magnetic transition metals and alloys.* Phys. Rev. B **87**, 014430 (2013).

[44] J. M. Lock. *Eddy current damping in thin metallic ferromagnetic films.* British Journal of Applied Physics **17**, 1645 (1966).

[45] Y. Tserkovnyak, A. Brataas, and G. E. W. Bauer. *Enhanced Gilbert Damping in Thin Ferromagnetic Films.* Phys. Rev. Lett. **88**, 117601 (2002).

[46] M. A. W. Schoen, J. M. Shaw, H. T. Nembach, M. Weiler, and T. J. Silva. *Radiative damping in waveguide-based ferromagnetic resonance measured via analysis of perpendicular standing spin waves in sputtered permalloy films.* Phys. Rev. B **92**, 184417 (2015).

[47] J. H. E. Griffiths. *Anomalous High-frequency Resistance of Ferromagnetic Metals.* Nature **158**, 670-671 (1946).

[48] C. Kittel. *Interpretation of Anomalous Larmor Frequencies in Ferromagnetic Resonance Experiment.* Phys. Rev. **71**, 270–271 (1947).

[49] C. Kittel. *Physical Theory of Ferromagnetic Domains.* Rev. Mod. Phys. **21**, 541–583 (1949).

[50] J. Bland and B. Heinrich, eds. *Ultrathin Magnetic Structures III.* Springer-Verlag Berlin Heidelberg, 1994.

[51] C. Kittel. *Einführung in die Festkörperphysik.* Oldenbourg, München, 2002.

[52] H. T. Nembach, T. J. Silva, J. M. Shaw, M. L. Schneider, M. J. Carey, S. Maat, and J. R. Childress. *Perpendicular ferromagnetic resonance measurements of damping and Lande g-factor in sputtered* $(Co_2Mn)_{1-x}Ge_x$ *films.* Phys. Rev. B **84**, 054424 (2011).

[53] B. Heinrich, J. F. Cochran, and R. Hasegawa. *FMR linebroadening in metals due to two-magnon scattering.* Journal of Applied Physics **57**, 3690-3692 (1985).

[54] D. J. Twisselmann and R. D. McMichael. *Intrinsic damping and intentional ferromagnetic resonance broadening in thin Permalloy films.* Journal of Applied Physics **93**, 6903-6905 (2003).

[55] R. D. McMichael, D. J. Twisselmann, and A. Kunz. *Localized Ferromagnetic Resonance in Inhomogeneous Thin Films.* Phys. Rev. Lett. **90**, 227601 (2003).

[56] J. Bland and B. Heinrich, eds. *Ultrathin Magnetic Structures II.* Springer-Verlag Berlin Heidelberg, 1994.

[57] G. Woltersdorf. *Spin-Pumping and Two-Magnon Scattering in Magnetic Multilayers.* Simon Fraser University, PhD thesis, 2004.

[58] Y. Ding, T. J. Klemmer, and T. M. Crawford. *A coplanar waveguide permeameter for studying high-frequency properties of soft magnetic materials.* Journal of Applied Physics **96**, 2969-2972 (2004).

[59] Z. Celinski, K. Urquhart, and B. Heinrich. *Using ferromagnetic resonance to measure the magnetic moments of ultrathin films.* Journal of Magnetism and Magnetic Materials **166**, 6 - 26 (1997).

[60] S. M. Bhagat and P. Lubitz. *Temperature variation of ferromagnetic relaxation in the* 3*d transition metals.* Phys. Rev. B **10**, 179–185 (1974).

[61] K. Gilmore. *Precession damping in itinerant ferromagnets.* Montana State University Bozeman, Montana, PhD thesis, 2007.

[62] B. Heinrich and Z. Frait. *Temperature Dependence of the FMR Linewidth of Iron Single-Crystal Platelets.* physica status solidi (b) **16**, K11–K14 (1966).

[63] A. A. Starikov, P. J. Kelly, A. Brataas, Y. Tserkovnyak, and G. E. W. Bauer. *Unified First-Principles Study of Gilbert Damping, Spin-Flip Diffusion, and Resistivity in Transition Metal Alloys.* Phys. Rev. Lett. **105**, 236601 (2010).

[64] I. Turek, J. Kudrnovský, and V. Drchal. *Nonlocal torque operators in ab initio theory of the Gilbert damping in random ferromagnetic alloys.* Phys. Rev. B **92**, 214407 (2015).

[65] V. Kamberský. *FMR linewidth and disorder in metals.* Czechoslovak Journal of Physics B **34**, 1111-1124 (1984).

[66] V. Kamberský. *On the Landau-Lifshitz relaxation in ferromagnetic metals.* Can. J. Phys. **48**, 2906 (1970).

[67] B. Heinrich, D. Fraitova, and V. Kambersky. *The Influence of s-d Exchange on Relaxation of Magnons in Metals.* physica status solidi (b) **23**, 501-507 (1967).

[68] R. Meservey and P. Tedrow. *Spin-polarized electron tunneling.* Physics Reports **238**, 173 - 243 (1994).

[69] J. Kübler. *Theory of Itinerant Electron Magnetism.* Oxford University Press Inc., New York, 2000.

[70] D. Thonig and J. Henk. *Gilbert damping tensor within the breathing Fermi surface model: anisotropy and non-locality.* New J. Phys. **16**, 013032 (2014).

[71] V. Kamberský. *Spin-orbital Gilbert damping in common magnetic metals.* Phys. Rev. B **76**, 134416 (2007).

[72] Y. Liu, Z. Yuan, R. J. H. Wesselink, A. A. Starikov, and P. J. Kelly. *Interface Enhancement of Gilbert Damping from First Principles.* Phys. Rev. Lett. **113**, 207202 (2014).

[73] Z. Yuan, K. M. D. Hals, Y. Liu, A. A. Starikov, A. Brataas, and P. J. Kelly. *Gilbert Damping in Noncollinear Ferromagnets.* Phys. Rev. Lett. **113**, 266603 (2014).

[74] M. A. W. Schoen, D. Thonig, M. L. Schneider, T. J. Silva, H. T. Nembach, O. Eriksson, O. Karis, and J. M. Shaw. *Ultra-low magnetic damping of a metallic ferromagnet.* Nat. Phys **12**, 839-842 (2016).

[75] J. Mallinson. *The Foundations of Magnetic Recording.* San Diego: Academic Press, 2nd ed., 1993.

[76] V. L'vov. *Wave Turbulence Under Parametric Excitation.* Springer-Verlag, Berlin, Heidelberg, 1994.

[77] I. S. Maksymov and M. Kostylev. *Impact of conducting nonmagnetic layers on the magnetization dynamics in thin-film magnetic nanostructures.* Journal of Applied Physics **113** (2013).

[78] M. Bailleul. *Shielding of the electromagnetic field of a coplanar waveguide by a metal film: Implications for broadband ferromagnetic resonance measurements.* Applied Physics Letters **103** (2013).

[79] M. Kostylev. *Strong asymmetry of microwave absorption by bilayer conducting ferromagnetic films in the microstrip-line based broadband ferromagnetic resonance.* Journal of Applied Physics **106**, 043903 (2009).

[80] R. F. Soohoo. *General Exchange Boundary Condition and Surface Anisotropy Energy of a Ferromagnet.* Phys. Rev. **131**, 594–601 (1963).

[81] S. Mathias, C. La-O-Vorakiat, P. Grychtol, P. Granitzka, E. Turgut, J. M. Shaw, R. Adam, H. T. Nembach, M. E. Siemens, S. Eich, C. M. Schneider, T. J. Silva, M. Aeschlimann, M. M. Murnane, and H. C. Kapteyn. *Probing the timescale of the exchange interaction in a ferromagnetic alloy.* Proceedings of the National Academy of Sciences **109**, 4792-4797 (2012).

[82] T. Maeda, H. Yamauchi, and H. Watanabe. *Spin Wave Resonance and Exchange Parameters in fcc Fe-Ni Alloys.* Journal of the Physical Society of Japan **35**, 1635-1642 (1973).

[83] G. C. Bailey and C. Vittoria. *Presence of Magnetic Surface Anisotropy in Permalloy Films.* Phys. Rev. B **8**, 3247–3251 (1973).

[84] H. T. Nembach, J. M. Shaw, C. T. Boone, and T. J. Silva. *Mode- and Size-Dependent Landau-Lifshitz Damping in Magnetic Nanostructures: Evidence for Nonlocal Damping.* Phys. Rev. Lett. **110**, 117201 (2013).

[85] P. Pincus. *Excitation of Spin Waves in Ferromagnets: Eddy Current and Boundary Condition Effects.* Phys. Rev. **118**, 658–664 (1960).

[86] Y. Li and W. Bailey. *Wavenumber-dependent Gilbert damping in metallic ferromagnets.* ArXiv e-prints (2014).

[87] J. M. Shaw, T. J. Silva, M. L. Schneider, and R. D. McMichael. *Spin dynamics and mode structure in nanomagnet arrays: Effects of size and thickness on linewidth and damping.* Phys. Rev. B **79**, 184404 (2009).

[88] M. Zwierzycki, Y. Tserkovnyak, P. J. Kelly, A. Brataas, and G. E. W. Bauer. *First-principles study of magnetization relaxation enhancement and spin transfer in thin magnetic films.* Phys. Rev. B **71**, 064420 (2005).

[89] A. Brataas, G. E. Bauer, and P. J. Kelly. *Non-collinear magnetoelectronics.* Physics Reports **427**, 157 - 255 (2006).

[90] C. T. Boone, H. T. Nembach, J. M. Shaw, and T. J. Silva. *Spin transport parameters in metallic multilayers determined by ferromagnetic resonance measurements of spin-pumping.* Journal of Applied Physics **113**, 153906 (2013).

[91] M. Weiler, J. M. Shaw, H. T. Nembach, and T. J. Silva. *Phase-Sensitive Detection of Spin Pumping via the ac Inverse Spin Hall Effect.* Phys. Rev. Lett. **113**, 157204 (2014).

[92] M. Obstbaum, M. Härtinger, H. G. Bauer, T. Meier, F. Swientek, C. H. Back, and G. Woltersdorf. *Inverse spin Hall effect in $Ni_{81}Fe_{19}$/normal-metal bilayers.* Phys. Rev. B **89**, 060407 (2014).

[93] M. Obstbaum. *Inverse spin Hall effect in metallic heterostructures.* University of Regensburg, PhD thesis, 2016.

[94] M. Weiler, M. Althammer, M. Schreier, J. Lotze, M. Pernpeintner, S. Meyer, H. Huebl, R. Gross, A. Kamra, J. Xiao, Y.-T. Chen, H. Jiao, G. E. W. Bauer, and S. T. B. Goennenwein. *Experimental Test of the Spin Mixing Interface Conductivity Concept.* Phys. Rev. Lett. **111**, 176601 (2013).

[95] A. F. Mayadas, J. F. Janak, and A. Gangulee. *Resistivity of Permalloy thin films.* Journal of Applied Physics **45**, 2780-2781 (1974).

[96] J. D. Vries. *Temperature and thickness dependence of the resistivity of thin polycrystalline aluminium, cobalt, nickel, palladium, silver and gold films.* Thin Solid Films **167**, 25 - 32 (1988).

[97] M. A. W. Schoen, J. Lucassen, H. T. Nembach, T. J. Silva, B. Koopmans, C. H. Back, and J. M. Shaw. *Magnetic properties of ultra-thin 3d transition-metal binary alloys I: spin and orbital moments, and anisotropy, and confirmation of Slater-Pauling behavior.* arXiv:1701.02177 (2017).

[98] M. A. W. Schoen, J. Lucassen, H. T. Nembach, T. J. Silva, B. Koopmans, C. H. Back, and J. M. Shaw. *Magnetic properties in ultra-thin 3d transition metal alloys II: experimental verification of quantitative theories of damping and spin-pumping.* arXiv:1701.02475 (2017).

[99] P. Amiri, Z. Zeng, P. Upadhyaya, G. Rowlands, H. Zhao, I. Krivorotov, J. Wang, H. Jiang, J. Katine, J. Langer, K. Galatsis, and K. Wang. *Low Write-Energy Magnetic Tunnel Junctions for High-Speed Spin-Transfer-Torque MRAM.* Electron Device Letters, IEEE **32**, 57-59 (2011).

[100] S. Kaka, M. R. Pufall, W. H. Rippard, T. J. Silva, S. E. Russek, J. A. Katine, and M. Carey. *Spin transfer switching of spin valve nanopillars using nanosecond pulsed currents.* Journal of Magnetism and Magnetic Materials **286**, 375 - 380 (2005). Proceedings of the 5th International Symposium on Metallic Multilayers.

[101] C. A. Bauer and P. E. Wigen. *Spin-Wave Resonance Studies in Invar Films.* Phys. Rev. B **5**, 4516–4524 (1972).

[102] A. J. P. Meyer and G. Asch. *Experimental g' and g Values of Fe, Co, Ni, and Their Alloys.* Journal of Applied Physics **32**, S330-S333 (1961).

[103] R. A. Reck and D. L. Fry. *Orbital and Spin Magnetization in Fe-Co, Fe-Ni, and Ni-Co.* Phys. Rev. **184**, 492–495 (1969).

[104] F. El Gabaly, S. Gallego, C. Muñoz, L. Szunyogh, P. Weinberger, C. Klein, A. K. Schmid, K. F. McCarty, and J. de la Figuera. *Imaging Spin-Reorientation Transitions in Consecutive Atomic Co Layers on Ru(0001).* Phys. Rev. Lett. **96**, 147202 (2006).

[105] M. Farle, B. Mirwald-Schulz, A. N. Anisimov, W. Platow, and K. Baberschke. *Higher-order magnetic anisotropies and the nature of the spin-reorientation transition in face-centered-tetragonal Ni(001)/Cu(001).* Phys. Rev. B **55**, 3708–3715 (1997).

[106] J. Prokop, D. A. Valdaitsev, A. Kukunin, M. Pratzer, G. Schönhense, and H. J. Elmers. *Strain-induced magnetic anisotropies in Co films on Mo(110).* Phys. Rev. B **70**, 184423 (2004).

[107] C. Rizal, P. Gyawali, I. Kshattry, and R. K. Pokharel. *Strain-induced magnetoresistance and magnetic anisotropy properties of Co/Cu multilayers.* Journal of Applied Physics **111** (2012).

[108] D. Sander. *The correlation between mechanical stress and magnetic anisotropy in ultrathin films.* Reports on Progress in Physics **62**, 809 (1999).

[109] C. M. Schneider, P. Bressler, P. Schuster, J. Kirschner, J. J. de Miguel, and R. Miranda. *Curie temperature of ultrathin films of fcc-cobalt epitaxially grown on atomically flat Cu(100) surfaces.* Phys. Rev. Lett. **64**, 1059–1062 (1990).

[110] L. Sun, P. C. Searson, and C. L. Chien. *Finite-size effects in nickel nanowire arrays.* Phys. Rev. B **61**, R6463–R6466 (2000).

[111] A. García-Arribas, E. Fernández, V. A. Svalov, V. G. Kurlyandskaya, A. Barrainkua, D. Navas, and M. J. Barandiaran. *Tailoring the magnetic anisotropy of thin film permalloy microstrips by combined shape and induced anisotropies.* The European Physical Journal B **86**, 1–7 (2013).

[112] G. Bayreuther, M. Dumm, B. Uhl, R. Meier, and W. Kipferl. *Magnetocrystalline volume and interface anisotropies in epitaxial films: Universal relation and Nèel's model (invited).* Journal of Applied Physics **93**, 8230-8235 (2003).

[113] G. Bayreuther and G. Lugert. *Magnetization of ultra-thin epitaxial Fe films.* Journal of Magnetism and Magnetic Materials **35**, 50 - 52 (1983).

[114] M. Dumm, M. Zölfl, R. Moosb§hler, M. Brockmann, T. Schmidt, and G. Bayreuther. *Magnetism of ultrathin FeCo (001) films on GaAs(001).* Journal of Applied Physics **87**, 5457-5459 (2000).

[115] B. Heinrich, J. F. Cochran, A. S. Arrott, S. T. Purcell, K. B. Urquhart, J. R. Dutcher, and W. F. Egelhoff. *Development of magnetic anisotropies in ultrathin epitaxial films of Fe(001) and Ni(001).* Applied Physics A **49**, 473-490 (1989).

[116] F. Huang, M. T. Kief, G. J. Mankey, and R. F. Willis. *Magnetism in the few-monolayers limit: A surface magneto-optic Kerr-effect study of the magnetic behavior of ultrathin films of Co, Ni, and Co-Ni alloys on Cu(100) and Cu(111).* Phys. Rev. B **49**, 3962–3971 (1994).

[117] E. Reiger, E. Reinwald, G. Garreau, M. Ernst, M. Zölfl, F. Bensch, S. Bauer, H. Preis, and G. Bayreuther. *Magnetic moments and anisotropies in ultrathin epitaxial Fe films on ZnSe(001).* Journal of Applied Physics **87**, 5923-5925 (2000).

[118] J. M. Shaw, H. T. Nembach, T. J. Silva, and C. T. Boone. *Precise determination of the spectroscopic g-factor by use of broadband ferromagnetic resonance spectroscopya).* Journal of Applied Physics **114**, 243906 (2013).

[119] M. T. Kief and W. F. Egelhoff. *Growth and structure of Fe and Co thin films on Cu(111), Cu(100), and Cu(110): A comprehensive study of metastable film growth.* Phys. Rev. B **47**, 10785–10814 (1993).

[120] J. Pelzl, R. Meckenstock, D. Spoddig, F. Schreiber, J. Pflaum, and Z. Frait. *Spin-orbit-coupling effects on g -value and damping factor of the ferromagnetic resonance in Co and Fe films.* Journal of Physics: Condensed Matter **15**, S451 (2003).

[121] M. Tischer, O. Hjortstam, D. Arvanitis, J. Hunter Dunn, F. May, K. Baberschke, J. Trygg, J. M. Wills, B. Johansson, and O. Eriksson. *Enhancement of Orbital Magnetism at Surfaces: Co on Cu(100).* Phys. Rev. Lett. **75**, 1602–1605 (1995).

[122] L. Pauling. *The Nature of the Interatomic Forces in Metals.* Phys. Rev. **54**, 899–904 (1938).

[123] J. C. Slater. *Electronic Structure of Alloys.* Journal of Applied Physics **8**, 385-390 (1937).

[124] J. Bland and B. Heinrich, eds. *Ultrathin Magnetic Structures I.* Springer-Verlag Berlin Heidelberg, 1994.

[125] C. H. Lambert, A. Rajanikanth, T. Hauet, S. Mangin, E. E. Fullerton, and S. Andrieu. *Quantifying perpendicular magnetic anisotropy at the Fe-MgO(001) interface.* Applied Physics Letters **102**, 122410 (2013).

[126] D. Marko, T. Strache, K. Lenz, J. Fassbender, and R. Kaltofen. *Determination of the saturation magnetization of ion irradiated Py/Ta samples using polar magneto-optical Kerr effect and ferromagnetic resonance.* Applied Physics Letters **96**, 022503 (2010).

[127] A. H. Morrish. *The Physical Principles of Magnetism.* IEEE Press, 2001.

[128] P. Bruno. *Magnetic surface anisotropy of cobalt and surface roughness effects within Neel's model.* J . Phys. F: Met. Phys. **18**, 1291-1298 (1988).

[129] L. Neel. *L'approche á la saturation de la magnétostriction.* J. Phys. Radium **15**, 376-378 (1954).

[130] P. Bruno and J. P. Renard. *Magnetic surface anisotropy of transition metal ultrathin films.* Applied Physics A **49**, 499–506 (1989).

[131] M. T. Johnson, P. J. H. Bloemen, F. J. A. den Broeder, and J. J. de Vries. *Magnetic anisotropy in metallic multilayers.* Reports on Progress in Physics **59**, 1409 (1996).

[132] J. M. Shaw, H. T. Nembach, and T. J. Silva. *Damping phenomena in $Co_{90}Fe_{10}$/Ni multilayers and alloys.* Applied Physics Letters **99**, 012503 (2011).

[133] M. Watanabe, M. Homma, and T. Masumoto. *Perpendicularly magnetized Fe-Pt (0 0 1) thin films with $(B \cdot H)_{max}$ exceeding 30 MG Oe.* Journal of Magnetism and Magnetic Materials **177**, 1231 - 1232 (1998).

[134] J. M. Shaw, H. T. Nembach, and T. J. Silva. *Measurement of orbital asymmetry and strain in $Co_{90}Fe_{10}$/Ni multilayers and alloys: Origins of perpendicular anisotropy.* Phys. Rev. B **87**, 054416 (2013).

[135] B. Újfalussy, L. Szunyogh, and P. Weinberger. *Magnetic anisotropy in Fe/Cu(001) overlayers and interlayers: The high-moment ferromagnetic phase.* Phys. Rev. B **54**, 9883–9890 (1996).

[136] A. Nilsson, J. Stöhr, T. Wiell, M. Aldén, P. Bennich, N. Wassdahl, M. G. Samant, S. S. P. Parkin, N. Mårtensson, J. Nordgren, B. Johansson, and H. L. Skriver. *Determination of the electronic density of states near buried interfaces: Application to Co/Cu multilayers.* Phys. Rev. B **54**, 2917–2921 (1996).

[137] K. N. Altmann, D. Y. Petrovykh, G. J. Mankey, N. Shannon, N. Gilman, M. Hochstrasser, R. F. Willis, and F. J. Himpsel. *Enhanced spin polarization of conduction electrons in Ni explained by comparison with Cu.* Phys. Rev. B **61**, 15661–15666 (2000).

[138] C. Carbone, M. Veronese, P. Moras, S. Gardonio, C. Grazioli, P. H. Zhou, O. Rader, A. Varykhalov, C. Krull, T. Balashov, A. Mugarza, P. Gambardella, S. Lebègue, O. Eriksson, M. I. Katsnelson, and A. I. Lichtenstein. *Correlated Electrons Step by Step: Itinerant-to-Localized Transition of Fe Impurities in Free-Electron Metal Hosts.* Phys. Rev. Lett. **104**, 117601 (2010).

[139] R. Knut, E. K. Delczeg-Czirjak, J. M. Shaw, H. T. Nembach, P. Grychtol, D. Zusin, C. Gentry, E. Turgut, H. C. Kapteyn, M. M. Murnane, O. Arena, D. A.and Eriksson, O. Karis, and T. J. Silva. *Localization of Fe d-states in Ni-Fe-Cu alloys and implications for ultrafast demagnetization.* arXiv:1508.03015 (2015).

[140] B. N. Engel, C. D. England, R. A. Van Leeuwen, M. H. Wiedmann, and C. M. Falco. *Interface magnetic anisotropy in epitaxial superlattices.* Phys. Rev. Lett. **67**, 1910–1913 (1991).

[141] D. Ceresoli, U. Gerstmann, A. P. Seitsonen, and F. Mauri. *First-principles theory of orbital magnetization.* Phys. Rev. B **81**, 060409 (2010).

[142] P. Söderlind, O. Eriksson, B. Johansson, R. C. Albers, and A. M. Boring. *Spin and orbital magnetism in Fe-Co and Co-Ni alloys.* Phys. Rev. B **45**, 12911–12916 (1992).

[143] Chadov, S., Minár, J., Katsnelson, M. I., Ebert, H., Ködderitzsch, D., and Lichtenstein, A. I. *Orbital magnetism in transition metal systems: The role of local correlation effects.* EPL **82**, 37001 (2008).

[144] C. Kittel. *On the Gyromagnetic Ratio and Spectroscopic Splitting Factor of Ferromagnetic Substances.* Phys. Rev. **76**, 743–748 (1949).

[145] W. Platow, A. N. Anisimov, G. L. Dunifer, M. Farle, and K. Baberschke. *Correlations between ferromagnetic-resonance linewidths and sample quality in the study of metallic ultrathin films.* Phys. Rev. B **58**, 5611–5621 (1998).

[146] O. Hennemann and E. Siegel. *Spin- Wave Measurements of Exchange Constant A in Ni-Fe Alloy Thin Films.* phys. stat. sol. **77**, 229 (1976).

[147] C. Wilts and S. Lai. *Spin wave measurements of exchange constant in Ni-Fe alloy films.* IEEE Transactions on Magnetics **8**, 280-281 (1972).

[148] B. Heinrich, D. J. Meredith, and J. F. Cochran. *Wave number and temperature dependent Landau-Lifshitz damping in nickel.* Journal of Applied Physics **50**, 7726-7728 (1979).

[149] L. Lagae, R. Wirix-Speetjens, W. Eyckmans, S. Borghs, and J. D. Boeck. *Increased Gilbert damping in spin valves and magnetic tunnel junctions.* Journal of Magnetism and Magnetic Materials **286**, 291 - 296 (2005). Proceedings of the 5th International Symposium on Metallic Multilayers.

[150] J. Rantschler, B. Maranville, J. J. Mallett, P. Chen, R. McMichael, and W. Egelhoff. *Damping at normal metal/permalloy interfaces.* Magnetics, IEEE Transactions on **41**, 3523-3525 (2005).

[151] J. M. Shaw, H. T. Nembach, and T. J. Silva. *Determination of spin pumping as a source of linewidth in sputtered $Co_{90}Fe_{10}$/Pd multilayers by use of broadband ferromagnetic resonance spectroscopy.* Phys. Rev. B **85**, 054412 (2012).

[152] M. Oogane, T. Wakitani, S. Yakata, R. Yilgin, Y. Ando, A. Sakuma, and T. Miyazaki. *Magnetic Damping in Ferromagnetic Thin Films.* Japanese Journal of Applied Physics **45**, 3889-3891 (2006).

[153] C. Scheck, L. Cheng, and W. E. Bailey. *Low damping in epitaxial sputtered iron films.* Applied Physics Letters **88**, 252510 (2006).

[154] Y. Yin, F. Pan, M. Ahlberg, M. Ranjbar, P. Dürrenfeld, A. Houshang, M. Haidar, L. Bergqvist, Y. Zhai, R. K. Dumas, A. Delin, and J. Akerman. *Tunable permalloy-based films for magnonic devices.* Phys. Rev. B **92**, 024427 (2015).

[155] J. Walowski, M. D. Kaufmann, B. Lenk, C. Hamann, J. McCord, and M. Münzenberg. *Intrinsic and non-local Gilbert damping in polycrystalline nickel studied by Ti:sapphire laser fs spectroscopy.* Journal of Physics D: Applied Physics **41**, 164016 (2008).

[156] Y. Liu, A. A. Starikov, Z. Yuan, and P. J. Kelly. *First-principles calculations of magnetization relaxation in pure Fe, Co, and Ni with frozen thermal lattice disorder.* Phys. Rev. B **84**, 014412 (2011).

[157] S. Ingvarsson, L. Ritchie, X. Y. Liu, G. Xiao, J. C. Slonczewski, P. L. Trouilloud, and R. H. Koch. *Role of electron scattering in the magnetization relaxation of thin* $Ni_{81}Fe_{19}$ *films.* Phys. Rev. B **66**, 214416 (2002).

[158] C. Luo, Z. Feng, Y. Fu, W. Zhang, P. K. J. Wong, Z. X. Kou, Y. Zhai, H. F. Ding, M. Farle, J. Du, and H. R. Zhai. *Enhancement of magnetization damping coefficient of permalloy thin films with dilute Nd dopants.* Phys. Rev. B **89**, 184412 (2014).

[159] K. Kobayashi, N. Inaba, N. Fujita, Y. Sudo, T. Tanaka, M. Ohtake, M. Futamoto, and F. Kirino. *Damping Constants for Permalloy Single-Crystal Thin Films.* IEEE Transactions on Magnetics **45**, 2541-2544 (2009).

[160] Y. Zhao, Q. Song, S.-H. Yang, T. Su, W. Yuan, S. S. P. Parkin, J. Shi, and W. Han. *Experimental Investigation of Temperature-Dependent Gilbert Damping in Permalloy Thin Films.* Scientific Reports **6**, 22890 (2016).

[161] C. T. Boone, J. M. Shaw, H. T. Nembach, and T. J. Silva. *Spin-scattering rates in metallic thin films measured by ferromagnetic resonance damping enhanced by spin-pumping.* Journal of Applied Physics **117**, 223910 (2015).

[162] F. D. Czeschka, L. Dreher, M. S. Brandt, M. Weiler, M. Althammer, I.-M. Imort, G. Reiss, A. Thomas, W. Schoch, W. Limmer, H. Huebl, R. Gross, and S. T. B. Goennenwein. *Scaling Behavior of the Spin Pumping Effect in Ferromagnet-Platinum Bilayers.* Phys. Rev. Lett. **107**, 046601 (2011).

[163] M. J. Hurben and C. E. Patton. *Theory of two magnon scattering microwave relaxation and ferromagnetic resonance linewidth in magnetic thin films.* Journal of Applied Physics **83**, 4344-4365 (1998).

[164] J. Lindner, K. Lenz, E. Kosubek, K. Baberschke, D. Spoddig, R. Meckenstock, J. Pelzl, Z. Frait, and D. L. Mills. *Non-Gilbert-type damping of the magnetic relaxation in ultrathin ferromagnets: Importance of magnon-magnon scattering.* Phys. Rev. B **68**, 060102 (2003).

[165] M. Sparks, R. Loudon, and C. Kittel. *Ferromagnetic Relaxation. I. Theory of the Relaxation of the Uniform Precession and the Degenerate Spectrum in Insulators at Low Temperatures.* Phys. Rev. **122**, 791–803 (1961).

[166] T. Devolder, P.-H. Ducrot, J. P. Adam, I. Barisic, N. Vernier, J.-V. Kim, B. Ockert, and D. Ravelosona. *Damping of $Co_xFe_{80-x}B_{20}$ ultrathin films with perpendicular magnetic anisotropy.* Applied Physics Letters **102**, 022407 (2013).

[167] R. J. Elliott. *Theory of the Effect of Spin-Orbit Coupling on Magnetic Resonance in Some Semiconductors.* Phys. Rev. **96**, 266–279 (1954).

[168] Y. Sun, H. Chang, M. Kabatek, Y.-Y. Song, Z. Wang, M. Jantz, W. Schneider, M. Wu, E. Montoya, B. Kardasz, B. Heinrich, S. G. E. te Velthuis, H. Schultheiss, and A. Hoffmann. *Damping in Yttrium Iron Garnet Nanoscale Films Capped by Platinum.* Phys. Rev. Lett. **111**, 106601 (2013).

[169] J. Zabloudil, R. Hammerling, L. Szunyogh, and P. Weinberger. *Electron Scattering in Solid Matter.* Springer, Berlin, 2005.

[170] P. J. Durham, B. L. Gyorffy, and A. J. Pindor. *On the fundamental equations of the Korringa-Kohn-Rostoker (KKR) version of the coherent potential approximation (CPA).* J. Phys. F **10**, 661 (1980).

[171] J. S. Faulkner and G. M. Stocks. *Calculating properties with the coherent-potential approximation.* PRB **21**, 3222 (1980).

[172] E. A. Stern. *Rigid-Band Model of Alloys.* Phys. Rev. **157**, 544 (1967).

[173] H. Ebert and M. Battocletti. *Spin and orbital polarized relativistic multiple scattering theory - With applications to Fe, Co, Ni and Fe_xCo_{1-x}.* Solid State Communications **98**, 785 - 789 (1996).

[174] S. Lounis, M. dos Santos Dias, and B. Schweflinghaus. *Transverse dynamical magnetic susceptibilities from regular static density functional theory: Evaluation of damping and g shifts of spin excitations.* Phys. Rev. B **91**, 104420 (2015).

[175] K. Nashimoto, D. K. Fork, and T. H. Geballe. *Epitaxial growth of MgO on GaAs(001) for growing epitaxial $BaTiO_3$ thin films by pulsed laser deposition.* Applied Physics Letters **60**, 1199-1201 (1992).

[176] A. Masuda and K. Nashimoto. *Orientation of MgO Thin Films on Si(100) and GaAs(100) Prepared by Electron-Beam Evaporation.* Japanese Journal of Applied Physics **33**, L793 (1994).

[177] O. Dugerjav, H. Kim, and J. M. Seo. *Growth of a crystalline and ultrathin MgO film on Fe(001).* AIP Advances **1**, 032156 (2011).

[178] W. Y. Hsu and R. Raj. *MgO epitaxial thin films on (100) GaAs as a substrate for the growth of oriented $PbTiO_3$.* Applied Physics Letters **60**, 3105-3107 (1992).

[179] B. Hu, W. He, J. Ye, J. Tang, Y. S. Zhang, S. S. Ahmad, X. Q. Zhang, and Z. H. Cheng. *Determination of magnetic anisotropy constants and domain wall pinning energy of Fe/MgO(001) ultrathin film by anisotropic magnetoresistance.* Scientific Reports **5**, 14114 (2015).

[180] K. Gilmore, M. D. Stiles, J. Seib, D. Steiauf, and M. Fähnle. *Anisotropic damping of the magnetization dynamics in Ni, Co, and Fe.* Phys. Rev. B **81**, 174414 (2010).

[181] T. Qu and R. H. Victora. *Dependence of Kambersky damping on Fermi level and spin orientation.* Journal of Applied Physics **115**, 17C506 (2014).

[182] M. Haertinger, C. H. Back, S.-H. Yang, S. S. P. Parkin, and G. Woltersdorf. *Properties of Ni/Co multilayers as a function of the number of multilayer repetitions.* Journal of Physics D: Applied Physics **46**, 175001 (2013).

[183] G. Fratucello and P. Vavassori. *Magnetic interface anisotropy in Ni/Fe/Ni(1 1 1) trilayers.* Journal of Magnetism and Magnetic Materials **272-276, Supplement**, E927 - E928 (2004). Proceedings of the International Conference on Magnetism (ICM 2003).

[184] I. Barsukov, S. Mankovsky, A. Rubacheva, R. Meckenstock, D. Spoddig, J. Lindner, N. Melnichak, B. Krumme, S. I. Makarov, H. Wende, H. Ebert, and M. Farle. *Magnetocrystalline anisotropy and Gilbert damping in iron-rich $Fe_{1-x}Si_x$ thin films.* Phys. Rev. B **84**, 180405 (2011).

Publication list

2017

Magnetic properties of ultra-thin 3d transition-metal binary alloys I: spin and orbital moments, and anisotropy, and confirmation of Slater-Pauling behavior
Schoen, M. A. W., Lucassen, J., Nembach, H. T., Silva,T. J., Koopmans,B., Back, C. H. and Shaw, J. M.
arXiv:1701.02177
Accepted in Phys. Rev. B

Magnetic properties in ultra-thin 3d transition metal alloys II: experimental verification of quantitative theories of damping and spin-pumping
Schoen, M. A. W., Lucassen, J., Nembach, H. T., Silva,T. J., Koopmans,B., Back, C. H. and Shaw, J. M.
arXiv:1701.02475
Accepted in Phys. Rev. B

The temperature dependence of FeRh's transport properties
Mankovsky, S., Polesya, S., Chadova, K., Ebert, H., Staunton, J. B., Gruenbaum, T., Schoen, M. A. W., Back, C. H., Chen, X. Z., and Song, C.
Submitted to Phys. Rev. B

Terahertz spin currents and inverse spin Hall effect in thin-film stacks containing complex magnetic compounds
Seifert, T., Martens, U., Günther, S., Schoen, M. A. W., Radu, F., Chen, X. Z., Lucas, I., Ramos, R., Aguirre, M. H., Algarabel, P. A., Anadón, A., Körner, H., Walowski, J., Back, C.H., Ibarra, M. R., Morellón, L., Saitoh, E., Wolf, M., Song, C., Uchida, K., Münzenberg, M., Radu, I., and Kampfrath, T.
Submitted to SPIN

2016

Ultra-low magnetic damping of a metallic ferromagnet.
Schoen, M. A.W., Thonig, D., Schneider, M. L., Silva, T. J., Nembach, H. T., Eriksson, E., Karis, O., and Shaw, J. M.
Nat. Phys 12, 839-842 (2016)

Anisotropic Polar Magneto-Optic Kerr Effect of Ultrathin Fe/GaAs(001) Layers due to Interfacial Spin-Orbit Interaction.
Buchner, M., Högl, P., Putz, S., Gmitra, M., Günther, S., Schoen, M. A.W., Kronseder, M., Schuh, D., Bougeard, D., Fabian, J., and Back, C.H.
Phys. Rev. Lett. 117, 157202 (2016).

2015

Perpendicular Magnetic Anisotropy and Easy Cone State in $Ta/Co_{60}Fe_{20}B_{20}/MgO$
Shaw, J. M., Nembach, H. T., Weiler, M., Silva, T. J., Schoen, M., Sun, J. Z., and Worledge, D. C.
IEEE Magnetics Letters 6, 3500404 (2015).

Radiative damping in waveguide-based ferromagnetic resonance measured via analysis of perpendicular standing spin waves in sputtered permalloy films.
Schoen, M. A.W., Shaw, J. M., Nembach, H. T.,Weiler, M., and Silva, T. J.
Phys. Rev. B 92, 184417 (2015).

Aknowledgement

I would like to thank:

Christian H. Back, for his support throughout my work on this dissertation, for giving me the opportunity to continue working on my project at the University of Regensburg, for always having an open ear, and for interesting discussions

Justin Shaw, for his support with sample deposition and SQUID measurements, for the idea to investigate binary alloys, for all his support during the writing process, and for a great time working at NIST.

Stefan Günther for dragging me into this and for helpful suggestions and discussions.

Tom Silva for sharing his expertise of ferromagnetism, development of the radiative damping model, and his continued support.

Matthias Kronseder for growing the $Co_{25}Fe_{75}$ samples in Regensburg, his exceptional motivation, great ideas and discussions, and a fun day mountainbiking.

Mathias Weiler for being a great office mate at NIST and for his help interpreting the radiative damping measurements.

Hans Nembach for his expertise with FMR measurements at NIST and great ski days at Breckenridge.

Ron Goldfarb for giving me the opportunity to work at NIST and for insightful comments on my work.

Danny Thonig and Olle Eriksson for performing the DFT calculations and fruitful discussions about the theoretical description of damping.

Tobias Grünbaum for his great work on FeRh alloys, interesting discussions, and being fun to work with.

Thomas Mayer for his great work with FMR measurements, good discussions, and motivation.

Juriaan Lucassen for all his help growing and measuring the Ni-Fe and Ni-Co sample series.

Markus Haertinger for building a great FMR setup, for always being around to help and for showing me the ropes at BESSY.

Robert Islinger, Martin Buchner, and Johannes Stigloher for being great office mates.

Markus Hollnberger for always understanding my designs for the FMR setup and insightful suggestions.

Chen Luo, Simon Poellath, Florin Radu, and Hanjo Ryll for their help and support a the VEKMAG endstation of the PM2 beamline of BESSY2.

Michael Schneider for performing high field measurements on the $Co_{25}Fe_{75}$ samples.